ESPOO 2006 VTT PUBLICATIONS 616

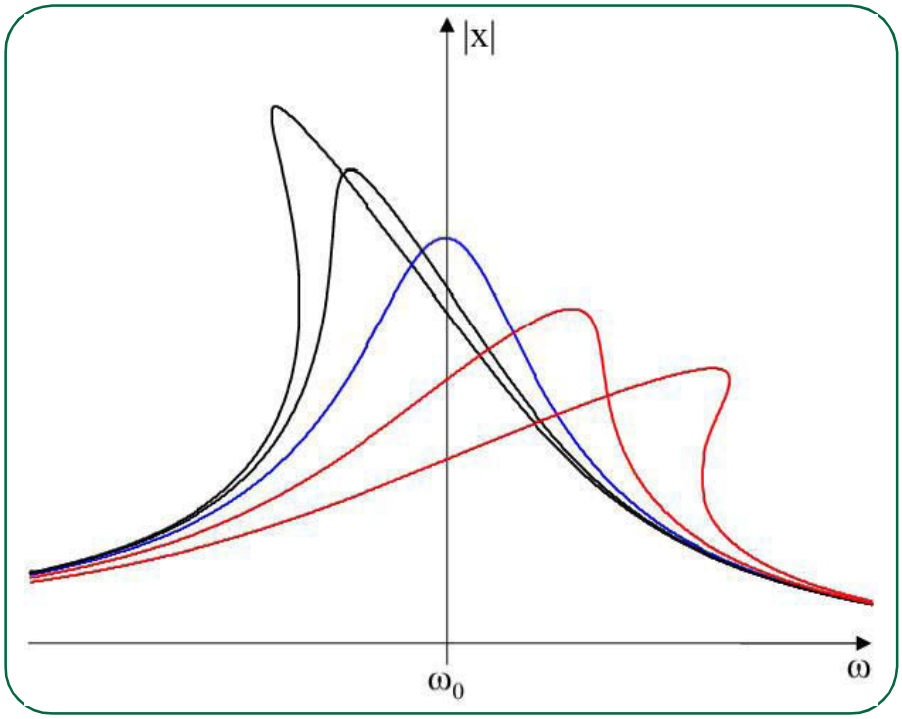

Ari Alastalo

Microelectromechanical Resonator-Based Components for Wireless Communications

Filters and Transmission Lines

VTT PUBLICATIONS 616

Microelectromechanical Resonator-Based Components for Wireless Communications

Filters and Transmission Lines

Ari Alastalo

Dissertation for the degree of Doctor of Science in Technology to be presented with due permission of the Department of Engineering Physics and Mathematics for public examination and debate in Large Seminar Hall of Micronova at Helsinki University of Technology (Espoo, Finland) on the 1st of November, 2006, at 12 o'clock noon.

ISBN 951–38–6865–6 (soft back ed.)
ISSN 1235–0621 (soft back ed.)

ISBN 951–38–6866–4 (URL: http://www.vtt.fi/publications/index.jsp)
ISSN 1455–0849 (URL: http://www.vtt.fi/publications/index.jsp)

Copyright © VTT Technical Research Centre of Finland 2006

JULKAISIJA – UTGIVARE – PUBLISHER

VTT, Vuorimiehentie 3, PL 2000, 02044 VTT
puh. vaihde 020 722 111, faksi 020 722 4374

VTT, Bergsmansvägen 3, PB 2000, 02044 VTT
tel. växel 020 722 111, fax 020 722 4374

VTT Technical Research Centre of Finland, Vuorimiehentie 3, P.O.Box 2000, FI-02044 VTT, Finland
phone internat. +358 20 722 111, fax + 358 20 722 4374

VTT, Tietotie 3, PL 1000, 02044 VTT
puh. vaihde 020 722 111, faksi 020 722 7012

VTT, Datavägen 3, PB 1000, 02044 VTT
tel. växel 020 722 111, fax 020 722 7012

VTT Technical Research Centre of Finland, Tietotie 3, P.O. Box 1000, FI-02044 VTT, Finland
phone internat. +358 20 722 111, fax +358 20 722 7012

Edita Prima Oy, Helsinki 2006

Alastalo, Ari. Microelectromechanical Resonator-Based Components for Wireless Communications. Filters and Transmission Lines [Mikromekaanisiin resonaattoreihin perustuvat komponentit langattoman tiedonsiirron sovelluksissa. Suodattimet ja siirtolinjat]. Espoo 2006. VTT Publications 616. 57 p. + app. 56 p.

Keywords MEMS, radio-frequency MEMS, microelectromechanical filters, micro-electromechanical resonators, components, transducers, wireless communication, transmission lines, acoustic wave propagation, intermodulation

Abstract

Starting in the early 1960's, when the integrated-circuit (IC) technology was developed, micromachining and microelectromechanical systems (MEMS) have grown into a broad research field with several commercial successes. Typical applications of MEMS are in physical, chemical and biochemical sensors, as well as in optical systems such as the digital micromirror device of Texas Instruments. From the 1990's, the advances in the processing technologies and the tremendous growth of the wireless-communication market have drawn much interest into radio-frequency MEMS devices (RF MEMS) such as filters, oscillators, switches and tunable capacitors. These are now beginning to penetrate the market.

This thesis considers electrostatically-actuated RF-MEMS filters and delay lines. For filters, the work concentrates on nonlinear distortion and filter design. The intermodulation properties of capacitively-coupled MEMS filters are analytically solved in closed form and the theory is verified in numerical simulations as well as in measurements with MEMS resonators. The analysis is more generally valid than the previously published results. The theory is utilized to formulate a design procedure for MEMS filters that, for the first time, takes systems speci-fications for tolerable intermodulation distortion and insertion-loss into account. For delay lines, capacitive actuation of bulk-acoustic waves in a solid rod is analyzed. In particular, challenges in impedance matching due to the weakness of the electrostatic coupling are quantified. Finally, a new kind of resonator-chain delay line for high-frequency (HF) signals is introduced. This delay line is characterized by extremely slow signal group velocity (~ 10–100 m/s), narrow-band response, and much lower characteristic impedance than found for the solid-rod waveguide enabling efficient signal coupling. Properties of the resonator-chain waveguide are theoretically analyzed and the results are verified in measurements of fabricated devices.

Alastalo, Ari. Microelectromechanical Resonator-Based Components for Wireless Communications. Filters and Transmission Lines [Mikromekaanisiin resonaattoreihin perustuvat komponentit langattoman tiedonsiirron sovelluksissa. Suodattimet ja siirtolinjat]. Espoo 2006. VTT Publications 616. 57 s. + liitt. 56 s.

Avainsanat MEMS, radio-frequency MEMS, microelectromechanical filters, micro-electromechanical resonators, components, transducers, wireless communication, transmission lines, acoustic wave propagation, intermodulation

Tiivistelmä

Mikroelektromekaanisten järjestelmien (MEMS) kehitys alkoi 1960-luvun alussa yhdessä integroitujen piirien (IC) teknologian kanssa. Tähän päivään mennessä mikromekaniikka on kehittynyt laajaksi tutkimusalaksi ja johtanut useisiin kaupallisiin menestyksiin. MEMS-teknologiaa sovelletaan mm. fysikaalisissa, kemiallisissa ja biokemiallisissa antureissa sekä optisissa järjestelmissä, kuten Texas Instrumentsin mikropeileissä, joita käytetään videoprojektroreissa. Kiinnostus radiotaajuisiin MEMS- komponentteihin (RF MEMS) on lisääntynyt voimakkaasti 1990-luvun alusta alkaen valmistusteknologian ja langattoman tiedonsiirron markkinoiden kehityksen myötä. Radiotekniikassa MEMS-teknologiaa pyritään soveltamaan mm. suodattimissa, oskillaattoreissa, kytkimissä ja säädettävissä kondensaattoreissa. Ensimmäiset tällaiset komponentit ovat jo kaupallistuneet.

Tässä väitöskirjassa käsitellään kapasitiivisesti kytkettyjä RF-MEMS-suodattimia ja viivelinjoja. Suodattimien osalta työ keskittyy epälineaarisuuksien ja häviöiden huomioimiseen suodinsuunnittelussa. MEMS-suodinten intermodulaatio-ominaisuudet ratkaistaan työssä analyyttisesti aikaisempaa yleisemmin ja saadut tulokset varmennetaan tietokonesimulaatioissa ja mittauksissa. Tulosten pohjalta laaditaan MEMS-suodinsuunnittelulle säännöt, joissa otetaan ensimmäistä kertaa huomioon asetetut vaatimukset sekä intermodulaatiolle että häviöille. Viivelinjojen osalta työssä käsitellään mikromekaaniseen tankoon perustuvaa tilavuusaaltoviivelinjaa ja tuodaan esiin vaikeudet, jotka liittyvät riittävän hyvän kytkennän saavuttamiseen tällaisessa rakenteessa. Tehokkaampi kytkentä on HF-taajuuksilla mahdollinen jousimassaketjuun perustuvaan viivelinjaan, jollainen esitellään ja analysoidaan tässä väitöstyössä. Hyvän kytkennän lisäksi tämän viivelinjan ominaisuuksiin kuuluu kapeakaistaisuus ja erittäin hidas signaalin kulkunopeus. Mikromekaanisen jousimassaketjuviivelinjan toiminta varmennetaan mittauksin.

Preface

Research for this dissertation was done at the Microsensing Laboratory of VTT Information Technology during 2002–2005. The work was done in close collaboration with several colleagues at Microsensing, the Microelectronics Centre and the Radiotechnology group of VTT as well as with many co-workers in the Materials Physics Laboratory, SMARAD Radio Laboratory, Metrology Research Institute and Circuit Theory Laboratory of Helsinki University of Technology (TKK).

Funding from VTT in the Future Communication Technologies strategic technology theme for the MEMS radio project and from the Academy of Finland in the Future Electronics Research Programme (TULE) for the MIRA project was indispensable to the research work and is gratefully acknowledged. I am also thankful to the Jenny and Antti Wihuri Foundation, the Academy of Finland and VTT for financial support during 2006 to finalize the thesis.

I am deeply indebted to my instructor Prof. Heikki Seppä and to the manager of Microsensing Dr. Timo Varpula for an opportunity to work in the field of RF MEMS and for guidance in the research work. They have, together with all the personnel, managed to create and maintain excellent working conditions and fruitful and open atmosphere in Microsensing. In particular, the inexhaustible ideas of Prof. Seppä are invaluable in stimulating brainstorming to find directions and to meet challenges of research. I am most thankful to my supervisors Prof. Martti Salomaa, whose dedicated guidance was deprived from his students by his untimely death in 2004, and to Prof. Matti Kaivola, who has greatly facilitated the final stages of the work. Insightful comments of Dr. Tapani Ryhänen and Dr. Remco Wiegerink were also of valuable help in writing the overview. In addition, I have been privileged to collaborate with Professors Antti Räisänen, Ilkka Tittonen, Aarne Oja and Markku Åberg.

I wish to express my gratitude to the many co-workers at VTT and TKK that I have been fortunate to work with during the years. Especially, technical discussions with Doc. Tomi Mattila and Dr. Ville Kaajakari have been most beneficial. Somehow, they have always found time to share their insight. Special thanks go to Dr. James Dekker and Dr. Jyrki Kiihamäki for outstanding work in MEMS fabrication that enabled the experiments of the thesis. Discussions and collaboration with as well as help and support of a large number of people, including Mika Koskenvuori, Jan Holmberg, Hannu Salminen, Markku Jenu, Dr. Tauno Vähä-Heikkilä, Dr. Timo Veijola, Dr. Jouni Knuuttila, Pekka Rantakari, Mikko Kiviranta, Anu Kärkkäinen, Dr. Jukka Kyynäräinen, Paula Holmlund, Jari Penttilä, Anssi Rautiainen, Ari Häärä, Dr. Kari Leppänen, Seija Lepistö, Aija Kaski and Kaisa Falenius, are also thankfully acknowledged.

My warm thanks go to my parents Maire and Reijo and to my brother Petri for support and presence in the many good things of life. Finally, the greatest of my thanks belong to my dear wife Hanna and to my wonderful son Aaro for bringing value and joy to each day.

List of Publications

This thesis is based on the following original publications. Other related publications by the author are cited in the text [1–4].

Intermodulation Distortion in MEMS Filters:

I Ari T. Alastalo and Ville Kaajakari, "Intermodulation in Capacitively Coupled Microelectromechanical Filters," *IEEE Electron Device Letters*, vol. 26, no. 5, pp. 289–291, May 2005.

II Ari T. Alastalo and Ville Kaajakari, "Third-Order Intermodulation in Microelectromechanical Filters Coupled with Capacitive Transducers," *IEEE Journal of Microelectromechanical Systems*, vol. 15, no. 1, pp. 141–148, February 2006.

III Ari T. Alastalo and Ville Kaajakari, "Systematic Design Approach for Capacitively Coupled Microelectromechanical Filters," *IEEE Transactions on Ultrasonics, Ferroelectrics, and Frequency Control*, vol. 53, no. 9, pp. 1662–1670, September 2006.

Acoustic Transmission Lines:

IV Ari T. Alastalo, Tomi Mattila, and Heikki Seppä, "Analysis of a MEMS Transmission Line," *IEEE Transactions on Microwave Theory and Techniques*, vol. 51, no. 8, pp. 1977–1981, August 2003.

V Ari T. Alastalo, Tomi Mattila, Heikki Seppä, and James Dekker, "Micromechanical slow-velocity delay lines," *Proc. 33rd European Microwave Conference*, Münich, Germany, 6–10 October, 2003, pp. 967–970.

VI Ari T. Alastalo, Jyrki Kiihamäki, and Heikki Seppä, "Microelectromechanical delay lines with slow signal propagation," *Journal of Micromechanics and Microengineering*, vol. 16, pp. 1854–1860, August 2006.

In the text, these publications are referred to by their Roman numerals.

Author's Contribution

The author has done all the theoretical analysis, characterization of the MEMS components, numerical simulations and measurements of all the contributed publications I–VI. He has also been responsible of writing of all the papers and has contributed most of the text of I–V and all of VI. The author has designed the MEMS components used in V and VI. In addition, the author has presented the results of the work at international conferences including the European Microwave Conference in Münich (Germany) 2003 and the IEEE International Ultrasonics Symposium in Rotterdam (The Netherlands) 2005.

Contents

Abbreviations

VTT	Technical Research Centre of Finland
TKK	Helsinki University of Technology
ETSI	European Telecommunications Standards Institute
GSM	global system for mobile communications (an ETSI standard)
RFID	radio-frequency identification
RX	radio receiver
TX	radio transmitter
IC	integrated circuit
FET	field-effect transistor
LNA	low-noise amplifier
MEMS	microelectromechanical systems
SOI	silicon on insulator
LTO	low-temperature oxide
CVD	chemical vapor deposition
RIE	reactive-ion etch
DRIE	deep reactive-ion etch (Bosch process)
ICP	inductively-coupled plasma
SAW	surface-acoustic wave
BAW	bulk-acoustic wave
FBAR	film-bulk-acoustic resonator
RF	radio frequency
IF	intermediate frequency of a superheterodyne receiver
HF	high frequency (3–30 MHz) (hydrofluoric acid in fabrication)
VHF	very high frequency (30–300 MHz)
UHF	ultra high frequency (300 MHz–3 GHz)
IM3	third-order intermodulation
IP3	third-order intercept point
IIP3	input-referred third-order intercept point
SIR	signal-to-intermodulation ratio
C/I	carrier-to-interference ratio

Symbols and Notation

ϵ_0	vacuum permittivity	8.85419×10^{-12} F/m
ρ	density	
Y	Young's modulus	
$\dot{y}$	time derivative of variable y	
$\ddot{y}$	second time derivative of variable y	
q	charge	
φ	electrostatic potential	
U	voltage	
V	bias voltage	
V_{pi}	pull-in voltage	
u	AC source voltage	
$\bar{u}$	normalized AC voltage (small)	$= u/V$
C	capacitance	
E	capacitor energy	$= \frac{1}{2}CU^2$
A	area of a capacitive transducer	
x	transducer or resonator displacement	
d	transducer gap with $x = 0$	
ξ	normalized transducer displacement (small)	$= x/d$
C_0	transducer capacitance with $x = 0$	$= \epsilon_0 A/d$
Z_0	transducer impedance with $x = 0$	$= 1/(j\omega C_0)$
η	electromechanical coupling	$= C_0 V/d$
k_e	electromechanical spring constant	$= \eta V/d$
k	spring constant of a harmonic resonator	
m	resonator mass	
γ	resonator damping constant	
Q	resonator quality factor	$= \sqrt{km}/\gamma$
ω_0	resonator eigenfrequency	$= \sqrt{k/m}$
$H(\omega)$	resonator response function	$= H'(\omega) + jH''(\omega)$
ω_e	electromechanical frequency	$= \sqrt{k_e/m}$
$\bar{k}$	spring constant with capacitive coupling	$= k - 2k_e$
$\bar{\omega}_0$	eigenfrequency with capacitive coupling	$= \sqrt{\bar{k}/m}$
$\bar{Q}$	quality factor with capacitive coupling	$= \sqrt{\bar{k}m}/\gamma$
R_m	electrical-equivalent resonator resistance	$= \gamma/\eta^2$

L_m	electrical-equivalent resonator inductance	$= m/\eta^2$
C_m	electrical-equivalent resonator capacitance	$= \eta^2/\bar{k}$
Z_L	load impedance	
R_L	load resistance	
C_L	load capacitance	
R_{ac}	source resistance	
R'_S	series-equivalent source resistance	
C'_S	series-equivalent source capacitance	
R'_L	series-equivalent load resistance	
C'_L	series-equivalent load capacitance	
γ'	loaded resonator dissipation constant	$= \eta^2 \left(R_{\mathrm{m}} + R'_S + R'_L\right)$
k'	loaded resonator spring constant	$= \eta^2 \left(\frac{1}{C_{\mathrm{m}}} + \frac{1}{C'_S} + \frac{1}{C'_L}\right)$
Q'	loaded resonator Q value	$= \sqrt{k'm}/\gamma'$
ω'	loaded resonator eigenfrequency	$= \sqrt{k'/m}$
u'	Thévenin-equivalent-source AC voltage	$= u/(1 + j\omega C_0 R_{\mathrm{ac}})$
P_{IIP3}	input power corresponding to IIP3	
P_{1dB}	input power for to 1-dB compression	
Γ_{III}	ratio of third harmonic to fundamental	
Γ	interference to signal ratio	
Γ_{int}	amplitude ratio of interferers	
G_V	voltage gain	
k_c	coupling spring of a resonator chain	
k_a	anchoring spring of a resonator chain	
m_0	coupling mass of a resonator chain	
a	period of a resonator chain	
ω_s	frequency of a symmetric eigenmode of a two-mode resonator	
ω_a	frequency of an antisymmetric eigenmode of a two-mode resonator	
K	ratio of anchoring spring to coupling spring	$= k_a/k_c$
M	total coupled-resonator mass	$= 2m + m_0$
λ	wavelength	
κ	wavevector	$= 2\pi/\lambda$
v_g	group velocity	
v_{ph}	phase velocity	
Z_c	characteristic impedance of a transmission line	

1 Introduction

Acoustic wave propagation in solids has for a long time been utilized in RF electronics to implement various functionalities in components such as local oscillators, filters, and delay lines. Such devices are based on transduction between electric signals and acoustic waves with part of the signal processing being performed in the mechanical domain. In these applications, one benefits from i) low attenuation of acoustic waves in crystalline materials and ii) low acoustic wave velocity compared to electromagnetic waves. The low attenuation enables high Q values of mechanical resonators in components such as quartz-based oscillators [5] that are widely used as low-phase-noise frequency references in mobile-communication devices. The low-loss propagation is also essential in surface-acoustic-wave (SAW) and bulk-acoustic-wave (BAW or FBAR) filters [6, 7]. The acoustic SAW and BAW velocities are of the order of 5000 m/s that is approximately 10^5 times smaller than the wave velocities for electromagnetic transmission lines. Thus, long signal delays can be produced with small-sized components. This is utilized, for example, in the SAW radio-frequency-identification (RFID) tags.

Recent advances in MEMS technology have opened up the possibility for creating microsized RF devices based on mechanical motion. In MEMS, integrated-circuit (IC) batch-fabrication technologies are utilized to produce miniature mechanical structures usually on a silicon substrate. As an example, a MEMS plate resonator has been demonstrated to be well suited for a high-spectral-purity oscillator in mobile-communication applications with phase-noise properties comparable to its quartz-based counterparts [8]. MEMS variable capacitors and, especially, switches are the most studied RF MEMS components with commercial products now on sale by a few companies [9]. MEMS switches are also utilized, for example, in phase shifters and impedance tuners [10, 11]. Micromechanical filters are at present studied as a potential technology for bandpass filtering in receiver front ends either at RF or IF frequencies [12–16]. Replacement of the conventional SAW and FBAR filters with MEMS that is integrable with CMOS electronics can reduce the cost, power consumption and physical size of the RF circuitry. This becomes more and more important as the number of different radios in a single device is increasing. Sometimes, also stationary components fabricated with MEMS technology, such as inductors and waveguides, are considered as a part of RF MEMS. For recent review articles and books on RF MEMS, see [9, 10, 17–20] and [21, 22], respectively. Besides in RF applications, MEMS technology is utilized, for example, in sensors, such as accelerometers, gyroscopes, magnetometers and pressure sensors, as well as in microfluidic devices and in micromirrors for projection displays (see, for example, [23, 24]).

This thesis considers design and analysis of electrostatically-actuated microacoustic RF filters and delay lines fabricated with MEMS technology for radio-communication devices. After the introduction to microelectromechanical systems in Chapter 1, the thesis focuses on the new scientific results of the work. In

Chapter 2, intermodulation (IM) properties of capacitively-coupled MEMS filters are analytically solved and the theory is verified in numerical simulations as well as in measurements. Although MEMS filters are widely studied in the literature, IM has received less attention. The new theory is utilized to formulate a design procedure for MEMS filters that takes both IM and insertion-loss requirements into account. Usage of the procedure is exemplified and implications of the analysis for different receiver architectures are discussed. MEMS delay lines are considered in Chapter 3. First, capacitive actuation of bulk-acoustic waves in a solid rod is analyzed. In particular, challenges in impedance matching due to the weakness of the electrostatic coupling are quantified. Then, a new kind of resonator-chain delay line for HF-frequency signals is introduced. This delay line is characterized by extremely slow signal group velocity, narrow-band response, and much lower characteristic impedance than found for the solid-rod waveguide enabling efficient signal coupling. Properties of the resonator-chain waveguide are theoretically analyzed and verified in simulations and measurements. Conclusions of the work are presented in Chapter 5.

1.1 MEMS in Radio Architectures

MEMS-based components have been suggested to implement many of the needed functionalities in modern communication devices. To set the context of the thesis more clearly, a typical superheterodyne radio architecture is depicted in Fig. 1 [25]. The blue shading indicates components that can possibly be realized with MEMS technology. In addition to the switches, phase shifters, local oscillators, filters and impedance tuners that are generally recognized as potential applications of MEMS [8–11, 15, 20–22], for the power sensor, used in the radio of Fig. 1 to control the power amplifier (PA), one can consider using MEMS, as first discussed in [26] and developed further, for example, in [2, 27].

Instead of developing MEMS replacements of conventional components, full utilization of the properties of MEMS may well require a redesign of the overall architecture and may prove well suited also for low-power low-performance radios of wireless sensors. Namely, MEMS may allow some of the different operations of Fig. 1 to be performed in a single electromechanical device, such as the RX front-end filtering, mixing and even the low-noise amplification using parametric pumping [1, 28]. In [15, 29], an architecture is considered, where the RX-band-select filter is replaced with a switchable bank of narrow-band filters with different center frequencies to cover the RX band. With such an approach, the linearity requirements of the LNA and the mixer can be relaxed due to the introduced selectivity against in-channel interferences. A multitude of parallel channel-select filters is also considered in [30] with FBAR filters for a radio of wireless sensors. Instead of many parallel filters, one can also consider using a single multimode MEMS resonator, such as the plate resonator of [8] with Lamé and square-extensional modes, if the size of the radio is to be minimized.

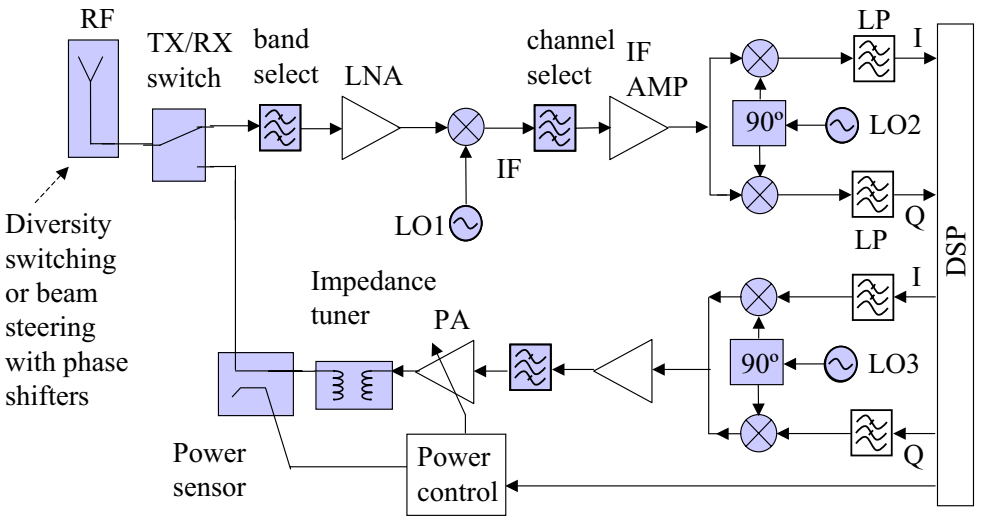

Figure 1: Superheterodyne radio architecture. Components for which MEMS implementation can be considered are indicated in blue.

Figure 2 schematically shows another possible architecture for a low-power radio transponder terminal that communicates with a high-power basestation. Here the TX carrier is generated from the RX signal using a time delay during which the TX/RX switch changes its state. The carrier generation can comprise, for example, a phase-lock loop or, if the basestation is sending an unmodulated carrier for the terminal TX, passband filtering can be enough. With a narrow-band delay line, the filters in Fig. 2 can possibly be omitted. SAW RFID tags are an example of a transponder radio, where the input RX pulse is coupled to a delay line with multiple reflectors that cause many TX pulses, with identifiable inter-pulse delays, to be sent back.

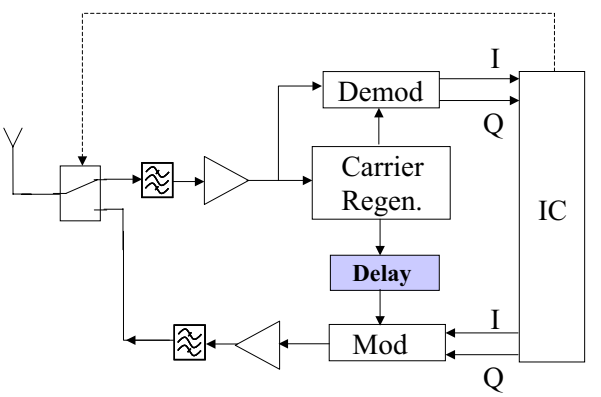

Figure 2: Schematic of a radio-transponder architecture where the delay line is used to separate reception and transmission in time.

1.2 Mechanical Resonators

Typical mechanical resonator geometries are shown in Fig. 3. The applied force, F, either stretches (a) or bends (b) the beam or stretches the plate (c) that is anchored to ideally undeformable supports. For small amplitudes at and close to the resonance frequency, the resonators can be modelled with a linear spring-mass system, as shown in Fig. 3 (d), for which the equation of motion is

$$m\ddot{x} + \gamma\dot{x} + kx = F \Leftrightarrow \ddot{x} + \frac{\omega_0}{Q}\dot{x} + \omega_0^2 x = F/m \equiv \bar{F}. \tag{1}$$

Here $\omega_0 = \sqrt{k/m}$ is the eigenfrequency and $Q = \sqrt{km}/\gamma$ is the quality factor of the resonator with spring constant, k, mass, m, and dissipation, γ. The dots above the variables refer to derivation with respect to time. Solution to (1) can conveniently be written using the complex response function

$$H(\omega) \equiv \left(\omega_0^2 - \omega^2 + j\frac{\omega\omega_0}{Q}\right)^{-1} \tag{2}$$

as

$$x(\omega) = \bar{F}H' + \dot{\bar{F}}H''/\omega, \tag{3}$$

where H' and H'' denote the real and imaginary parts of H, respectively. The second term in (3), which is proportional to the first time derivative of the applied force, describes the power dissipation of the system. The absolute value of the response

$$|H| = \sqrt{H'^2 + H''^2} = \left[\left(\omega_0^2 - \omega^2\right)^2 + \left(\omega\omega_0/Q\right)^2\right]^{-1/2} \tag{4}$$

gives the amplitude, x_0, of the displacement, x, as $x_0 = |H|\bar{F}_0$, where $\bar{F}_0$ is the scaled amplitude of the applied force.

For large amplitudes, nonlinearities of the resonator have to be taken into account. Spring nonlinearities can be included in (1) by replacing the linear spring force with a nonlinear force as

$$kx \rightarrow kx + k_2x^2 + k_3x^3 + \ldots. \tag{5}$$

Taking the nonlinear terms into account only up to the third order, the equation of motion (1) becomes

$$\ddot{x} + \frac{\omega_0}{Q}\dot{x} + \omega_0^2 x + \alpha x^2 + \beta x^3 = \bar{F}, \tag{6}$$

where $\alpha \equiv k_2/m$ and $\beta \equiv k_3/m$. The higher-order terms (αx^2 and βx^3) in (6) introduce a shift to the resonance frequency, $\omega_r \equiv \omega_0 + \omega_\delta$, and tilt the response of the resonator [31, 32] (Duffing effect). The resonance frequency shift, ω_δ, as a function of the resonator amplitude, x_0, is given by

$$\omega_\delta = \delta x_0^2, \tag{7}$$

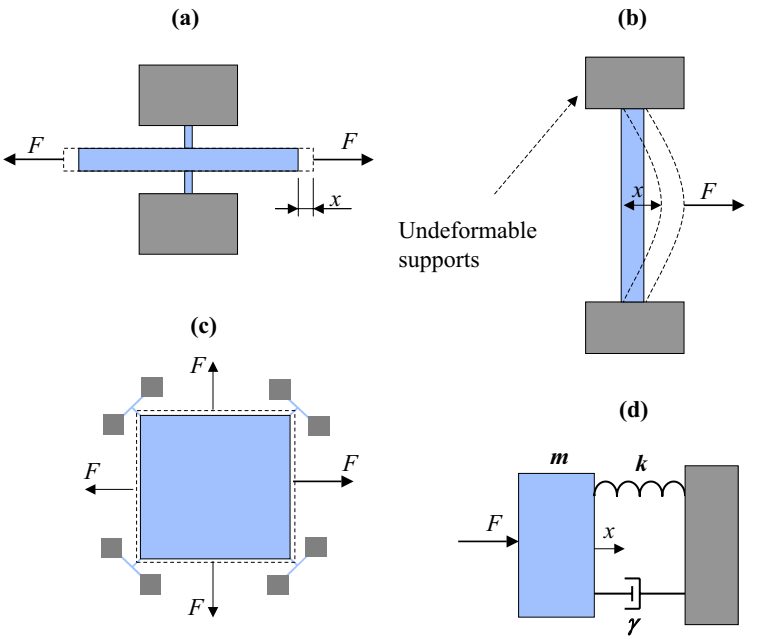

Figure 3: Typical resonator geometries, (a) stretching beam (b) bending beam and (c) extending plate of [8]. The resonators are anchored to stationary supports. (d) For small motion close to the resonance frequency, the resonators can be modelled with a linear spring-mass system (harmonic oscillator).

where [31, 32]

$$\delta = \frac{3\beta}{8\omega_0} - \frac{5\alpha^2}{12\omega_0^3}. \tag{8}$$

At the critical resonance amplitude of

$$x_{0,\,c} = \frac{2\sqrt{\omega_0}}{\sqrt{3Q|\delta|\sqrt{3}}}, \tag{9}$$

the response becomes a multivalued function of frequency with two stable and one unstable solution for each excitation frequency resulting in hysteresis [31,32]. The amplitude responses of the linear ($\delta = 0$) and some nonlinear resonators are schematically shown in Fig. 4. The nonlinear responses have been obtained by considering a unit-amplitude force ($\bar{F}_0 = 1$) and solving for the resonator amplitude, x_0, in (4) after substitutions $|H| = x_0$ and $\omega_0 \rightarrow \omega_r = \omega_0 + \delta x_0^2$. The behaviour of the response in hysteresis is also indicated.

The resonator geometries of Fig. 3 are typical in RF MEMS filters [12,13,15,33] and oscillators [8, 34, 35]. Other state-of-the-art MEMS resonators have been based, for example, on tuning forks, [36], folded-beams [15], ring [37] or circular disk [38, 39] geometry. The highest frequency-Q products of microresonators have been reported for a silicon ring [37] and a diamond disk [40] ($Q > 10\ 000$

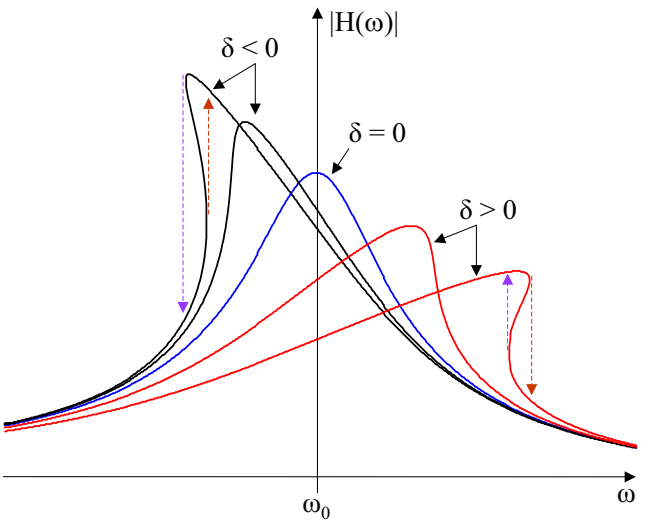

Figure 4: Tilting of the resonator response due to nonlinearity. The dashed arrows show the behaviour of the solution with hysteresis, when the frequency ω of the excitation force is increased (red) or lowered (blue).

at $f \sim 1$ GHz). Research is also in progress towards reducing the size of the resonators below one micrometer [41, 42]. Compared to MEMS, utilization of these submicron nanomechanical (NEMS) devices in RF systems is much more challenging due to their more complicated fabrication and inefficient coupling to electric signals.

1.3 Electrostatic Transduction in MEMS

Several choices exist for coupling electrical signals and mechanical motion [21,43]. In microsystems, most common is the electrostatic actuation due to its low power consumption, fast operation and simplicity of the needed fabrication processes [21, 22]. The most studied RF application of MEMS is an RF switch [22] (for recent references, see also [44–46]) for which capacitive coupling typically suffers from high actuation voltages (high, at least, for battery-powered applications) and inadequate reliability due to dielectric charging [22]. Therefore, for MEMS switches, one has also utilized piezoelectric [47] and magnetic [48] transducers, as well as combinations of magnetic and electrostatic [49] and of thermal and electrostatic transducers [50].

Capacitively actuated MEMS resonators have been demonstrated at up to GHz frequencies [37, 39]. However, achieving good enough signal coupling becomes increasingly challenging as the device size shrinks with increasing resonance frequency. Consequently, higher bias voltages and smaller transducer gaps are needed. Alternatively, piezoelectric coupling has been used also for MEMS resonators [51–54] as well as electromagnetic [55], magnetostrictive [56] and ther-

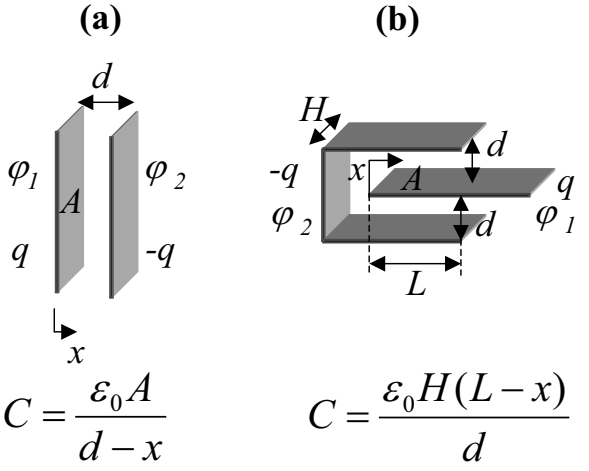

Figure 5: Conductors at potentials φ_1 and φ_2 with charges q and $-q$, respectively, forming the parallel-plate (a) and comb-drive (b) capacitive transducers. The conductor plate with charge q is movable and its displacement with respect to the initial position is denoted with x.

mal [57] transducers. Electrostatic transducers with high-permittivity dielectrics replacing the air gap have also recently been introduced [14, 58, 59] and analyzed in detail in [4]. While offering solutions to the problems of electrostatic actuation, the other approaches have their own challenges [21] such as demanding or expensive fabrication (permanent magnets and current coils or piezoelectric or magnetostrictive thin films), slow operation (thermal transducers) and power consumption (thermal and magnetic transducers). In what follows, this thesis concentrates on capacitive coupling.

Two common electrostatic transducers, parallel plate and comb drive, are shown in Fig. 5. The actual comb drive is composed of several elements of the type in Fig. 5 (b) in parallel [60], but here it suffices to consider only a single element. The transducer capacitors are composed of two conductor plates at potentials φ_1 and φ_2 with charges q and $-q$, respectively. One of the plates is movable and its displacement with respect to the initial position is denoted with x. Energy stored in the transducers is

$$E = \frac{1}{2} C U^2 = \frac{1}{2} \frac{q^2}{C}, \tag{10}$$

where $U \equiv \varphi_2 - \varphi_1$ is the voltage difference between the conductors and C is the transducer capacitance given in Fig. 5. With biasing, either the voltage, U, or the charge, q, is kept constant, resulting in a force between the conductor plates

as [61]

$$F = \left.\frac{\partial E}{\partial x}\right|_U = \frac{1}{2}U^2\frac{\partial C}{\partial x} \qquad \text{(voltage bias)} \tag{11 a}$$

$$F = -\left.\frac{\partial E}{\partial x}\right|_q = -\frac{1}{2}q^2\frac{\partial}{\partial x}\left(\frac{1}{C}\right) \quad \text{(charge bias).} \tag{11 b}$$

Consequently, with voltage biasing, the force (11 a) is a nonlinear function of the displacement, x, for the parallel-plate transducer of Fig. 5 (a) while for the comb drive of Fig. 5 (b), the force does not depend on x. Vice versa, with charge biasing, the force (11 b) is independent of x for the parallel-plate transducer and a nonlinear function of x for the comb-drive.

Due to its simple implementation and applicability also in the presence of significant parasitic capacitances [62], such as pad capacitances, voltage biasing has been the preferred solution in RF MEMS applications. Furthermore, although the comb drive results in better linearity properties, better coupling (stronger force) can be obtained with the parallel-plate transducer by minimizing the electrode gap. Good coupling is critical, for example, in MEMS filters to minimize the insertion loss. In the following, only voltage-biased parallel-plate transducers are considered.

One effect of the nonlinearity of the voltage-biased parallel-plate transducer is that when applied to the mechanical resonators of Fig. 3 at high enough bias voltages, the resonators become unstable and are deflected against the stationary electrodes. This effect, called pull-in, can be utilized, for example, in MEMS switches [21] and sensors [26] but must be avoided in RF filters, thus setting an upper limit for the bias voltage (pull-in voltage). With the transducer forces as indicated in Fig. 3, the pull-in voltage is

$$V_{\mathrm{pi},1} = \sqrt{\frac{8kd^2}{27C_0}}, \tag{12 a}$$

where C_0 is the transducer capacitance with $x = 0$. With two transducers placed on both sides of the resonator of Fig. 3 (b), such that the bias forces act in opposite directions, the pull-in occurs at a higher voltage of

$$V_{\mathrm{pi},2} = \sqrt{\frac{kd^2}{2C_0}}. \tag{12 b}$$

In addition, using the two transducers as a differential drive (voltage $V + u$ on one transducer and $V - u$ on the other, where V is the bias voltage and u a small signal) the second-order signal nonlinearity can be reduced. To the third-order nonlinearities that are in focus in this thesis, the differential drive has no effect. Appendix 5 outlines the derivation of (12 a) and (12 b). Since the rest position of the resonator with symmetric biasing for $V < V_{\mathrm{pi},2}$ is at $x = 0$, the effective spring constant, $\bar{k} = k - 2k_e$, vanishes at the pull-in voltage.

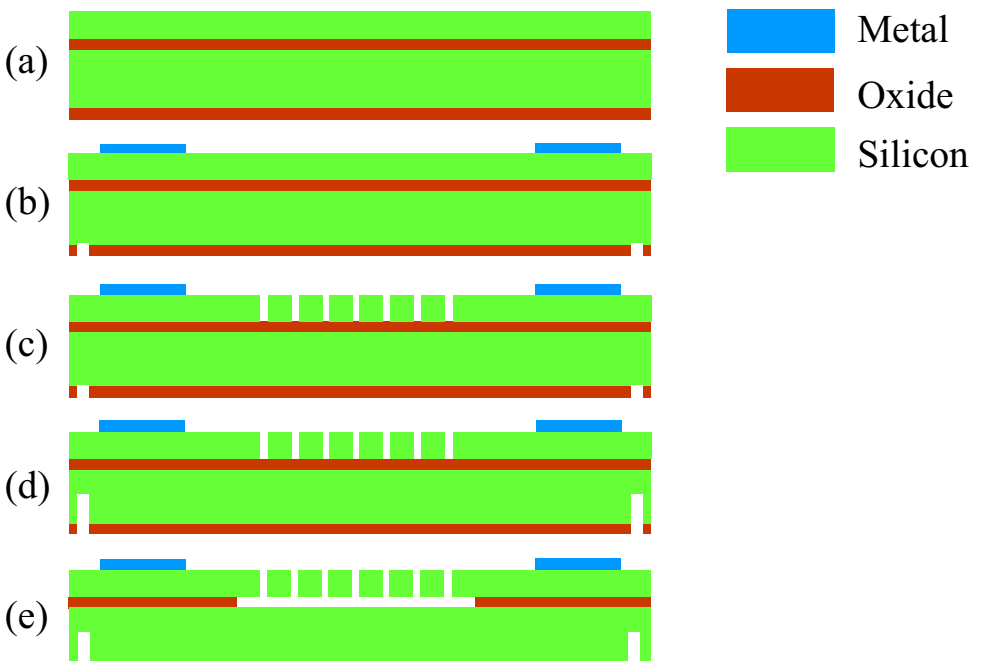

Figure 6: Basic MEMS device fabrication process. (a) Oxide deposition, (b) metallization, (c) device patterning, (d) sawline etching, (e) device releasing.

1.4 SOI MEMS Fabrication at VTT

The silicon-on-insulator (SOI) fabrication processes used at VTT for the components characterized in this thesis are outlined in what follows. More detailed discussions on silicon-based MEMS surface, bulk and SOI micromachining can be found, for example, in [63–65]. Present research also focuses on use of i) diamond for the highest quality factors and two times higher sound velocity than in silicon (higher frequencies with the same resonator dimensions) [40,66], ii) silicon carbide for somewhat higher sound velocity with similar fabrication technologies as for silicon [67,68] and iii) silicon germanium to facilitate post-CMOS integration due to its low thermal budget [38,69]. Diamond and silicon carbide are also considered to be more suitable than silicon for environments with demanding thermal, chemical, radiation or wear conditions [70].

1.4.1 Standard VTT MEMS Process

Fabrication of the devices described in Publication V is illustrated in Fig. 6. The process makes use of a SOI wafer which contains a 1-μm buried oxide layer beneath a 10-μm silicon device layer. After depositing an extra 1-μm-thick low-temperature-oxide (LTO) layer on the wafer backside with chemical vapor deposition (CVD) (a), metal is deposited using Argon (Ar) plasma and patterned on the front side (b). The metallization consists of a titanium-tungsten (TiW) dif-

fusion barrier, a 1-μm-thick aluminum (Al) layer, and a thin molybdenum (Mo) top layer to protect the Al against the hydrofluoric acid (HF) that is later used for release etch. Etching of the metal is carried out using either a chlorine-based ($Cl_2 + BCl_3 + CHCl_3$) reactive-ion-etch (RIE) RF plasma or by wet etching. A short dip in Freckle etchant is used to remove the residual etch debris. Sawing lines are then patterned on the backside oxide layer and etched a few microns deep with $CF_4 + CHF_3$-based RIE plasma. The next step (c) is the patterning of the resonator structures, with nominal gaps of 0.5 μm, and release holes of 1.5 μm diameter. Inductively-coupled plasma (ICP) is used in the Bosch process [64, 71] with $SF_6 + C_4F_8$-etch and C_4F_8 + Ar-passivation steps to form the gaps and release holes using a resist mask, which is then stripped in oxygen plasma before the backside sawlines are etched to a greater depth (d), again using ICP etching but with the previously patterned oxide as a mask. The Bosch process is also called deep reactive-ion etch (DRIE). The buried oxide (and the backside LTO) is then etched for several minutes in 49% HF and then dried in supercritical CO_2 (e). The devices may be separated by cleaving along the sawlines or by sawing.

1.4.2 Fabrication Process for Narrow Gaps

Table 1: Clamped-clamped (CC) beam, free-free (FF) beam and square-plate resonators with narrow transducer gaps.

gap / [nm]	type	dimensions	f / [MHz]	Q	Ref.
200	CC beam	3.7 μm×54μm	8	5400	[72]
100	FF beam	2 μm×40μm	10	10000	[73]
80	CC beam	3 μm×200μm	0.6	4800	[74]
60	CC beam	3 μm×30μm	30	2500	[75]
50	square plate	320 μm×320μm	13	4000	[76]

In order to obtain good-enough coupling with low-enough bias voltages for capacitively-coupled RF MEMS resonators, several processes have been developed to minimize the transducer gap. Resonators with vertical gaps of $d \approx 200$ nm [72], $d \approx 100$ nm [73], $d \approx 80$ nm [74], $d \approx 60$ nm [75] and $d \approx 50$ nm [76] have been fabricated. Relevant properties of these resonators are summarized in Table 1. In [76], a much higher quality factor of $Q > 10^5$ is found for a resonator with otherwise the same parameter values but with the transducer gap increased to $d \approx 180$ nm. For [75], the effective gap, given by the bias-voltage dependence of the resonance frequency, is found to be $d \approx 400$ nm, which is suggested to be caused by carrier depletion. In [72, 73, 75], the reported quality factors for the beam resonators are in good agreement with the support-loss estimate of $Q < 2(L/w)^2$ [77]. For [74, 76], on the other hand, the low quality factors of

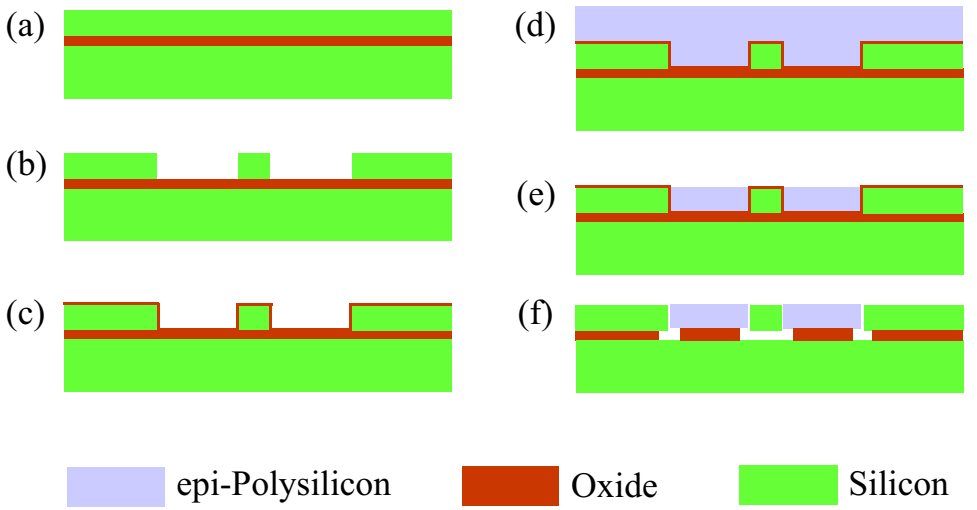

Figure 7: VTT MEMS process for narrow-gap devices. (a) SOI starting wafer, (b) etching of electrode areas with DRIE (Bosch process), (c) deposition of sacrificial oxide, (d) epitaxial polycrystalline-silicon deposition, (e) grinding and polishing, (f) device releasing.

the sub-100-nm-gap resonators can be explained neither by anchoring loss [77] nor by thermoelastic damping [78] but are possibly due to surface effects [77] or contamination [76] in the narrow gaps.

The narrow-gap processes [72–76] are based on a deposition of a thin sacrificial layer of oxide or polysilicon to define the gaps. Figure 7 illustrates the process developed at VTT [76] that is used for the devices characterized in Publications I, II and VI. The electrode areas are first etched in the Bosch process (b) after which a thin sacrificial layer of thermal oxide (c), and a layer of epitaxial polycrystalline silicon (d) are deposited on the wafer. Next, grinding and silicon-selective chemical-mechanical polishing (CMP) are used to bring the structural layer back to its original thickness (e). Finally, HF etch (f) is used to release the vibrating structures. The process can be finalized with a wafer-level vacuum sealing step as discussed in [76].

1.5 Nonlinearities in Signal-Processing Applications

After the above introduction of capacitively-coupled MEMS resonators as well as their mechanical (5) and electrical (11 a) sources of nonlinearity, typical figures of merit of linearity, used in signal-processing applications, are discussed in what follows for future reference. Noise properties of MEMS resonators [79–81] that also are of central importance in signal processing are left outside the scope of this work.

Typically, for a narrow transducer gap, the capacitive nonlinearity is the dom-

inant source of distortion. Odd-order nonlinearities are especially detrimental as they can lead to unwanted frequency components at a desired-signal frequency, ω_0. For example, cubic mixing of two fundamental signals, having frequencies ω_1 and ω_2, results in third-order intermodulation (IM3) products at frequencies $2\omega_1 - \omega_2$ and $2\omega_2 - \omega_1$. This is easily seen [82] with a signal

$$x_{\text{in}} = A_1 \cos \omega_1 t + A_2 \cos \omega_2 t \tag{13}$$

at the input of a nonlinear system for which the response can be modelled as a third-order polynomial

$$x_{\text{out}} = \alpha_0 + \alpha_1 x_{\text{in}} + \alpha_2 x_{\text{in}}^2 + \alpha_3 x_{\text{in}}^3. \tag{14}$$

Here we ignore any nonlinearities of higher than third order, although, in practise, they can also be important. Inserting (13) to (14), one obtains

$$\begin{aligned} x_{\text{out}} = \frac{1}{4} \big[& \alpha_0 + 2\alpha_2 A_1^2 + 2\alpha_2 A_2^2 + \\ & + \Big(\overline{\boxed{4\alpha_1 A_1}} + 3\alpha_3 A_1^3 + \overline{6\alpha_3 A_1 A_2^2} \Big) \cos(\omega_1 t) + \\ & + \big(4\alpha_1 A_2 + 3\alpha_3 A_2^3 + 6\alpha_3 A_1^2 A_2 \big) \cos(\omega_2 t) + \\ & + 2\alpha_2 A_1^2 \cos(2\omega_1 t) + \alpha_3 A_1^3 \cos(3\omega_1 t) + \\ & + 2\alpha_2 A_2^2 \cos(2\omega_2 t) + \alpha_3 A_2^3 \cos(3\omega_2 t) + \\ & + 4\alpha_2 A_1 A_2 \cos(\omega_1 t - \omega_2 t) + 4\alpha_2 A_1 A_2 \cos(\omega_1 t + \omega_2 t) + \\ & + \boxed{3\alpha_3 A_1^2 A_2} \cos(2\omega_1 t - \omega_2 t) + 3\alpha_3 A_1 A_2^2 \cos(2\omega_2 t - \omega_1 t) + \\ & + 3\alpha_3 A_1^2 A_2 \cos(2\omega_1 t + \omega_2 t) + 3\alpha_3 A_1 A_2^2 \cos(\omega_1 t + 2\omega_2 t) \big] . \end{aligned} \tag{15}$$

The boxed, underlined and overlined terms of (15) are referred to in what follows. If $\omega_1 = \omega_0 + \Delta\omega$ and $\omega_2 = \omega_0 + 2\Delta\omega$, the IM3 product at $2\omega_1 - \omega_2$ is at ω_0 corrupting the desired signal at that frequency. In the following, we introduce the commonly used measures of nonlinearity: third-order intercept point, 1-dB compression and harmonics.

Third-Order Intercept Point: The third-order intercept point (IP3) is typically defined as the crossing point of the linear extrapolations of the small-amplitude IM3 signal at $2\omega_1 - \omega_2$ and a fundamental two-tone test signal at ω_1 or ω_2 (with $A_1 = A_2$) in the device output. The signal level at the input, corresponding to IP3, is termed IIP3. Setting the boxed amplitudes in (15) equal, one obtains for the IIP3 amplitude $A_{\text{IIP3}}^2 = 4|\alpha_1|/(3|\alpha_3|)$ [82]. Using the same boxed terms of (15) but the first one for a desired signal, $x_{\text{sig}} = A_{\text{sig}} \cos(\omega_0 t)$, and the second one for interference (13) with $A_1 = A_2 = A_{\text{int}}$, one finds for the signal-to-intermodulation ratio (SIR) at the output of the system

$$\text{SIR} = A_{\text{IIP3}}^2 \frac{A_{\text{sig}}}{A_{\text{int}}^3} = P_{\text{IIP3}} \sqrt{\frac{P_{\text{sig}}}{P_{\text{int}}^3}}, \tag{16}$$

where the last result is expressed in terms of the signal and interference powers at the input. The result (16) is valid also for frequency selective components, such as filters, provided that the IP3 definition is modified as being the crossing point of the linear extrapolations of the IM3 output signal and a wanted output signal when the wanted signal has the same input magnitude as the interferers and is located at the passband center.

1-dB Compression: Typically, the coefficient α_3 for the third-order term in (14) is negative and thus the gain of the system decreases for increasing signal amplitudes as seen in the amplitude of the $\cos(\omega_1 t)$ term in (15). The 1-dB compression point is defined as the input signal level for which the gain has decreased by 1 dB. The corresponding amplitude, $A_{1\text{dB}}$, can be solved using the underlined terms in (15) ($A_2 = 0$). The linear gain for the signal with amplitude A_1 is α_1 while the compressed gain is $\alpha_1 + \frac{3}{4}\alpha_3 A_1^2$. Thus $A_{1\text{dB}}$ is found by solving [82]

$$20\log\left|\alpha_1 + \frac{3}{4}\alpha_3 A_{1\text{dB}}^2\right| = 20\log|\alpha_1| - 1 \text{ dB}. \tag{17}$$

Consequently, in terms of powers, one finds a useful relation between the intercept point and compression

$$P_{1\text{dB}} \approx P_{\text{IIP3}} - 10 \text{ dB}. \tag{18}$$

If $A_2 \gg A_1$, gain for the weaker signal follows from the overlined terms in (15) and the compression point is found as in (17) but with the $\frac{3}{4}$ replaced with $\frac{3}{2}$. One finds

$$\hat{P}_{1\text{dB}} \approx P_{\text{IIP3}} - 13 \text{ dB}, \tag{19}$$

where $\hat{P}_{1\text{dB}}$ denotes the power level at which gain for a much weaker signals is reduced by 1 dB.

Harmonics: The amplitudes of the second and third harmonics ($x_{\text{out}}^{\text{II}}$ and $x_{\text{out}}^{\text{III}}$) with respect to the fundamental term ($x_{\text{out}}^{\text{I}}$) are also easily obtained from (15). In particular, one finds that the third harmonic can be related to P_{IIP3} as

$$\Gamma_{\text{III}} \equiv 20\log_{10}\left(\frac{x_{\text{out}}^{\text{III}}}{x_{\text{out}}^{\text{I}}}\right) = 2\left(P_1 - P_{\text{IIP3}}\right) - 10 \text{ dB}, \tag{20}$$

where P_1 is the power corresponding to the signal amplitude A_1. For example, for the GSM mobile terminal with maximum transmit power of 33 dBm, it is required that the third harmonics in TX remain below -30 dBm [83]. Consequently, ignoring antenna and switch losses, one needs for the power P_{IIP3}, according to (20), $P_{\text{IIP3}} > 60$ dBm. With the switch losses and the antenna efficiency taken into account, the minimum acceptable P_{IIP3} is accordingly raised.

1.6 Objectives of the Work

The objective of the work is to contribute to the progress of reducing the size, price and power consumption (increased operation time of battery-powered devices) of communication systems by wider utilization of MEMS components. Both replacement of components, such as filters, in conventional radios and devices enabling novel radio architectures are to be considered. The research questions of the work are:

1) In order to use capacitive MEMS resonators for front-end filters in wireless radio receivers as suggested, for example, in [15], what are the requirements for the central parameter values such as supply voltage, transducer gap and resonator quality factor?

2) What are the possible obstacles of commercially using MEMS resonators for filtering at UHF frequencies?

3) How to systematically design MEMS filters to meet filter specifications of a communication system such as GSM [83], concentrating, in particular, on intermodulation distortion [84] and on insertion loss?

4) What are the central tradeoffs in filter properties that affect the design?

5) Instead of replacing conventional RF components with MEMS devices, can more be gained through a redesign of the radio architecture? What special requirements do MEMS filters set for the overall system?

6) How can low-loss acoustic propagation in single-crystal silicon be used for novel time-delay components and delay-line radio architectures?

2 Designing MEMS Filters for RF Applications

In radio systems, micromechanical filters have been suggested for bandpass filtering in the receiver front ends either at RF or IF frequencies. In contrast to conventional acoustic SAW and FBAR filters that pass the entire RX band, their MEMS replacements are often thought to have a narrower passband. This is enabled by the high quality factors of MEMS resonators that are achievable by utilizing low-loss single-crystal materials and vacuum packaging. For example, capacitively-actuated MEMS resonators with quality factors of $Q > 100\,000$ at 10 MHz [8] and $Q > 10\,000$ at 1 GHz [37] have been reported. Consequently, one needs tuning of the filter passband or a bank of switchable filters with different center frequencies to cover all the RX channels of the communication system as discussed in [15] and in Sec. 1.1. A central challenge of MEMS filters is to obtain a low-enough mechanical impedance for acceptable insertion loss. Consequently, for bias voltages that are practical for mobile devices, maximizing the resonator quality factor and minimizing the transducer gap become of primary interest although they increase the nonlinear distortion of the device. In this thesis, a filter design approach that takes both insertion-loss and intermodulation-distortion requirements into account is developed.

2.1 Filtering with a Single Resonator

Usage of a mechanical resonator, with mass, m, spring constant, k, and dissipation constant, γ, as a bandpass filter for capacitively-coupled electrical signals with voltage bias is schematically shown in Fig. 8. The load impedance is denoted by Z_L, the source impedance by R_{ac} and $Z = u/i_1$ is the small-signal impedance seen when looking into the input transducer. The resonator mass is grounded and the bias voltage, V, is connected to the mechanically stationary electrodes of the parallel-plate transducers. The transducer area is A and d is the width of the gap with the resonator at its rest position. As the resonator mass is displaced by x, the transducer capacitances become

$$C_1 = \frac{C_0}{1 + x/d} = C_0 \left[1 - \xi + \xi^2 - \xi^3 + \ldots\right] \tag{21 a}$$

$$C_2 = \frac{C_0}{1 - x/d} = C_0 \left[1 + \xi + \xi^2 + \xi^3 + \ldots\right], \tag{21 b}$$

where $C_0 = \epsilon_0 A/d$ is the rest capacitance ($x = 0$) and $\xi \equiv x/d$ is the normalized displacement. With the electromechanical coupling coefficient defined as $\eta \equiv C_0 V/d$ and the spring constant as $k_e \equiv \eta V/d$, the small-signal electrical-equivalent

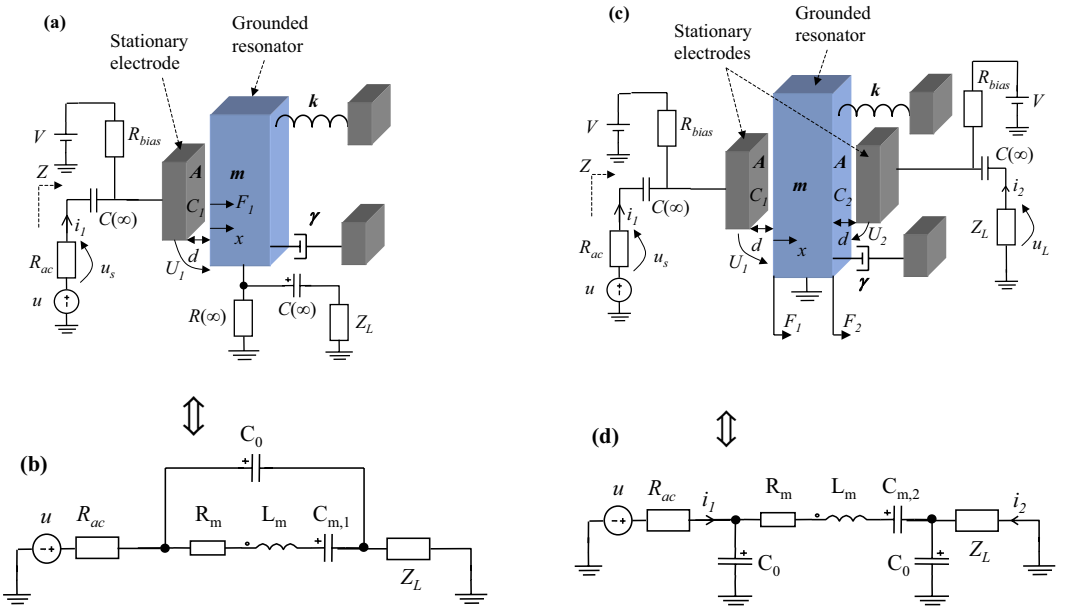

Figure 8: Micromechanical resonator operating as a single-stage band-pass filter for capacitively-coupled signals with unsymmetric (a) and symmetric (c) bias. In (b) and (d), the corresponding electrical-equivalent small-signal models are shown.

parameters in Fig. 8 (b) and (d) are found as [16, 43]

$$R_m = \frac{\gamma}{\eta^2} \tag{22 a}$$

$$L_m = \frac{m}{\eta^2} \tag{22 b}$$

$$C_{m,N} = \frac{\eta^2}{k - Nk_e}, \tag{22 c}$$

where N is the number of transducers ($N = 1$ in Fig. 8 (a,b) and $N = 2$ in Fig. 8 (c,d)). With these definitions, the coupling coefficient, η, is included in the values of the equivalent resistance, inductance and capacitance. Alternatively, the coupling can be modelled with a transformer [43]. In App. 5, details of the derivation of the equivalent circuits are explained. With only one transducer ($N = 1$), the transducer area can be larger than for $N = 2$ resulting in a better electromechanical coupling and lower R_m. For example, for the plate resonator of Fig. 3 (c), all the four faces can be used for actuation. However, as in filtering and delay-line applications it is important to eliminate the direct electrical signal propagation through C_0 between the input and output ports, it is better to use two capacitive transducers ($N = 2$), one for input and one for output, and connect the resonator to AC ground potential as shown in Fig. 8 (c, d). Consequently, in what follows, we mainly concentrate on the two-transducer approach of Fig. 8 (c, d).

Forces F_1 and F_2 in Fig. 8, exerted on the moving mass, are found with (11 a) as

$$F_1 = -\frac{1}{2}\,U_1^2\,\frac{C_0/d}{(1+\xi)^2} = -\frac{1}{2}\,(V+u-u_s)^2\,\frac{C_0}{d}\left[1-2\xi+3\xi^2-4\xi^3+\ldots\right] \quad (23\,\text{a})$$

$$F_2 = \quad \frac{1}{2}\,U_2^2\,\frac{C_0/d}{(1-\xi)^2} = \frac{1}{2}\,(V-u_L)^2\,\frac{C_0}{d}\left[1+2\xi+3\xi^2+4\xi^3+\ldots\right]. \quad (23\,\text{b})$$

Here U_i are the voltages across the transducers ($U_1 = V+u-u_s$ and $U_2 = V-u_L$), $u_s = i_1 R_{\text{ac}}$ is the voltage drop in the source resistance and $u_L = i_2 Z_L$ is the load voltage as indicated in Fig. 8. The currents i_1 and i_2 in Fig. 8 (c,d) are

$$i_1 = \frac{dQ_1}{dt} = \frac{d(C_1U_1)}{dt} = C_1(\dot{u}-\dot{u}_s) + (V+u-u_s)\frac{\partial C_1}{\partial x}\dot{x} \quad (24\,\text{a})$$

$$i_2 = \frac{dQ_2}{dt} = \frac{d(C_2U_2)}{dt} = -C_2\dot{u}_L + (V-u_L)\frac{\partial C_2}{\partial x}\dot{x}, \quad (24\,\text{b})$$

where the derivatives of the capacitances are the same as for the forces in (23 a) and (23 b). Equations (23 a)–(24 b) and the equation of motion of the resonator form the basis of the calculations in this thesis.

2.2 Multi-Stage Filters

Multistage MEMS filters can be composed, for example, by coupling resonators in series with mechanical springs [15, 16], by using shunt capacitors or active buffers [12] or by using direct capacitive coupling between the resonators [13]. The spring coupling [15, 16] has the same electrical-equivalent representation as the shunt-capacitance-coupled filter [12] which is shown in Fig. 9 for two stages. Here C_{gnd} is the inter-stage coupling capacitor.

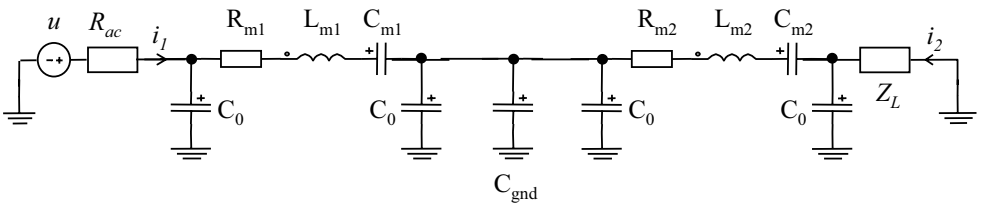

Figure 9: A two-stage MEMS filter where the inter-stage coupling is done with the shunt capacitance C_{gnd}.

2.3 IM3 for MEMS Filters

The intermodulation properties of capacitively-coupled single-resonator MEMS filters are solved in closed form in Publications I–II and the theory is generalized

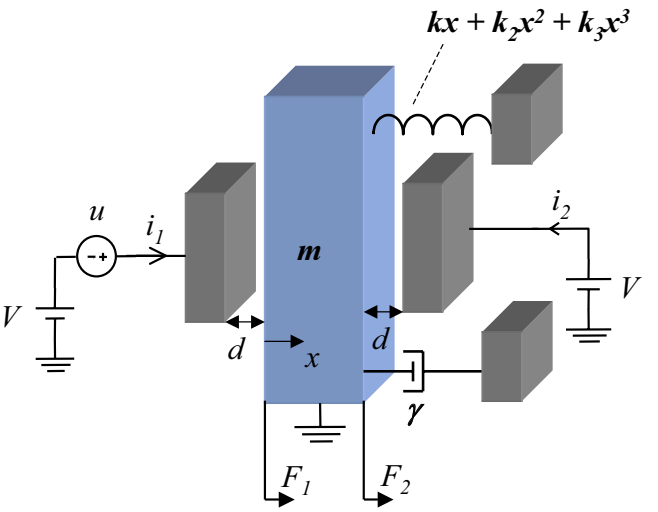

Figure 10: Filter circuit of Fig. 8 (c) simplified for intermodulation analysis.

for higher-order filters in Publication III and [3]. We consider the circuit of Fig. 8 (c) with $R_{\mathrm{ac}} = Z_L = 0$ as shown in Fig. 10. Nonzero source and load impedances will be included afterwards as done in Publication III. Furthermore, for generality we include mechanical spring nonlinearities up to third order with (5). The equation of motion of the resonator in Fig. 10 up to third order in the small parameters, $\bar{u} \equiv u/V$ and $\xi \equiv x/d$, is found with the forces of (23 a) and (23 b) as

$$\ddot{\xi} + \frac{\bar{\omega}_0}{\bar{Q}}\dot{\xi} + \bar{\omega}_0^2 \xi = -\omega_e^2 \left[\bar{u} + \bar{k}_2 \xi^2 - 2\bar{u}\xi + \frac{\bar{u}^2}{2} - \left(4 - \bar{k}_3\right) \xi^3 + 3\bar{u}\xi^2 - \bar{u}^2 \xi \right] = \bar{F}. \quad (25)$$

Here, the following definitions are used: $\bar{\omega}_0 \equiv \sqrt{\bar{k}/m}$, $\bar{Q} \equiv \sqrt{\bar{k}m}/\gamma$, $\omega_e \equiv \sqrt{k_e/m}$, $\bar{k}_2 \equiv dk_2/k_e$ and $\bar{k}_3 \equiv d^2 k_3/k_e$ with $\bar{k} \equiv k - 2k_e$, $k_e \equiv \eta V/d$ and $\eta \equiv C_0 V/d$. The output current is found from (24 b) as

$$\bar{i} \equiv \frac{i_2}{d} = \eta \underbrace{\left(1}_{\bar{i}_{\mathrm{sig}},\, \bar{i}^{(1)}_{\mathrm{IM3}}} + 2\xi + \underbrace{3\xi^2}_{\bar{i}^{(2)}_{\mathrm{IM3}}} + 4\xi^3 + \ldots \right) \dot{\xi}. \quad (26)$$

In (26), we have indicated the terms that contribute to the signal and the intermodulation currents at the fundamental frequency, $\bar{\omega}_0$.

The desired signal, $\bar{u}_{\mathrm{sig}}$, at the resonance frequency, $\bar{\omega}_0$, and an interfering signal, $\bar{u}_{\mathrm{int}}$, at the filter input are now taken as

$$\bar{u}_{\mathrm{sig}} = \bar{u}_{\mathrm{sig},0} \cos \bar{\omega}_0 t, \quad (27a)$$

$$\bar{u}_{\mathrm{int}} = \bar{u}_{\mathrm{int},0} \left(\cos \omega_1 t + \Gamma_{\mathrm{int}} \cos \omega_2 t \right), \quad (27b)$$

where $\omega_1 \equiv \bar{\omega}_0 + \Delta\omega$ and $\omega_2 \equiv \bar{\omega}_0 + 2\Delta\omega$ such that a third-order intermodulation product of (27b) is at the desired-signal frequency, $\bar{\omega}_0$. The frequency separation of the interferers is denoted by $\Delta\omega$. A possible difference in the interferer amplitudes is taken into account with Γ_{int}.

The output signal current, $\bar{i}_{\text{sig}}$, in (26) is found by first obtaining the linear signal motion, ξ_{sig}, from (3) with a force, $\bar{F}_{\text{sig}}$, given by the excitation (27a) in (25) as $\bar{F}_{\text{sig}} = -\omega_e^2 \bar{u}_{\text{sig}}$. Similarly, linear resonator motion, ξ_{int}, at the interferer frequencies, ω_1 and ω_2, is found from (3) with a force, $\bar{F}_{\text{int}}$, given by (27b) in (25) as $\bar{F}_{\text{int}} = -\omega_e^2 \bar{u}_{\text{int}}$. The intermodulation currents, $\bar{i}_{\text{IM3}}^{(1)}$ and $\bar{i}_{\text{IM3}}^{(2)}$, in (26) at $\bar{\omega}_0$ due to the interference (27b) are obtained in Publication II by approximately solving the nonlinear equation of motion (25).

The signal-to-intermodulation ratio (SIR), defined as the ratio of the signal current, $\bar{i}_{\text{sig}}$, to the total intermodulation current, $\bar{i}_{\text{IM3}} = \bar{i}_{\text{IM3}}^{(1)} + \bar{i}_{\text{IM3}}^{(2)}$, is given in Publication II for a general case. For practical usage in filter design, it is more convenient to consider SIR in the limit of $\bar{Q} \to \infty$ that becomes valid as soon as the interferers are well outside the passband of the filter. We find

$$\text{SIR}_{\bar{Q}\to\infty} = \frac{16|\Delta\omega|^3(\bar{\omega}_0 + \Delta\omega)(2\bar{\omega}_0 + \Delta\omega)^2}{\Big[9\Delta\omega^4 + 28\Delta\omega^3\,\bar{\omega}_0 + 2\Delta\omega^2(10\,\bar{\omega}_0^2 - 9\,\omega_e^2) + \\ - 24\Delta\omega\,\omega_e^2\,\bar{\omega}_0 + 3(4 - \bar{k}_3)\omega_e^4\Big]\Gamma_{\text{int}}\Gamma^3\,\bar{u}_{\text{sig},0}^2\,\omega_e^2}, \tag{28}$$

where $\Gamma \equiv \bar{u}_{\text{int},0}/\bar{u}_{\text{sig},0}$ is the interference-to-signal ratio at the filter input. As (28) contains odd powers of $\Delta\omega$, it is asymmetric around the resonance predicting different SIR values for interferers below the resonance and interferers above the resonance.

Another important limit is when the interferers are inside the filter passband ($\Delta\omega \to 0$). This is relevant, for example, when signal self distortion is considered. In terms of the IIP3 voltage, we have with $\Gamma_{\text{int}} = 1$ (Publication I)

$$\bar{u}_{0,\text{IIP3,IB}}^2 = 1\Big/\sqrt{\big[3(1-\bar{k}_3/4)\,p^3 + p/4\big]^2 + 9p^4/4}, \tag{29}$$

where $p \equiv \bar{Q}\omega_e^2/\bar{\omega}_0^2 = k_e\bar{Q}/\bar{k}$. The corresponding SIR is found from (16).

The theoretical results are compared to measurements and numerical simulations in Publication II. A good accuracy of the theory is found as shown, for example, in figure 11 for the square-extensional-mode plate resonator of Fig. 3 (c). The resonator is fabricated on a silicon-on-insulator (SOI) wafer with the narrow-gap process of [76] (see Sec. 1.4.2) and it has a size of 320 μm $\times$ 320 μm $\times$ 10 μm (thickness of the SOI device layer is 10 μm). For other details, see Publication II. For signal input and output, two parallel capacitive transducers on opposite sides of the plate are used. Each transducer corresponds to one of the four forces shown in Fig. 3 (c). For example, for input, the transducers are on the left- and on the right-hand side of the plate while the output transducers are

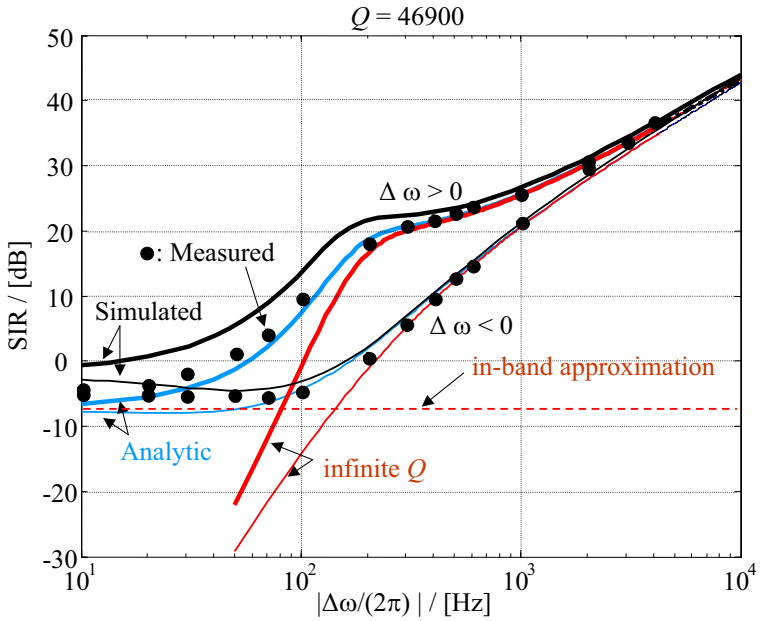

Figure 11: Signal-to-intermodulation ratio as a function of interferer frequency separation for the square-plate resonator of Publication II that is schematically illustrated in Fig. 3 (c). Simulated behaviour (black curves), general analytic result of Publication II (blue curves), analytic result in the limit $\bar{Q} \to \infty$ (28) (red curves), in-band limit (29) (dashed line), and measured results (large dots) are shown. The thin curves are for $\Delta\omega < 0$ while the thick curves are for $\Delta\omega > 0$.

located below and above the plate. A bias voltage is brought to the stationary transducer electrodes while the resonator is grounded. The electrical-equivalent model for the resonator is as shown in Fig. 8 (d) but with a 180° phase change in the output current due to the in-phase motion of all the faces of the plate resonator.

The measurements are done with the MEMS resonator and a JFET (junction field-effect transistor) preamplifier in vacuum using a −50-dBm desired signal (corresponding to a 50 Ω source impedance) at the resonator input at the resonance frequency of $\bar{\omega}_0$ and considering two 0-dBm interferers at $\omega_1 = \bar{\omega}_0 + \Delta\omega$ and $\omega_2 = \bar{\omega}_0 + 2\Delta\omega$. The simulations are done in Aplac® circuit simulator using harmonic balance [85]. As seen in Fig. 11, the infinite-Q limit of (28) becomes valid as soon as the interferers are outside the resonator passband. Also, as predicted by the theory, at the intermediate frequencies of 50 Hz $< |\Delta f| <$ 1 kHz we observe that the SIR is much lower for interferers below the resonance ($\Delta\omega < 0$) than for interferers above the resonance ($\Delta\omega > 0$). This difference is at greatest when the interferer frequencies are close to the 3-dB-passband edge of the resonator. Within the passband, the in-band approximation (29) becomes valid. The excellent agreement between the analytical, simulated and measured results

verifies the theory for weakly coupled ($R_m \gg \{R_{\mathrm{ac}}, Z_L\}$) single-stage capacitive MEMS filters.

The previously reported experimental IM3 results [84] for $\Delta\omega \ll -\omega_0/Q$ are in good agreement with (28). For example, assuming that the spring constant of the clamped-clamped-beam resonator of [84] can be approximated by a point-force result [86], (28) and (16) give the same IIP3 voltage as reported in [84]. On the other hand, for $\Delta\omega > 0$ as well as for the interferers close to the passband edge, results of Publication II and (28) differ from the analytical result of [84].

2.4 Generalization of the IM3 Theory

With source and load impedances that are large enough to not be ignorable, a parellel-to-series impedance transformation is utilized as shown in Fig. 12 for a single-resonator MEMS filter. Here the load impedance is represented by a resistance R_L and capacitance C_L in parallel. Loading of the resonator due to the source and load impedances can now be taken into account by using a loaded dissipation and spring constant

$$\gamma' = \eta^2 \left(R_{\mathrm{m}} + R'_S + R'_L\right) \tag{30 a}$$

$$k' = \eta^2 \left(1/C_{\mathrm{m}} + 1/C'_S + 1/C'_L\right), \tag{30 b}$$

to find a loaded quality factor, $Q' \equiv \sqrt{k'm}/\gamma'$, and resonance frequency, $\omega' \equiv \sqrt{k'/m}$. The series-equivalent resistances and capacitances of Fig. 12 in (30 a) and (30 b) are (see, for example, [87])

$$R'_S = \frac{R_{\mathrm{ac}}}{(R_{\mathrm{ac}}\omega' C_0)^2 + 1} \tag{31 a}$$

$$C'_S = \frac{C_0\left[(R_{\mathrm{ac}}\omega' C_0)^2 + 1\right]}{(R_{\mathrm{ac}}\omega' C_0)^2} \tag{31 b}$$

$$R'_L = \frac{R_L}{\left[R_L\omega'(C_0 + C_L)\right]^2 + 1} \tag{31 c}$$

$$C'_L = \frac{(C_0 + C_L)\left\{\left[R_L\omega'(C_0 + C_L)\right]^2 + 1\right\}}{\left[R_L\omega'(C_0 + C_L)\right]^2}. \tag{31 d}$$

In addition to using the loaded quality factor, Q', the Thévenin-equivalent input voltage

$$u' = u \times \frac{1}{1 + j\omega' C_0 R_{\mathrm{ac}}} \tag{32}$$

must be used in order to be able to utilize the unloaded SIR and IIP3 results (28) and (29) for tightly-coupled filters.

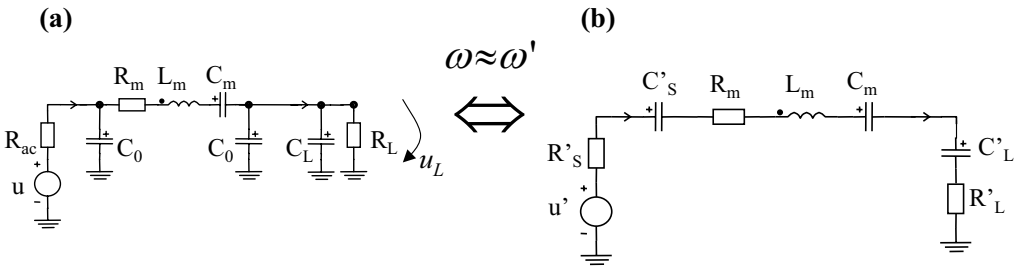

Figure 12: Parallel-to-series impedance transformation for a single-stage MEMS filter. For example, u and $R_{\rm ac}$ can model an antenna while C_L and R_L represent an LNA input.

For filter design, (28) and (29) can be further simplified by assuming that: i) the pass-band desired-signal frequency is much higher than the frequency separation to the interferers present in the filter input, ii) the bias voltage is much lower than the electromechanical pull-in voltage, and iii) mechanical spring nonlinearities can be ignored as much weaker than the capacitive transducer nonlinearities. With these assumptions we find from (28)

$$\mathrm{SIR} = \frac{8\,|\Delta\omega|\,\omega'}{5\,\omega_e^2} \times \frac{V^2}{R'_S\,\Gamma_{\rm int}} \sqrt{\frac{P_{\rm sig}}{P_{\rm int}^3}}. \tag{33}$$

The AC-source powers for the signal and interference are $P_{\rm sig} = u_{\rm sig}^2/(2R_{\rm ac})$ and $P_{\rm int} = u_{\rm int}^2/(2R_{\rm ac})$, respectively. When the interferers are inside the passband, we have from (29) and (16) generalizing to $\Gamma_{\rm int} \neq 0$

$$\mathrm{SIR}_{\rm IB} = \frac{1}{\sqrt{(6p^3 + p/2)^2 + 9p^4}} \times \frac{V^2}{R'_S\,\Gamma_{\rm int}} \sqrt{\frac{P_{\rm sig}}{P_{\rm int}^3}}\ , \tag{34}$$

where $p \equiv Q'\omega_e^2/\omega'^2 = Q'\,k_e/k'$.

In Publication III, it is shown that as $\mathrm{SIR}(\Delta\omega) \to \mathrm{SIR}(-\Delta\omega)$ for out-of-band interferers with $|\Delta\omega| \to \infty$, (33) becomes valid. Furthermore, outside the passband the single-resonator result (28) is also valid for higher-order filters as well as for the tightly-coupled filters provided that the loaded quality factor and the Thévenin-equivalent input voltage of (32) are used as discussed above. Intuitively, this is to be expected as for the out-of-band interferer frequencies, the resonator impedances are high and the resonators are therefore only weakly coupled. Furthermore, as typically the capacitive nonlinearity is much stronger than the mechanical spring nonlinearities, the transducers effectively set the IIP3. Moreover, except close to the passband edge, the force nonlinearity of the first transducer is the dominant source of intermodulation (Publication II).

For in-band frequencies, the IIP3 for higher-order filters depends on the chosen desired-user frequency within the passband. However, the single-stage approximation is still a good order-of-magnitude estimation (Publication III).

2.5 Design Principles of MEMS Filters

In what follows, we derive design criteria for the resonator dimensions, transducer gap, Q value and bias voltage from specified in-band and out-of-band filter attenuation and maximum distortion. The criteria yield a systematic procedure to design MEMS filters for communication systems. We focus on receiver (RX) applications.

Out-of-band attenuation: For minimum performance, the filter should suppress the interferers situated outside the systems RX band to the same level as the strongest interferers within the RX band. If this is achieved, the linearity requirement for the LNA and mixer are set by the in-band interferers that normally are not affected by band-select filtering. Denoting the minimum attenuation at frequency ω with respect to the desired-signal frequency, ω', as $A_{\min}$, the minimum required loaded in-circuit quality factor can be found. For the single-stage MEMS filter, this leads to

$$Q' \geq \frac{\sqrt{A_{\min}^2 - (\omega/\omega')^2}}{\left|1 - (\omega/\omega')^2\right|} \equiv Q'_{\min}. \tag{35}$$

Increasing the filter order makes the stop-band response a steeper function of frequency and thus a lower quality factor for the resonators is sufficient at the cost of higher insertion loss.

Out-of-Band Intermodulation: The weakest signal, with power P_{sig}, to be detected in the presence of interferers, having powers P_{int} at $\omega'+\Delta\omega$ and $\omega'+2\Delta\omega$, leads to requirements for intermodulation performance. Typically, this is specified with the minimum SIR ($\text{SIR}_{\min}$) that the filter needs to satisfy in its output in order to meet the target for the overall systems carrier-to-interference (C/I) ratio. Requiring the SIR to be greater than or equal to the minimum $\text{SIR}_{\min}$ gives from (33)

$$d^3 + (\epsilon_0 A \omega' R_{\text{ac}})^2 d \geq \frac{5}{8} R_{\text{ac}} \Gamma_{\text{int}} \text{SIR}_{\min} \frac{\epsilon_0 A}{m \left|\Delta\omega\right| \omega'} \sqrt{\frac{P_{\text{int}}^3}{P_{\text{sig}}}}, \tag{36}$$

which can also be used for higher-order filters as discussed above. Thus in order to meet the performance requirements given as $\text{SIR}_{\min}$, there is a minimum value for the gap.

In-Band Loss: The passband voltage gain, $G_V \equiv 2u_L/u$, is easily found using the circuits of Fig. 12 and assuming n identical filter stages. Requiring that the passband voltage gain is larger than a specified minimum acceptable value, $G_{\min}$,

a lower limit for QV^2 is found as

$$QV^2 \geq \frac{nd^4\sqrt{km}}{(\epsilon_0 A)^2 \left\{ \frac{2}{\omega' C_L' G_{\min}} \frac{|1+j\omega' C_L' R_L'|}{|1+j\omega' C_0 R_{\mathrm{ac}}|} - R_S' - R_L' \right\}}. \tag{37}$$

Thus, after choosing the gap, d, the unloaded quality factor, Q, and the bias voltage, V, need to be chosen to meet the insertion loss specifications. As the unloaded quality factor is usually determined by material properties, effectively this gives a requirement for the bias voltage. It is to be noted that with a dominantly capacitive termination ($|1/\omega' C_L'| \gg R_L'$) it is possible to obtain voltage gain as the filter acts as an RLC impedance transformer.

In-Band Intermodulation: The in-band intermodulation is estimated from (34) by considering the i) signal self distortion and ii) in-band interferers. However, typically the out-of-band interferers give more stringent linearity requirements. Therefore, after choosing the filter parameters, it is usually sufficient to check that the filter meets the in-band specifications. If these are not met, then the filter gap should be increased and the design adjusted accordingly.

2.6 Design Example

In the following, the usage of the above results is illustrated by a single-stage MEMS front-end filter design for $f_0 = 1$ GHz with requirements of GSM 900 mobile device. The simplified specifications are shown in Table 2. These should be considered as exemplary performance requirements and a realistic system design may set a more or less stringent goals.

Table 2: Simplified RX front-end filter requirements for GSM 900 [83].

Specification		Comment
$\mathrm{SIR}_{\min}$	12 dB	$\rightarrow$ (36)
$G_{\min}$	-3 dB	$\rightarrow$ (37)
$A_{\min}(f - f_0 = 10$ MHz)	23 dB	$\rightarrow$ (35)
to be met with:		
P_{sig}	-99 dBm	Signal
$P_{\mathrm{int}}(\Delta f = 0$ Hz)	-49 dBm	In-band interferer
$P_{\mathrm{int}}(\Delta f = 600$ kHz)	-43 dBm	In-band blocker
$P_{\mathrm{int}}(\Delta f = 10$ MHz)	0 dBm	Out-of-band blocker

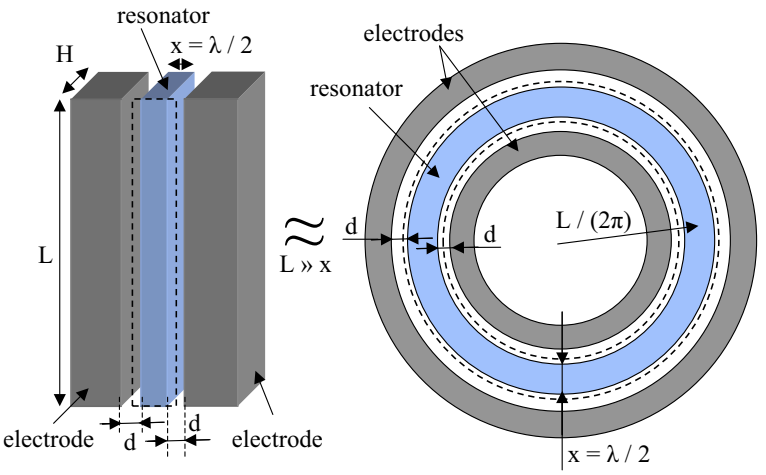

Figure 13: Test geometry for resonator design showing the resonator surrounded by the electrodes. The dotted line indicates the vibration mode shape in extended state.

Resonator geometry: Several structures have been utilized in MEMS microresonators such as bending and stretching beams (see Fig. 3) as well as bulk-acoustic circular [39] or square [8] plates or ring resonators [37]. In order to reach UHF frequencies, micromechanical bending-mode resonators are unpractical since the fundamental frequencies are at HF range (< 30 MHz) and coupling to harmonics of high order is difficult. Bulk-acoustic circular or square plate resonators can have the first vibration mode at VHF range and the second or third harmonic already at ~ 1 GHz [39]. Alternatively, one can utilize the fundamental bulk-acoustic mode of a thin bar or ring for which a very high quality factor is reported in [37]. Above 1 GHz, however, the thickness of the bar becomes only few microns and can easily be limited by fabrication accuracy. As in Publication III, we consider here the bar and ring geometries, shown in Fig. 13, to illustrate the usage of the design equations developed in Sec. 2.5. Other resonator structures can be treated in a similar fashion.

The resonating dimension of the bar in Fig. 13 is $x = \lambda/2 = v/(2f_0) \approx 4\mu$m for $f_0 = 1$ GHz. Here $v = \sqrt{Y/\rho}$ is the bulk-acoustic wave velocity with $\rho = 2330$ kg/m^3 the density and $Y = 168$ GPa the Young's modulus of silicon. The bar can also approximate the ring geometry of [37], shown on the right-hand side of Fig. 13, when the ring radius $L/(2\pi)$ is much larger than the ring width x. The capacitive transducers at both sides of the resonator have an area of $A = HL$ and a rest capacitance of $C_0 = \epsilon_0 HL/d$. The mass and spring coefficient are now [34]

$$m = \rho LxH/2 \tag{38 a}$$

$$k = \pi^2 YLH/(2x). \tag{38 b}$$

We consider a typical thickness of the SOI device layer of $H = 10$ μm after which the resonator length L is varied to find a good geometry. For square plate, instead

of (38 a) and (38 b), one would use $m_{\rm sp} = \rho H L^2$ and $k_{\rm sp} = \pi^2 Y_{\rm 2D} H$, where $Y_{\rm 2D}$ is the effective elastic modulus for the extending plate [8].

Minimum quality factor: From the minimum requirements for the interference attenuation in Table 2, one obtains with (35) a value of $Q'_{\rm min} = 700$ for the minimum loaded quality factor. For channel-select filtering in GSM 900, the passband is 200 kHz corresponding to a much higher in-circuit quality factor of $Q' = 5000$, which would also be enough for $A_{\rm min} = 40$ dB at 10 MHz off the passband in (35) as is typically satisfied by commercial FBAR filters. As higher Q values enable lower bias voltages for the same insertion loss (37), we set the unloaded quality factor to $Q = 2000$, which could be feasible [37], resulting in an unloaded 3-dB bandwidth of 500 kHz.

Minimum gap: The intermodulation requirements set the minimum value for the gap. In Publication III, the filter design is considered with two 0-dBm out-of-band blockers of Table 2 at 10 MHz and 20 MHz off the passband edge. Consequently, the gap minimum is found to be in between 10 nm and 100 nm depending on parameter values. Here we consider only one 0-dBm blocker of Table 2 together with an in-band interferer at $f_0 + 5$ MHz with a power of -49 dBm. In this case (36) yields the lower limit for the gap to be as low as ~ 1 nm. As the gap width is more likely to be limited by the fabrication technology, we consider $d \in \{10, 30, 90\}$ nm in what follows.

Load impedance: In Publication III both resistive and capacitive filter terminations are analyzed. It is shown, in particular, that the requirements of low-enough bias voltage, good linearity and low insertion loss are difficult to be met for battery-powered devices if the conventional resistive 50-Ω source and load termination is to be used. As a capacitive termination enables voltage gain in the filter and thus a lower insertion loss than for a resistive load with the same bias voltage, we consider here only a capacitive termination with $R_L = 1$ MΩ and $C_L = 0.1$ pF. Such an environment for the filter could be realized in an integrated RX architecture where the filter output is directly connected to a capacitive FET LNA (low-noise amplifier) load (C_L and R_L in Fig. 12) while the filter input is fed from a resistive source such as an antenna (u and $R_{\rm ac}$ in Fig. 12).

Bias Voltage: After setting values for the gap, d, resonator length, L, and the AC source impedance, $R_{\rm ac}$, the minimum bias voltage can be solved from (37) as shown in Fig. 14, where the voltage is drawn as a function of the resonator length for different values of the transducer gap and the source resistance. For low-voltage operation, the gap has to be well below 100 nm. For example, the design marked with the circle in Fig. 14, for which $d = 30$ nm, $R_{\rm ac} = 50\ \Omega$ and $L = 200\ \mu$m, needs a bias of 12 V. Other parameters for this filter solution are given in Table 3.

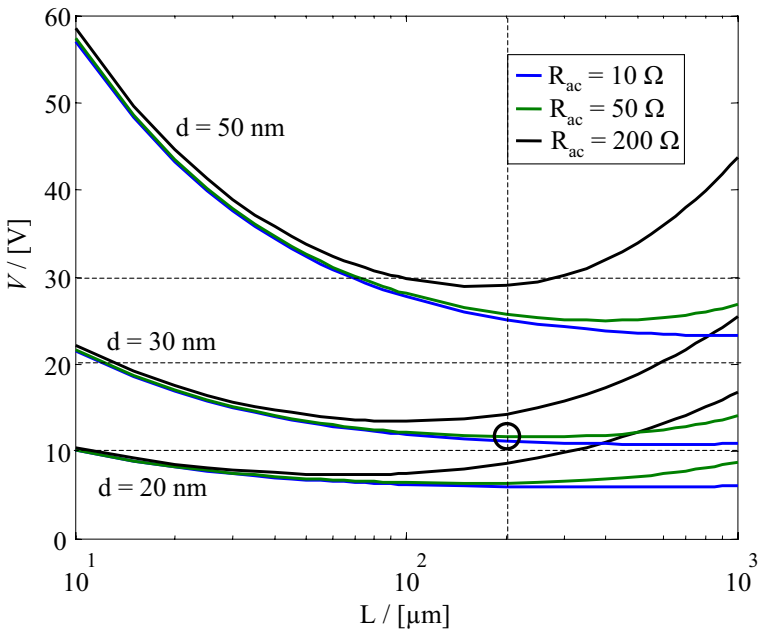

Figure 14: Minimum bias voltage meeting the insertion-loss specification (37).

Table 3: Exemplary filter design that is marked with a circle in Fig. 14.

f_0	[GHz]	1	R_m	[Ω]	560	Q		2000
H	[μm]	10	R_L	[$M\Omega$]	1	Q'		1840
L	[μm]	200	C_L	[pF]	0.1	V_{pi} (12 a)	[V]	420
k	[MN/m]	390	R_{ac}	[Ω]	50	G_V	[dB]	-2.5
m	[fg]	9.9	V	[V]	12	SIR (33)	[dB]	99
d	[nm]	30	C_0	[fF]	590	$\mathrm{SIR}_{\mathrm{IB}}$ (34)	[dB]	110

3 Acoustic Transmission Lines

Acoustic transmission lines have been utilized in several applications. For example, in wireless passive SAW RFID tags and sensors, the transmitted data is coded into a multitude of reflections of a SAW pulse that is generated (in response to a received radio pulse) and detected by an antenna connected to a SAW chip [88]. In these applications, long acoustic delays and short transmission distances guard against interference from multipath radio propagation. In radar systems, delay lines are used, for example, to create a delayed replica of the transmit signal to correlate it with the received signal reflected from the target [89], to compensate for phase errors in FMCW radars [90], or to simulate a target. In delay-line oscillators, long delay stabilizes the frequency and suppresses off-carrier phase noise [91–93]. Delay-line based information processing has been applied, for example, to implement convolution [94]. Analog delays are also proposed for novel ultra-wideband receivers [95]. In video systems, delay lines are used, for example, in event recorders and action replay. In this work a capacitively-coupled bulk-acoustic microsized transmission line is analyzed and a new MEMS delay-line structure for long time delays, consisting of a chain of coupled resonators, is introduced.

3.1 Bulk-Wave Wavequides

An acoustic transmission line for high frequencies is obtained when the mechanical resonator of Fig. 8 (c) is replaced with an elastic continuous medium obeying the wave equation as shown in Fig. 15. Here longitudinal bulk-wave propagation is utilized for signal transmission in an electrostatically-coupled microsized silicon rod of the kind analyzed in detail in Publication IV. In Fig. 15, the wave equation for the mechanical displacement y along the rod is

$$\frac{\partial^2 y(x,t)}{\partial t^2} = c^2 \frac{\partial^2 y(x,t)}{\partial x^2} \ , \ t \geq 0 \ , \ x \in [0, \Delta x], \tag{39}$$

where $c^2 = Y/\rho$ with Y being the Young's modulus and ρ the density of the rod material. The boundary conditions are

$$\left.\frac{\partial y(x,t)}{\partial x}\right|_{x=0} = \frac{F_1}{AY} \quad , \quad \left.\frac{\partial y(x,t)}{\partial x}\right|_{x=\Delta x} = \frac{F_2}{AY} \ , \tag{40}$$

where F_1 and F_2 are the electrostatic forces of (23 a) and (23 b) of the input and output transducers, respectively.

Solving the wave equation as is done in Publication IV, allows one to identify the input impedance in Fig. 15 as $Z = Z_0 || Z_{\rm em}$, where $Z_{\rm em}$ for small k_e obeys the standard transmission-line equation [96]

$$Z_{\rm em} = Z_c \frac{Z_T + Z_c \tanh(j\beta\Delta x)}{Z_c + Z_T \tanh(j\beta\Delta x)} \ , \tag{41}$$

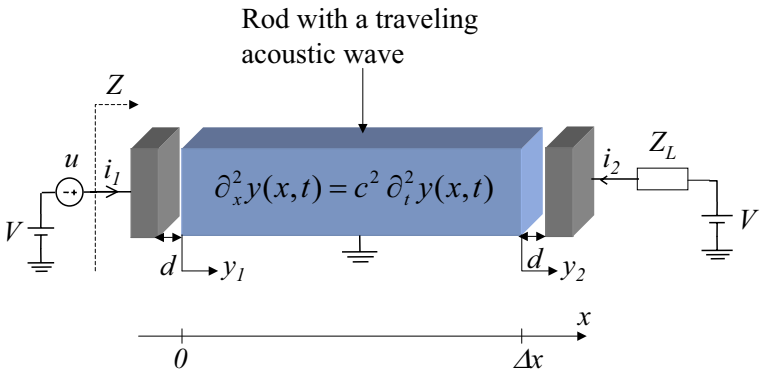

Figure 15: Schematic representation of a setup where an electric signal is transmitted through a micromechanical rod as an acoustic plane longitudinal wave.

where $\beta \equiv \omega/c$, $Z_c \equiv AY/\left(c\eta^2\right)$ and $Z_T \equiv Z_0||Z_L$. The mechanical losses can be included in (41) by substituting $j\beta$ with $j\beta + \alpha$ where α is the attenuation coefficient [96, 97]. For zero reflection at the output, one needs $Z_T = Z_c$, which gives with (41)

$$Z_{\text{em}} = Z_c = \frac{AY}{c\eta^2} = \frac{A\sqrt{\rho Y}}{\eta^2} = \frac{d^4\sqrt{\rho Y}}{A\left(\epsilon_0 V\right)^2}\ . \tag{42}$$

Here $A\sqrt{\rho Y}$ is the mechanical characteristic impedance of the rod [98]. The corresponding matched load impedance is $Z_L = (Z_c||Z_0^*)$. Thus Z_c can be seen as an electrical characteristic impedance of the acoustic waveguide.

For practical realisation of the MEMS waveguide, impedance matching is a challenge. This is because the weakness of the capacitive coupling makes the characteristic electrical impedance, Z_c, in (42) extremely high. As (42) shows, Z_c can be made smaller by having a smaller gap, d, softer or sparser rod material (smaller Y or ρ), a larger area, A, higher-permittivity material in the gap or a higher bias voltage, V. On the other hand, the maximum displacement of the end of the rod is limited by pull-in. For example, for a silicon rod with $Y = 168$ GPa, $\rho = 2330$ kg/m^3, $A = 10 \times 100$ $(\mu\text{m})^2$, $d = 100$ nm and $V = 100$ V, one finds $Z_c = 2.5$ MΩ while the lower limit for Z_c, given by pull-in, is 2.1 MΩ (see Publication IV) for a 1 mm long rod.

3.2 Resonator Chains

A capacitively-coupled spring-mass-chain waveguide of Publications V and VI, shown in Fig. 16 without dissipation, is composed of elementary resonators that can be modelled with two identical moving masses, m, that are coupled with a spring of strength k_c and anchored to a stationary support with springs of strength k_a. Except for the ends, the chain is periodic with period a. The waveguide can be seen as a high-order bandpass filter [15, 16] with identical stages. Using a

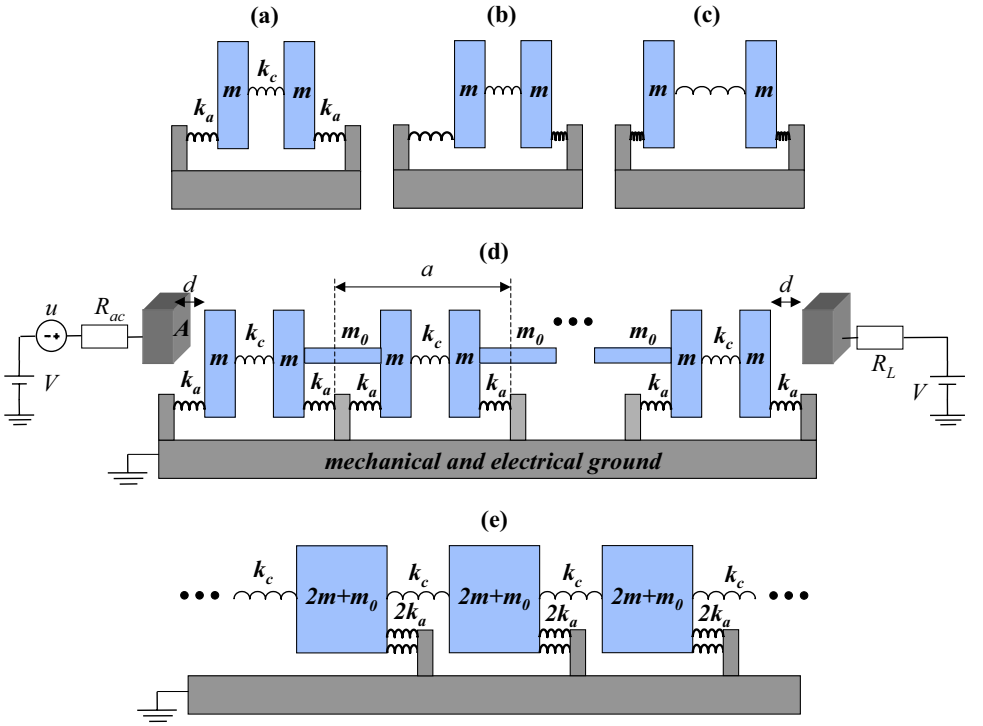

Figure 16: (a) An elementary two-mode resonator with (b) symmetric and (c) antisymmetric eigenmodes. (d) Delay line consisting of capacitive input (left) and output (right) transducers with gap d and a chain of coupled resonators. Except for the ends of the chain, the waveguide can be modelled as shown in (e). Losses are not indicated.

weak inter-stage coupling spring, much lower characteristic impedances can be obtained than for the solid-rod waveguide of Sec. 3.1. However, not as high signal frequencies can be used than with bulk-wave propagation. In what follows, damping is not considered in the analytical work but is included in the numerical simulations.

The elementary resonator of Fig. 16 has two fundamental modes of vibration with resonance frequencies

$$\omega_s = \sqrt{\frac{k_a}{m}} \tag{43 a}$$

$$\omega_a = \sqrt{\frac{2k_c + k_a}{m}}. \tag{43 b}$$

In the symmetric mode with resonance frequency ω_s (43 a), the masses move in phase while in the antisymmetric mode with frequency ω_a (43 b), there is a 180° phase difference between the mass motions. A useful parameter is the ratio of the strength of the anchoring spring, k_a, to that of the coupling spring, k_c, determined as $K \equiv k_a/k_c = 2/\left[(\omega_a/\omega_s)^2 - 1\right]$. For a particular resonator

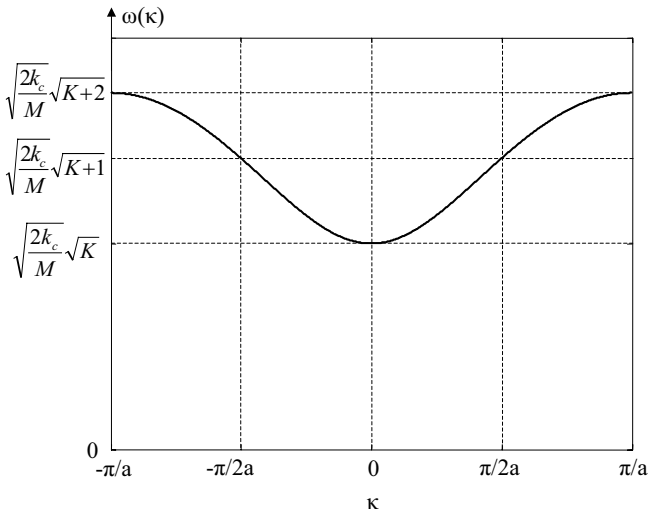

Figure 17: Dispersion relation for the anchored spring-mass chain of Fig. 16.

geometry, the ratio of the resonance frequencies is obtained, for example, from FEM eigenmode analysis or from measurements.

A periodic chain of coupled resonators can vibrate and carry signals at frequencies consistent with the dispersion relation, $\omega(\kappa)$, that gives the frequency, ω, as a function of the wave vector, $\kappa \equiv 2\pi/\lambda$, where λ is the wavelength. For the anchored chain of Fig. 16, the dispersion relation is found as a generalization of the familiar text-book result for periodic unanchored (free) chains [99]. One obtains for the anchored chain

$$\omega(\kappa) = \sqrt{\frac{2k_c}{M}}\sqrt{1-\cos(\kappa a)+K}, \tag{44}$$

where $M \equiv 2m + m_0$ is the total coupled-resonator mass, a is the period of the chain and the wave vector, $\kappa \in [-\pi/a, \pi/a]$, is restricted to the first Brillouin zone [99]. The dispersion relation (44) is illustrated in Fig. 17. As opposed to the low-pass character of free chains, the nonzero k_a forbids zero-frequency oscillations and results in passband response.

Group velocity for signal propagation along the chain is found from (44) as $v_g = \partial\omega/\partial\kappa$, and it is seen to differ from the phase velocity $v_{\rm ph} = \omega/\kappa$. For the center frequency $\omega_0 = 2\pi f_0$ and bandwidth $\Delta\omega = 2\pi\Delta f$ of the line one finds

$$\omega_0 = \omega(\frac{\pi}{2a}) = \sqrt{\frac{2k_c}{M}}\,\sqrt{K+1} \tag{45 a}$$

$$\Delta\omega = \omega(\frac{\pi}{a}) - \omega(0) = \sqrt{\frac{2k_c}{M}}\left(\sqrt{K+2} - \sqrt{K}\right). \tag{45 b}$$

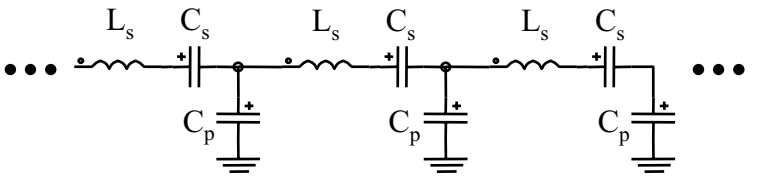

Figure 18: Electrical-equivalent model for the spring-mass-chain transmission line in Fig. 16 for center-band operation.

At the center of the passband, one obtains for the phase and group velocities

$$v_{\rm ph}^0 \equiv \left.\frac{\omega}{\kappa}\right|_{\omega_0} = \frac{2a}{\pi}\sqrt{\frac{2k_c}{M}}\sqrt{K+1} \tag{46 a}$$

$$v_g^0 \equiv \left.\frac{\partial\omega}{\partial\kappa}\right|_{\omega_0} = \frac{a}{2}\sqrt{\frac{2k_c}{M}}\,\frac{1}{\sqrt{K+1}} \tag{46 b}$$

illustrating clearly the dispersive character of the spring-mass chain.

Solving for the propagation constant κa in (44) and expanding its square as a power series with respect to ω^2 around the passband center frequency, allowes one to identify the elements of the electrical-equivalent circuit of the transmission line as depicted in Fig. 18 (see, for example, [100]), where

$$L_s = \frac{M}{\eta^2} \tag{47 a}$$

$$C_s = \frac{\pi\eta^2}{2k_c\,[\pi(1+K)-(\pi/2)^2]} \tag{47 b}$$

$$C_p = \frac{\pi\eta^2}{2k_c}\ . \tag{47 c}$$

Consequently, one finds for the characteristic impedance of the line

$$Z_c = \sqrt{\frac{Z_s}{Y_p}} = \frac{\sqrt{k_c M}}{\eta^2\sqrt{2(K+1)}}, \tag{48}$$

where $Z_s = j\omega L_s + 1/(j\omega C_s)$ is the series impedance and $Y_p = j\omega C_p$ is the shunt admittance in Fig. 18.

Increasing the strength of the anchoring spring, k_a, with respect to that of the coupling spring, k_c, increases the center frequency (45 a) and phase velocity (46 a) while decreasing the bandwidth (45 b), group velocity (46 b) and the characteristic impedance (48) that, typically, is much higher than 50 Ω with electrostatic coupling. Furthermore, for higher K, the variation of the group velocity as a function of frequency at the band center is reduced. For good signal coupling and long delays, it is thus desirable to have K as high as possible.

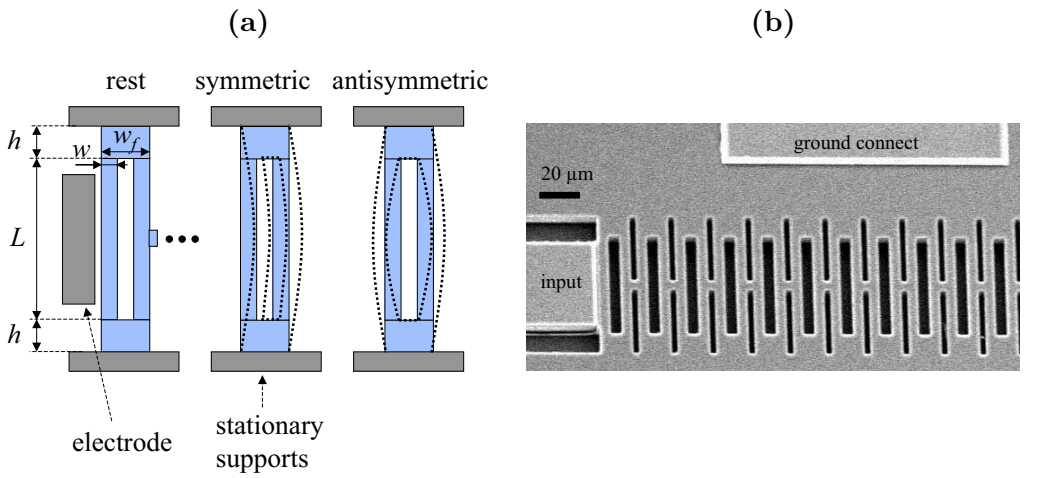

Figure 19: (a) Schematic of a resonator-chain design with an elementary tuning-fork resonator having symmetric and antisymmetric eigenmodes. Here, in particular, $w = 5$ μm, $w_f = 15$ μm and $L = 50$ μm. (b) SEM micrograph of a fabricated structure.

3.2.1 Measurements of Test Structures

The theory for the spring-mass-chain transmission lines is validated in Publication VI with measurements of fabricated narrow-gap waveguides of various lengths having different resonator structures. Figure 19 illustrates one of the designs that is discussed in detail in Publication VI. Figure 20 shows a measurement result and an Aplac® simulation fit for the response of the waveguide of Fig. 19 composed of 80 elementary two-mode resonators in series with a period of $a = 17.5$ μm. The numerical result that reasonably well fits the measurement is obtained by varying the parameters of the device. In particular, one finds for the quality factor of the elementary resonators $Q = 8000$, spring-constant ratio $K = 8.5$ and gap $d = 230$ nm corresponding to a group velocity of $v_g^0 = 70$ m/s and a characteristic impedance of $Z_c = 6$ MΩ. The passband ripple and high loss are due to impedance mismatch at the input and output of the waveguide. Matched termination would require the source and load impedances to equal the characteristic impedance. However, practical matching also requires the transducer (Z_0), bonding-pad (Z_{pad}) and parasitic feed-through (Z_{thr}) impedances to be smaller than Z_c.

3.2.2 Minimizing the Characteristic Impedance

As shown above, the MEMS resonator-chain delay lines enable record high acoustic time delays in a given physical size. However, to facilitate matched source and load termination for the line and to avoid using a differential readout, a much lower characteristic impedance, well below the pad, feed-through and transducer impedances, is needed than what was obtained above. As shown by (48) this can

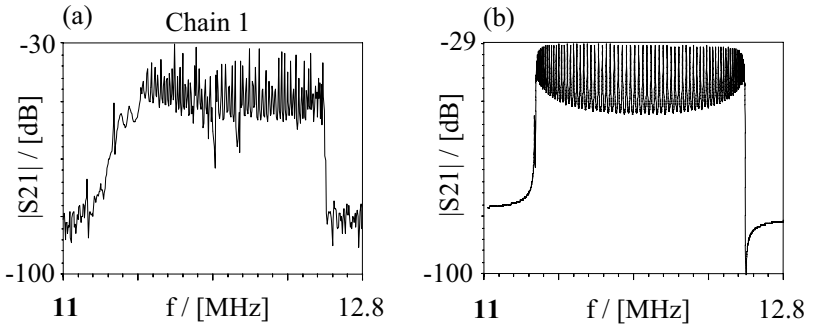

Figure 20: Measured (a) and simulated (b) response of the transmission line of Fig. 19 with 80 resonators.

be achieved by enhancing the coupling, η, and by strenghtening the anchoring spring, k_a, with respect to the coupling spring, k_c, (larger K). Reducing the anchoring height, h, in Fig. 19 to 5 μm, doubling the beam separation ($w_f \rightarrow 20\mu$m) and taking the narrowing of the structures in fabrication into account in the design, a much higher spring-constant ratio of $K = 74$ is expected. For good signal coupling, it is also important to design the first and last resonator in the chain to compensate for the electrical spring softening as well as for the stiffening of the first and last beams due to the capacitive coupling occuring over the transducer area as opposed to the point-force inter-resonator coupling along the chain. If, in addition, the transducer gap is reduced to $d = 100$ nm, a delay line with a period of $a = 22.5$ μm, estimated characteristic impedance of $Z_c = 22$ kΩ, bandwidth of $\Delta f = 185$ kHz and group velocity of $v_g^0 = 13$ m/s can be obtained with a bias voltage of 30 V ($V_{\rm pi} = 38$ V (12 a)).

Figure 21 shows the simulated response and group delay for a low-impedance chain of 80 resonators with reduced pad ($C_{\rm pad} = 91$ fF $\Rightarrow Z_{\rm pad} = 127$ kΩ) and feed-through capacitances ($C_{\rm thr} = 8$ fF $\Rightarrow Z_{\rm thr} = 1.3$ MΩ) that are likely obtainable with wafer-level vacuum packaging and IC integration. The transducer capacitance is $C_0 = 37$ fF corresponding to $Z_0 = 308$ kΩ. Consequently, the characteristic impedance of the transmission line is much lower than $Z_{\rm pad}$, $Z_{\rm thr}$ and Z_0 as required by good signal coupling. To have a flat group delay at the band center, resistive source and load termination to $R_L = 14$ kΩ is used that is somewhat lower than the estimated characteristic impedance of 22 kΩ. Higher pad and feed-through capacitances result in passband ripple and increased insertion loss if the characteristic impedance is not simultaneously further lowered.

Figure 22 illustrates a low-power transponder terminal, communicating with on-off keying, for example, in a low-datarate sensor application. Here, the reader sends an RF pulse to the sensor in which the pulse is either retransmitted back to the reader (bit 1) or shunted to ground (bit 0). Utilizing the above low-impedance design, for a datarate of 80 kb/s, one could use a delay line of 12 μs time delay (chain of 7 resonators) and a time pulse of $\Delta T_{\rm pulse} = 10$ μs.

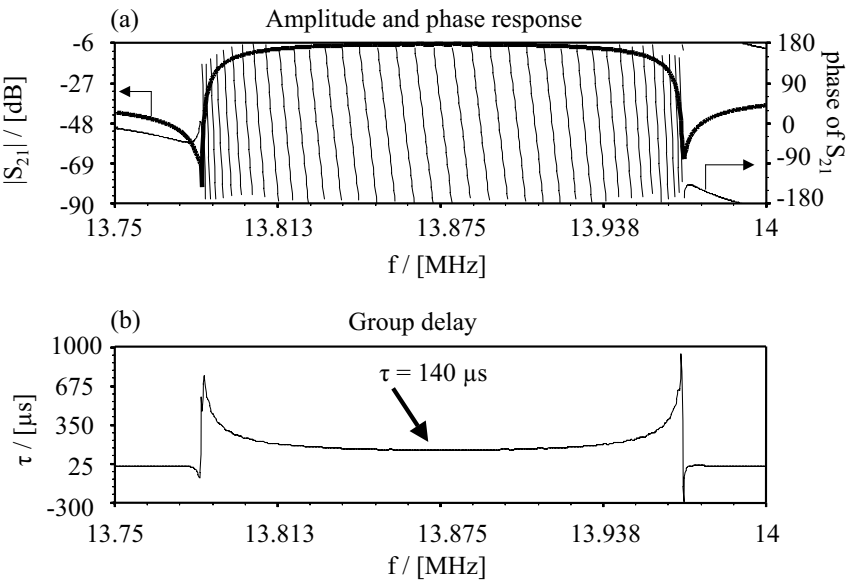

Figure 21: Simulated response (a) and group delay (b) for the low-impedance delay line with 14 kΩ source and load impedance. In (a) the thick line is for the amplitude and the thin line for the phase of S_{21}.

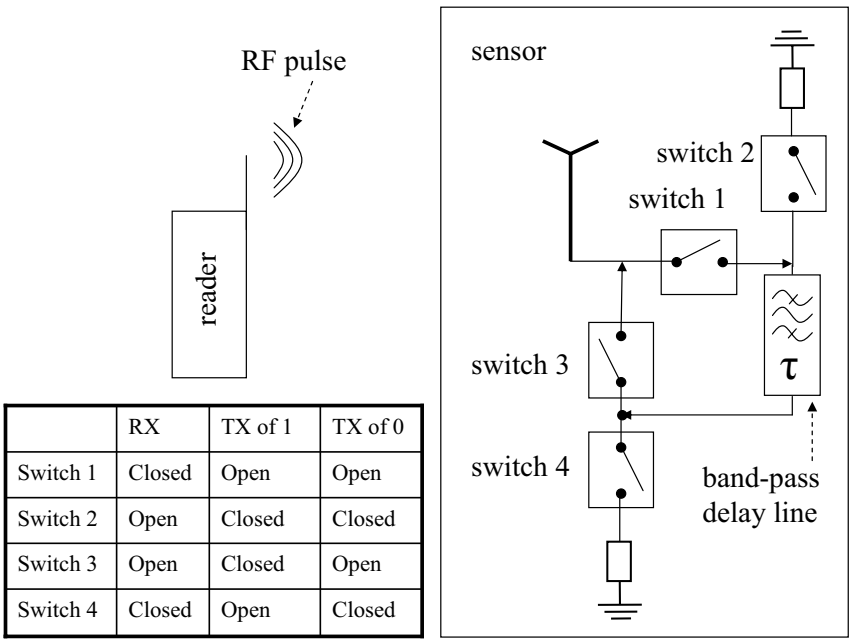

	RX	TX of 1	TX of 0
Switch 1	Closed	Open	Open
Switch 2	Open	Closed	Closed
Switch 3	Open	Closed	Open
Switch 4	Closed	Open	Closed

Figure 22: Schematic of a simple delay-line transponder for low-power low-datarate communication in sensor applications. The switch states in RX and TX are indicated in the table. Switch 2 is needed to have a proper source and load termination for the delay line at all times.

4 Discussion on Frequency Scaling

It is of interest to consider the scaling of the device properties as a function of frequency. In single-crystal bulk silicon, the attenuation factor at $f = 1$ GHz for longitudinal waves in the cube-edge direction is $\alpha = 1000$ dB/m/$(20 \log_{10} e) \sim f^2$ [97]. This results in the scaling of the acoustic quality factor as $Q = \pi f/(v\alpha) \sim f^{-1}$, where v is the wave velocity [97]. For $f = 1$ GHz, one obtains $Q = 3200$ which, however, is somewhat exceeded by the state-of-the-art silicon MEMS resonators [37]. Let us now consider three different bulk-acoustic (BAW) resonators in the circuit of Fig. 12 with a capacitive load: i) the 1D ring resonator of Fig. 13 with only the width x scaling as $x \sim f^{-1}$, ii) the 2D plate of [8] and Fig. 3 (c) with the lateral dimensions but not the SOI thickness scaling as $\sim f^{-1}$, and iii) a 3D resonator for which all the dimensions scale as $\sim f^{-1}$ as considered in [32]. We further assume that i) the bias and AC voltages, transducer gap, $R_{\rm ac}$, $R_L \gg 1/(\omega C_L)$, and C_L do not scale with the frequency, ii) the transducer impedance Z_0 is much higher than the source impedance $R_{\rm ac}$, and iii) the bias voltage is much lower than the pull-in voltage. With these assumptions, we find the scaling exponents of relevant resonator properties that are given in Table 4. Here the same SIR scaling is obtained both for (33) outside the passband with $\Delta\omega \sim \omega/Q$ and for (34) within the band. Although scaling of the motional impedance depends on the chosen geometry, the nonlinearity-limited critical amplitude, $x_{0,\rm c}$, [32], pull-in voltage, SIR and voltage gain have more universal exponents. It is interesting to note that increasing the frequency enhances SIR but degrades the voltage gain.

Table 4: Frequency scaling exponents of resonator properties.

symbol	k	m	Q	C_0	η	R_m	$x_{0,\rm c}$	$V_{\rm pi}$	SIR	G_V
1D ring	1	-1	-1	0	0	1	-1/2	1/2	2	-2
2D plate	0	-2	-1	-1	-1	2	-1/2	1/2	2	-2
3D	-1	-3	-1	-2	-2	3	-1/2	1/2	2	-2

For the spring-mass-chain delay lines, the frequency scaling can be estimated based on the clamped-clamped flexural-beam resonator for which $m \sim wHL$ and $k \sim H(w/L)^3$ [32]. For $w \sim L \sim f^{-1}$, $H \sim f^0$ and $w \sim L \sim H \sim f^{-1}$, the resonator scaling is the same as for the 2D-plate resonator and the 3D resonator in Table 4, respectively. Assuming that both the anchoring and the coupling springs of the tuning forks scale as k (keeping the spring-constant ratio K constant), the group velocity is found not to scale with frequency. The characteristic impedance, on the other hand, scales as $Z_c \sim f$ for $H \sim f^0$ while for $H \sim f^{-1}$ we have $Z_c \sim f^2$. Thus for higher frequencies, the impedance matching becomes increasingly challenging, especially if the device-layer thickness needs to be reduced.

5 Conclusions

Microelectromechanical systems are beginning to provide a competitive alternative for many components used in radio architectures of commercial battery-powered communication devices. Several start-up companies are commercializing RF MEMS switches, filters and oscillators with the MEMS switch already being sold by a few companies such as TeraVicta. The MEMS switch has a better contact resistance than, for example, CMOS or GaAs switches but the reliability still needs to be improved and the voltage levels of capacitively-actuated switches need to be lowered. The MEMS oscillator offers clear size and integration advantages compared to conventional quartz oscillators. They are being commercialized, for example, by Discera and SiTime as well as by VTT and VTI Technologies. Unlike a quartz oscillator, however, the MEMS oscillator requires external temperature compensation. Piezoelectrically-actuated FBAR filters, that often are also considered as MEMS devices, have already replaced SAW filters in some cell phones. Focusing on the research questions stated in Sec. 1.6, this thesis has created new scientific knowledge that is vital for RF MEMS filter design and introduced a new kind of MEMS delay line that can be used, for example, in time-delay radios.

Filter Distortion: In this thesis, intermodulation properties of capacitively-coupled bandpass MEMS filters were analytically solved in closed form and the trade-off between linearity and insertion loss was quantified. The theoretical results were verified in circuit simulations as well as in measurements. Also mechanical nonlinearities were included although, typically for good coupling, the capacitive nonlinearity is the dominant source of intermodulation. The theory was first formulated for weakly-coupled single-stage filters and then generalized to strong coupling (low motional resistance and low insertion loss) and to higher-order filters. What was not taken into account was the fact that for strong interferers present within the passband, Duffing effect can result in signal compression that limits the filter performance.

The obtained formulas are more generally applicable than the previously published results. In particular, the results of this thesis showed good accuracy also close to the passband edge and revealed the unsymmetry in intermodulation between positive and negative frequency separations of the interferers from the passband. In [57], an analytical result for intermodulation in a thermally actuated MEMS resonator is given that is in exact agreement with (28) if all terms other than the one originating from the third-order mechanical nonlinearity in the denominator are ignored. However, [57] uses an interferometric readout, which is not suitable for commercial communication applications, and does not consider insertion loss that is of importance in filter design.

After the analysis, a systematic procedure to design MEMS filters was formulated. The conventional resistive 50-Ω source and load termination was shown to typically result in a high insertion loss if good linearity is required with low-voltage

operation. Consequently, it was found desirable to utilize the high resonator Q for voltage gain that is enabled by capacitive load termination at the filter output. This is possible in integrated receiver architectures, where 50 Ω transmission lines are not needed between the antenna and the filter and between the filter and the LNA. With such an approach, MEMS filters could be used to construct a receiver front-end having a bank of narrow-band (ultimately channel-select) filters with different passbands to cover all the RX channels as suggested in [15]. Taking also the noise properties of MEMS resonators [79] into account in the filter design as well as practical demonstration of the optimized filters are left for future work.

Using dielectric media other than air/vacuum for the electrode gap has potential in lowering the electrical impedance and thus alleviating the need for a very narrow gap [14]. The analysis procedure derived in this thesis can be directly applied for such devices as long as an appropriate value for permittivity is used.

Delay Lines: Usage of electrostatically-actuated longitudinal waves in a silicon rod for signal transmission was analyzed in detail and challenges due to high impedance levels were quantified. For HF frequencies, a MEMS resonator-chain structure with record slow signal propagation was presented enabling miniaturization of time-delay components. The properties of the delay line were theoretically analyzed and the theory was verified in measurements with fabricated devices consisting of up to 80 series-connected MEMS resonators. The fabricated delay lines had still too high characteristic impedances for practical applications, but careful design can result in impedance levels of few kiloohms that can be acceptable in integrated solutions with properly-designed impedance transformers. To reach higher frequencies, the lateral resonator dimensions have to be scaled down which, however, weakens the capacitive coupling (increases the line impedance) unless the reduced transducer area is compensated for by a smaller gap, thicker SOI device layer or a higher bias voltage. In addition to a group velocity that is much lower than that for other acoustic delay lines (SAW or BAW), the MEMS line is characterized by a narrow-band response. This can be utilized in applications that would otherwise require a separate bandpass filter as in wireless transponder radios of sensors for which a possible structure was suggested in Fig. 22. Compared to SAW devices, MEMS can dramatically reduce the size of the radio unit. Demonstration of such a transponder is left for future work.

In the fabrication of capacitive MEMS filters and delay lines, several challenges remain: i) The gap should be reduced to well below 100 nm to enable low-enough bias voltages. High-permittivity dielectrics can provide an alternative approach to better coupling. ii) The dimensional tolerances of the devices, manufactured with lithography, are poor leading to wide variations in the center frequency. iii) The parasitic feed through-capacitance may limit the filtering performance and a differential readout may be required. If these challenges are met, MEMS filters and transmission lines can have a large economic potential.

References

[1] Ari T Alastalo, Mika Koskenvuori, Heikki Seppä, and James Dekker, "A Micromechanical Resonating RF Mixer," in *34th European Microwave Conference*, 2004, pp. 1297–1300.

[2] Ari Alastalo, Jukka Kyynäräinen, Heikki Seppä, Anu Kärkkäinen, Nadine Pesonen, Manu Lahdes, Tauno Vähä-Heikkilä, Panu Pekko, and James Dekker, "Wideband microwave power sensor based on MEMS technology," in *Conference on Precision Electromagnetic Measurements (CPEM 2004)*, 2004, pp. 115–116.

[3] Ari T. Alastalo and Ville Kaajakari, "Designing Capacitively Coupled Microelectromechanical Filters," in *IEEE International Ultrasonics Symposium*, 2005, pp. 1588–1591.

[4] Ville Kaajakari, Ari T. Alastalo, and Tomi Mattila, "Electrostatic transducers for micromechanical resonators: free space and solid dielectric," *IEEE Trans. Ultrason., Ferroelect., Freq. Contr.*, 2006, in press.

[5] John R. Vig, "Introduction to Quartz Frequency Standards," http://www.ieee-uffc.org/freqcontrol/quartz/vig/vigtoc.htm, 1992.

[6] Robert Weigel, David P. Morgan, John M. Owens, Arthur Ballato, Kenneth M. Lakin, Ken-ya Hashimoto, and Clemens C. W. Ruppel, "Microwave Acoustic Materials, Devices, and Applications," *IEEE Trans. Microwave Theory Tech.*, vol. 50, no. 3, pp. 738–749, 2002.

[7] Markku Ylilammi, Juha Ellä, Meeri Partanen, and Jyrki Kaitila, "Thin Film Bulk Acoustic Wave Filter," *IEEE Trans. Ultrason., Ferroelect., Freq. Contr.*, vol. 49, no. 4, pp. 535–539, 2002.

[8] V. Kaajakari, T. Mattila, A. Oja, J. Kiihamäki, and H. Seppä, "Square-Extensional Mode Single-Crystal Silicon Micromechanical Resonator for Low Phase Noise Oscillator Applications," *IEEE Electron Device Lett.*, vol. 25, no. 4, pp. 173–175, 2004.

[9] Peter Gammel, Georg Fischer, and Jérémie Bouchaud, "RF MEMS and NEMS Technology, Devices, and Applications," *Bell Labs Technical Journal*, vol. 10, no. 3, pp. 29–59, 2005.

[10] S. Lucyszyn, "Review of radio frequency microelectromechanical systems technology," *IEE Proc.-Sci. Meas. Technol.*, vol. 151, no. 2, pp. 93–103, 2004.

[11] Tauno Vähä-Heikkilä, "MEMS tuning and matching circuits, and millimeter wave on-wafer measurements," D.Sc. thesis, Helsinki University of Technology, 2006, VTT Publications 596, Espoo 2006.

[12] Siavash Pourkamali and Farrokh Ayazi, "Electrically Coupled MEMS Bandpass Filters: Part I: With Coupling Element," *Sensors and Actuators A*, vol. 122, no. 2, pp. 307–316, 2005.

[13] Siavash Pourkamali and Farrokh Ayazi, "Electrically Coupled MEMS Bandpass Filters: Part II: Without Coupling Element," *Sensors and Actuators A*, vol. 122, no. 2, pp. 317–325, 2005.

[14] Hengky Chandrahalim, Dana Weinstein, Lih Feng Cheow, and Sunil A. Bhave, "Channel-Select Micromechanical Filters Using High-K Dielectrically Transduced MEMS Resonators," in *IEEE International Conference on Micro Electro Mechanical Systems, (MEMS 2006)*, 2006, pp. 894–897.

[15] Clark T.-C. Nguyen, "Frequency-Selective MEMS for Miniaturized Low-Power Communication Devices," *IEEE Trans. Microwave Theory Tech.*, vol. 47, no. 8, pp. 1486–1503, 1999.

[16] Liwei Lin, Roger T. Howe, and Albert P. Pisano, "Microelectromechanical Filters for Signal Processing," *J. Microelectromech. Syst.*, vol. 7, no. 3, pp. 286–294, 1998.

[17] Milton Feng, Shyh-Chiang Shen, David C. Caruth, and Jian-Jang Huang, "Device Technologies for RF Front-End Circuits in Next-Generation Wireless Communications," *Proc. IEEE*, vol. 92, no. 2, pp. 354–375, 2004.

[18] Harrie A C Tilmans, Walter De Raedt, and Eric Beyne, "MEMS for wireless communications: 'from RF-MEMS components to RF-MEMS-SiP'," *J. Micromech. Microeng.*, vol. 13, pp. S139–S163, 2003.

[19] Hee-Gook Lee, Jae Yeong Park, Jong Uk Bu, and Youngjoo Yee, "MEMS Technology for Advanced Telecommunication Applications," *International Journal of High Speed Electronics and Systems*, vol. 12, no. 2, pp. 215–233, 2002.

[20] J Jason Yao, "RF MEMS from a device perspective," *J. Micromech. Microeng.*, vol. 10, pp. R9–R38, 2000.

[21] Vijay K. Varadan, K. J. Vinoy, and K. A. Jose, *RF MEMS and Their Applications*, John Wiley & Sons Ltd, 2003.

[22] Gabriel M. Rebeiz, *RF MEMS, Theory, Design, and Technology*, John Wiley & Sons, Inc., 2003.

[23] Stephen Lewis, Susan Alie, Dr. Timothy Brosnihan, Craig Core, Teresa Core, Dr. Roger Howe, John Geen, David Hollocher, Dr. Michael Judy, Jack Memishian, Kieran Nunan, Dr. Richard Paine, Steven Sherman, Bob Tsang, and Bruce Wachtmann, "Integrated Sensor and Electronics Processing for >10ˆ8 "iMEMS" Inertial Measurement Unit Components," in *IEEE International Electron Device Meeting (IEDM'03)*, 2003, pp. 39.1.1–39.1.4.

[24] D. F. Moore and R. R. A. Syms, "Recent developments in micromachined silicon," *Electronics & Communication Engineering Journal*, vol. 11, no. 6, pp. 261–270, 1999.

[25] A. Bruce Carlson, Paul B. Crilly, and Janet C. Rutledge, *Communication Systems*, McGraw-Hill, 4th edition, 2002.

[26] Heikki Seppä, Jukka Kyynäräinen, and Aarne Oja, "Microelectromechanical Systems in Electrical Metrology," *IEEE Trans. Instrum. Meas.*, vol. 50, no. 2, pp. 440–444, 2001.

[27] Luis Fernández, Javier Sesé, Remco Wiegerink, Jaap Flokstra, Henri Jansen, and Miko Elwenspoek, "Radio Frequency Power Sensor Based on MEMS Technology with Ultra Low Losses," in *IEEE International Conference on Micro Electro Mechanical Systems, (MEMS 2005)*, 2005, pp. 191–194.

[28] Ark-Chew Wong and Clark T.-C. Nguyen, "Micromechanical Mixer-Filters ("Mixlers")," *J. Microelectromech. Syst.*, vol. 13, no. 1, pp. 100–112, 2004.

[29] Clark T.-C. Nguyen, "Method and apparatus for generating a signal having at least one desired output frequency utilizing a bank of vibrating micromechanical devices," United States Patent 6,577,040, 2003.

[30] B.P. Otis, Y.H. Chee, R. Lu, N.M. Pletcher, and J.M. Rabaey, "An Ultra-Low Power MEMS-Based Two-Channel Transceiver for Wireless Sensor Networks," in *Symposium On VLSI Circuits*, 2004, pp. 20–23.

[31] L. D. Landau and E. M. Lifshitz, *Mechanics*, Butterworth-Heinemann, 1999.

[32] V. Kaajakari, T. Mattila, A. Oja, and H. Seppä, "Nonlinear Limits for Single-Crystal Silicon Microresonators," *J. Microelectromech. Syst.*, vol. 13, no. 5, pp. 715–724, 2004.

[33] Sunil A. Bhave, Di Gao, Roya Maboudian, and Roger T. Howe, "Fully-Differential Poly-SiC Lamé-Mode Resonator and Checkerboard Filter," in *IEEE International Conference on Micro Electro Mechanical Systems, (MEMS 2005)*, 2005, pp. 223–226.

[34] T. Mattila, J. Kiihamäki, T. Lamminmäki, O. Jaakkola, P. Rantakari, A. Oja, H. Seppä, H. Kattelus, and I. Tittonen, "12 MHz Micromechanical Bulk Acoustic Mode Oscillator," *Sensors and Actuators A*, vol. 101, no. 1-2, pp. 1–9, 2002.

[35] T. Mattila, O. Jaakkola, J. Kiihamäki, J. Karttunen, T. Lamminmäki, P. Rantakari, A. Oja, H. Seppä, H. Kattelus, and I. Tittonen, "14 MHz Micromechanical Oscillator," *Sensors and Actuators A*, vol. 97-98, pp. 497–502, 2002.

[36] M. Agarwal, K. K. Park, M. Hopcroft, S. Chandorkar, R. N. Candler, B. Kim, R. Melamud, G. Yama, B. Murmann, and T. W. Kenny, "Effects of Mechanical Vibrations and Bias Voltage Noise on Phase Noise of MEMS Resonator Based Oscillators," in *IEEE International Conference on Micro Electro Mechanical Systems, (MEMS 2006)*, 2006, pp. 154–157.

[37] Sheng-Shian Li, Yu-Wei Lin, Yuan Xie, Zeying Ren, and Clark T.-C. Nguyen, "Micromechanical "Hollow-Disk" Ring Resonators," in *17th International IEEE Conference on Micro Electro Mechanical Systems, (MEMS 2004)*, 2004, pp. 821–824.

[38] Emmanuel P. Quévy, Alvaro San Paulo, Erol Basol, Roger T. Howe, Tsu-Jae King, and Jeffrey Bokor, "Back-End-of-Line Poly-SiGe Disk Resonators," in *IEEE International Conference on Micro Electro Mechanical Systems, (MEMS 2006)*, 2006, pp. 234–237.

[39] Jing Wang, Zeying Ren, and Clark T.-C. Nguyen, "1.156-GHz Self-Aligned Vibrating Micromechanical Disk Resonator," *IEEE Trans. Ultrason., Ferroelect., Freq. Contr.*, vol. 51, no. 12, pp. 1607–1628, 2004.

[40] Jing Wang, James E. Butler, Tatyana Feygelson, and Clark T.-C. Nguyen, "1.51 GHz Nanocrystalline Diamond Micromechanical Disk Resonator With Material-Mismatched Isolating Support," in *International IEEE Conference on Micro Electro Mechanical Systems, (MEMS 2004)*, pp. 641–644.

[41] Florian W Beil, Laura Pescini, Eva Höhberger, Andreas Kraus, Artur Erbe, and Robert H Blick, "Comparing schemes of displacement detection and subharmonic generation in nanomachined mechanical resonators," *Nanotechnology*, vol. 14, pp. 799–802, 2003.

[42] Jaume Verd, G. Abadal, J. Teva, María Villarroya Gaudó, Arantxa Uranga, Xavier Borrisé, Francesca Campabadal, Jaume Esteve, Eduardo Figueras Costa, Francesc Pérez-Murano, Zachary J. Davis, Esko Forsén, Anja Boisen, and Nuria Barniol, "Design, Fabrication, and Characterization of a Submicroelectromechanical Resonator With Monolithically Integrated CMOS

Readout Circuit," *J. Microelectromech. Syst.*, vol. 14, no. 3, pp. 508–519, 2005.

[43] Harrie A C Tilmans, "Equivalent circuit representation of electromechanical transducers: I. Lumped-parameter systems," *J. Micromech. Microeng.*, vol. 6, pp. 157–176, 1996.

[44] A Q Liu, M Tang, A Agarwal, and A Alphones, "Low-loss lateral micromachined switches for high frequency applications," *J. Micromech. Microeng.*, vol. 15, pp. 157–167, 2005.

[45] Seong-Dae Lee, Byoung-Chul Jun, Sam-Dong Kim, and Jin-Koo Rhee, "A Novel Pull-Up Type RF MEMS Switch With Low Actuation Voltage," *IEEE Microwave Wireless Compon. Lett.*, vol. 15, no. 12, pp. 856–858, 2005.

[46] Jaewoo Lee, Chan Han Je, Sungweon Kang, and Chang-Auck Choi, "A Low-Loss Single-Pole Six-Throw Switch Based on Compact RF MEMS Switches," *IEEE Trans. Microwave Theory Tech.*, vol. 53, no. 11, pp. 3335–3344, 2005.

[47] Hee-Chul Lee, Jae-Hyoung Park, Jae-Yeong Park, Hyo-Jin Nam, and Jong-Uk Bu, "Design, fabrication and RF performances of two different types on piezoelectrically actuated Ohmic MEMS switches," *J. Micromech. Microeng.*, vol. 15, pp. 2098–2104, 2005.

[48] Meichun Ruan and Charles B. Wheeler, "Latching Micromagnetic Relays," *J. Microelectromech. Syst.*, vol. 10, no. 4, pp. 511–517, 2001.

[49] Il-Joo Cho, Taeksang Song, Sang-Hyun Baek, and Euisik Yoon, "A Low-Voltage and Low-Power RF MEMS Series and Shunt Switches Actuated by Combination of Electromagnetic and Electrostatic Forces," *IEEE Trans. Microwave Theory Tech.*, vol. 53, no. 7, pp. 2450–2457, 2005.

[50] Daniel Saias, Philippe Robert, Samuel Boret, Christophe Billard, Guillaume Bouche, Didier Belot, and Pascal Ancey, "An Above IC MEMS RF Switch," *IEEE J. Solid-State Circuits*, vol. 38, no. 12, pp. 2318–2324, 2003.

[51] Brett Piekarski, Don DeVoe, Madan Dubey, Roger Kaul, and John Conrad, "Surface micromachined piezoelectric resonant beam filters," *Sensors and Actuators A*, vol. 91, pp. 313–320, 2001.

[52] B. Antkowiak, J.P. Gorman, M. Varghese, D.J.D. Carter, and A.E. Duwel, "Design of a High-Q, Low-Impedance, GHz-Range Piezoelectric MEMS Resonator," in *The 12th International Conference on Solid State Sensors, Actuators and Microsystems, (Transducers'03)*, 2003, pp. 841–846.

[53] Gianluca Piazza, Reza Abdolvand, and Farrokh Ayazi, "Voltage-tunable piezoelectrically-transduced single-crystal silicon resonators on SOI substrate," in *16th IEEE International Conference on Micro Electro Mechanical Systems, (MEMS 2003)*, 2003, pp. 149–152.

[54] Le Yan, Jian Wu, and William C. Tang, "A 1.14 GHz Piezoelectrically Transduced Disk Resonator," in *18th IEEE International Conference on Micro Electro Mechanical Systems, (MEMS 2005)*, 2005, pp. 203–206.

[55] Arthur Erbe and Robert H. Blick, "Silicon-on-Insulator Based Nanoresonators for Mechanical Mixing at Radio Frequencies," *IEEE Trans. Ultrason., Ferroelect., Freq. Contr.*, vol. 49, no. 8, pp. 1114–1117, 2002.

[56] Tarik Bourouina, Amalia Garnier, and Hiroyuki Fujita, "Effect of direct current bias field and alternating current excitation field on vibration amplitudes and resonance frequencies of a magnetostrictively actuated bimorph microresonator," *J. Appl. Phys.*, vol. 91, no. 1, pp. 112–120, 2002.

[57] Robert B. Reichenbach, Maxim Zalalutdinov, Keith L. Aubin, Richard Rand, Brian H. Houston, Jeevak M. Parpia, and Harold G. Craighead, "Third-Order Intermodulation in a Micromechanical Thermal Mixer," *J. Microelectromech. Syst.*, vol. 14, no. 6, pp. 1244–1252, 2005.

[58] Sunil A. Bhave and Roger T. Howe, "Internal Electrostatic Transduction for Bulk-Mode MEMS Resonators," in *Solid State Sensor, Actuator and Microsystems Workshop*, Hilton Head, SC, 2004, pp. 59–60.

[59] Sunil A. Bhave and Roger T. Howe, "Silicon nitride-on-silicon bar resonator using internal electrostatic transduction," in *The 13th International Conference on Solid-State Sensors, Actuators and Microsystems, (Transducers'05)*, 2005, pp. 2139–2142.

[60] William C. Tang, Tu-Cuong H. Nguyen, and Roger T. Howe, "Laterally Driven Polysilicon Resonant Microstructures," in *IEEE Conference on Micro Electro Mechanical Systems*, 1989, pp. 53–59.

[61] John R. Reitz, Frederick J. Milford, and Robert W. Christy, *Foundations of Electromagnetic Theory*, Addison Wesley, 3rd edition, 1980.

[62] L. Castañer, J. Pons, R. Nadal-Guardia, and A. Rodríguez, "Analysis of the extended operation range of electrostatic actuators by current-pulse drive," *Sensors and Actuators A*, vol. 90, pp. 181–190, 2001.

[63] Marc Madou, *Fundamentals of Microfabrication*, CRC Press, 1997.

[64] Jyrki Kiihamäki, "Fabrication of SOI micromechanical devices," D.Sc. thesis, Helsinki University of Technology, VTT Publications 559, Espoo 2005.

[65] James M. Bustillo, Roger T. Howe, and Richard S. Muller, "Surface Micromachining for Microelectromechanical Systems," *Proc. IEEE*, vol. 86, no. 8, pp. 1552–1574, 1998.

[66] N. Sepúlveda, D.M. Aslam, and J.P. Sullivan, "Polycrystalline Diamond RF MEMS Resonators with the Highest Quality Factors," in *IEEE International Conference on Micro Electro Mechanical Systems, (MEMS 2006)*, 2006, pp. 238–241.

[67] Robert F. Wiser, Juyong Chung, Mehran Mehregany, and Christian A. Zorman, "Polycrystalline Silicon-Carbide Surface-Micromachined Vertical Resonators - Part I: Growth Study and Device Fabrication," *J. Microelectromech. Syst.*, vol. 14, no. 3, pp. 567–578, 2005.

[68] Robert F. Wiser, Massood Tabib-Azar, Mehran Mehregany, and Christian A. Zorman, "Polycrystalline Silicon-Carbide Surface-Micromachined Vertical Resonators - Part II: Electrical Testing and Material Property Extraction," *J. Microelectromech. Syst.*, vol. 14, no. 3, pp. 579–589, 2005.

[69] Hideki Takeuchi, Emmanuel Quévy, Sunil A. Bhave, Tsu-Jae King, and Roger T. Howe, "Ge-Blade Damascene Process for Post-CMOS Integration of Nano-Mechanical Resonators," *IEEE Electron Device Lett.*, vol. 25, no. 8, pp. 529–531, 2004.

[70] Christian A. Zorman and Mehran Mehregany, "Silicon Carbide for MEMS and NEMS - An Overview," in *Sensors 2002*, 2002, pp. 1109–1114.

[71] Franz Laermer and Andrea Schilp, "Method for anisotropic plasma etching of substrates," United States Patent 5,498,312, 1996.

[72] Siavash Pourkamali and Farrokh Ayazi, "Fully Single Crystal Silicon Resonators with Deep-Submicron Dry-Etched Transducer Gaps," in *IEEE International Conference on Micro Electro Mechanical Systems, (MEMS 2004)*, 2004, pp. 813–816.

[73] Wan-Thai Hsu, John R. Clark, and Clark T.-C. Nguyen, "A sub-micron capacitive gap process for multiple-metal-electrode lateral micromechanical resonators," in *IEEE International Conference on Micro Electro Mechanical Systems, (MEMS 2001)*, 2001, pp. 349–352.

[74] Siavash Pourkamali, Akinori Hashimura, Reza Abdolvand, Gavin K. Ho, Ahmet Erbil, and Farrokh Ayazi, "High-Q Single Crystal Silicon HARPSS Capacitive Beam Resonators With Self-Aligned Sub-100-nm Transduction Gaps," *J. Microelectromech. Syst.*, vol. 12, no. 4, pp. 487–496, 2003.

[75] Emmanuel Quévy, Bernard Legrand, Dominique Collard, and Lionel Buchaillot, "Ultimate technology for micromachining of nanometric gap HF micromechanical resonators," in *IEEE International Conference on Micro Electro Mechanical Systems, (MEMS 2003)*, 2003, pp. 157–160.

[76] J. Kiihamäki, V. Kaajakari, H. Luoto, H. Kattelus, and M. Yli-Koski, "Fabrication of single crystal silicon resonators with narrow gaps," in *The 13th International Conference on Solid-State Sensors, Actuators and Microsystems, (Transducers'05)*, 2005, pp. 1354–1357.

[77] Kevin Y. Yasumura, Timothy D. Stowe, Eugene M. Chow, Timothy Pfafman, Thomas W. Kenny, Barry C. Stipe, and Daniel Rugar, "Quality Factors in Micron- and Submicron-Thick Cantilevers," *J. Microelectromech. Syst.*, vol. 9, no. 1, pp. 117–125, 2000.

[78] Ron Lifshitz and M. L. Roukes, "Thermoelactic damping in micro- and nanomechanical systems," *Phys. Rev. B*, vol. 61, no. 8, pp. 5600–5608, 2002.

[79] V. Kaajakari, Jukka K. Koskinen, and Tomi Mattila, "Phase Noise in Capacitively Coupled Micromechanical Oscillators," *IEEE Trans. Ultrason., Ferroelect., Freq. Contr.*, vol. 52, no. 12, pp. 2322–2331, 2005.

[80] J. R. Vig and Yoonkee Kim, "Noise in Microelectromechanical System Resonators," *IEEE Trans. Ultrason., Ferroelect., Freq. Contr.*, vol. 46, no. 6, pp. 1558–1565, 1999.

[81] A. N. Cleland and M. L. Roukes, "Noise processes in nanomechanical resonators," *J. Appl. Phys.*, vol. 92, no. 5, pp. 2758–2769, 2002.

[82] B. Razavi, *RF Microelectronics*, Prentice Hall, 1998.

[83] ETSI, "GSM global system for mobile communications," TS 145 005 V6.11.0 (2005-09).

[84] Reza Navid, John R. Clark, Mustafa Demirci, and Clark T.-C. Nguyen, "Third-order intermodulation distortion in capacitively-driven cc-beam micromechanical resonators," in *IEEE International Conference on Micro Electro Mechanical Systems, (MEMS 2001)*, 2001, pp. 228–231.

[85] T. Veijola and T. Mattila, "Modeling of Nonlinear Micromechanical Resonators and Their Simulation with the Harmonic-Balance Method," *International Journal of RF and Microwave Computer Aided Engineering*, vol. 11, no. 5, pp. 310–321, 2001.

[86] Jr. W. Weaver, S. Timoshenko, and D. Young, *Vibration Problems in Engineering*, Wiley, 5th edition, 1990.

[87] T. Lee, *The Design of CMOS Radio-Frequency Integrated Circuits*, Cambridge University Press, 1998.

[88] Leonhard M. Reindl, Alfred Pohl, Gerd Scholl, and Robert Weigel, "SAW-Based Radio Sensor Systems," *IEEE Sensors J.*, vol. 1, no. 1, pp. 69–78, 2001.

[89] Ram M. Narayanan, Wei Zhou, Kelvin H. Wagner, and Sangtaek Kim, "Acoustooptic Correlation Processing in Random Noise Radar," *IEEE Geosci. Remote Sensing Lett.*, vol. 1, no. 3, pp. 166–170, 2004.

[90] Leonhard Reindl, Clemens C. W. Ruppel, Stefan Berek, Ulrich Knauer, Martin Vossiek, Patric Heide, and Lutz Oréans, "Design, Fabrication, and Application of Precise SAW Delay Lines Used in an FMCW Radar System," *IEEE Trans. Microwave Theory Tech.*, vol. 49, no. 4, pp. 787–794, 2001.

[91] S. K. Salmon, "Practical Aspects of Surface-Acoustic-Wave Oscillators," *IEEE Trans. Microwave Theory Tech.*, vol. MTT-27, no. 12, pp. 1012–1018, 1979.

[92] Thomas E. Parker and Gary K. Montress, "Precision Surface-Acoustic-Wave (SAW) Oscillators," *IEEE Trans. Ultrason., Ferroelect., Freq. Contr.*, vol. 35, no. 3, pp. 342–364, 1988.

[93] D. Ciplys, R. Rimeika, A. Sereika, R. Gaska, M.S. Shur, J.W. Yang, and M.A. Khan, "GaN-based SAW delay-line oscillator," *Electronics Letters*, vol. 37, no. 8, pp. 545–546, 2001.

[94] J. H. Yin, K. X. Shen, Y. Shui, Z. L. Jiang, and S. P. He, "Modified SAW Diode Convolver," *Electronics Letters*, vol. 28, no. 2, pp. 172–174, 1992.

[95] Shiwei Zhao, Huaping Liu, and Zhi Tian, "A Decision-Feedback Autocorrelation Receiver for Pulsed Ultra-Wideband Systems," in *Proc. IEEE Radio and Wireless Conference*, 2004, pp. 251–254.

[96] D. M. Pozar, *Microwave Engineering*, Wiley, 2nd edition, 1998.

[97] B. A. Auld, *Acoustic Fields and Waves in Solids*, Krieger, 2nd edition, 1990.

[98] H. F. Pollard, *Sound Waves in Solids*, Pion Ltd., 1977.

[99] Neil W. Ashcroft and N. David Mermin, *Solid State Physics*, Saunders College Publishing, 1976.

[100] Simon Ramo, John R. Whinnery, and Theodore Van Duzer, *Fields and Waves in Communication Electronics*, John Wiley & Sons, 2nd edition, 1984.

APPENDIX 1

Electromechanical Instability

Electromechanical Instability

Increasing the bias voltage enhances the electrostatic coupling and lowers the typically very high impedance level of the MEMS resonator thus reducing insertion loss from a low-impedance source such as a 50-Ω generator. As shown in (22 c), the voltage bias also lowers the effective spring constant of the resonator. For large-enough bias, the resonator becomes unstable and is deflected against one of the stationary transducer electrodes (pull-in).

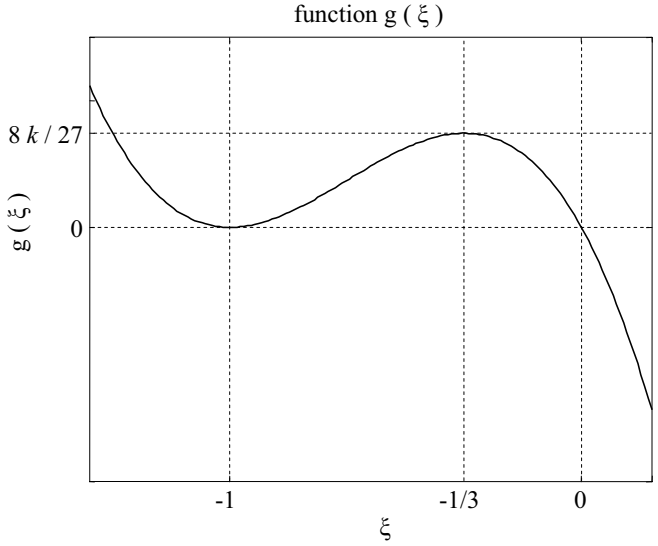

Figure 1: Function $g(\xi)$ in (2).

The pull-in voltage can be obtained as follows. For the single-transducer structure of Fig. 8 (a), the equation of motion with zero AC voltage becomes using (23 a)

$$m\ddot{x} + \gamma\dot{x} + kx = F_1 \Rightarrow m\ddot{\xi} + \gamma\dot{\xi} = -\frac{1}{2}\frac{k_e}{(1+\xi)^2} - k\xi. \tag{1}$$

Solving for the rest position ($\dot{\xi} = 0$ and $\ddot{\xi} = 0$), one obtains

$$k_e = -2k\xi(1+\xi)^2 \equiv g(\xi). \tag{2}$$

The function $g(\xi)$ is plotted in Fig. 1. One sees that if $k_e > 8k/27$, there is no solution for the resonator displacement inside the transducer gap resulting in pull-in. The corresponding voltage (pull-in voltage) is given by (12 a). Similarly, for the double-transducer circuit of Fig. 8 (c), one obtains the instability at a higher bias voltage of (12 b).

APPENDIX 2

Derivation of the Equivalent Circuits

Derivation of the Equivalent Circuits

To derive the small-signal electrical-equivalent circuit of Fig. 8 (c), we assume a harmonic excitation $u = u_0 e^{j\omega t}$ that yields $\dot{u} = j\omega u$. For the load voltage $u_L = i_2 Z_L$ and for the voltage across the source resistance $u_s = i_1 R_{\mathrm{ac}}$, we also use $\dot{u}_L = j\omega u_L$ and $\dot{u}_s = j\omega u_s$, respectively. Equations (23 a), (23 b), (24 a) and (24 b) for the forces and currents are now approximated to first order in the small parameters $\xi \equiv x/d$, $\bar{u} \equiv u/V$ and $\bar{u}_L \equiv u_L/V$ resulting in

$$i_1 = \big(j\omega C_0 u - \eta\dot{x}\big)/\big(1 + j\omega C_0 R_{\mathrm{ac}}\big) = u/Z \tag{1 a}$$
$$i_2 = \eta\dot{x}/\big(1 + j\omega C_0 Z_L\big) \tag{1 b}$$
$$F_1 = -\eta\big(V/2 + u'\big) + k_e x - \gamma_s \dot{x} \tag{1 c}$$
$$F_2 = \eta V/2 + k_e x - \gamma_L \dot{x}, \tag{1 d}$$

where Z is the unknown input impedance, $\gamma_s \equiv \eta^2(Z_0||R_{\mathrm{ac}})$ and $\gamma_L \equiv \eta^2(Z_0||Z_L)$ are the complex dissipation coefficients introduced by the source and load impedances and $u' = u/(1 + j\omega C_0 R_{\mathrm{ac}})$ is the Thévenin-equivalent AC voltage. The equation of motion for the resonator ($m\ddot{x} + \gamma\dot{x} + kx = F_1 + F_2$) can now be written as

$$m\ddot{x} + \hat{\gamma}\dot{x} + \bar{k}x = -\eta u', \tag{2}$$

where $\hat{\gamma} \equiv \gamma + \gamma_s + \gamma_L$ and $\bar{k} \equiv k - 2k_e$. Solving now, as usual, for the resonator motion by assuming $x = Ae^{j\omega t}$, where A is an unknown complex amplitude, one obtains the resonator velocity as

$$\dot{x} = \frac{-j\omega\eta u'}{\bar{k} - m\omega^2 + j\omega\hat{\gamma}}. \tag{3}$$

Inserting (3) into (1 a) one finds the input impedance Z as shown in Fig. 8 (d)

$$Z = R_{\mathrm{ac}} + Z_0||\big(Z_{\mathrm{em}} - (Z_0||R_{\mathrm{ac}})\big), \tag{4}$$

where

$$\begin{aligned} Z_{\mathrm{em}} = \frac{\bar{k} - m\omega^2 + j\omega\hat{\gamma}}{j\omega\eta^2} &= \frac{\gamma}{\eta^2} + j\omega\frac{m}{\eta^2} + \frac{1}{j\omega\dfrac{\eta^2}{\bar{k}}} + (Z_0||R_{\mathrm{ac}}) + (Z_0||Z_L) \\ &= R_m + j\omega L_m + \frac{1}{j\omega C_{m,2}} + (Z_0||R_{\mathrm{ac}}) + (Z_0||Z_L). \end{aligned} \tag{5}$$

Here R_m, L_m and $C_{m,2}$ are given by (22 a), (22 b) and (22 c), respectively. Similarly, one can derive the equivalent circuit of Fig. 8 (b).

APPENDIX 3

Publications I–VI

PUBLICATION I

Intermodulation in Capacitively Coupled Microelectromechanical Filters

In: IEEE Electron Device Letters 2005.
Vol. 26, No. 5, pp. 289–291.
Reprinted with permission from the publisher.

Intermodulation in Capacitively Coupled Microelectromechanical Filters

Ari T. Alastalo and Ville Kaajakari, *Member, IEEE*

***Abstract*—A compact model for third-order intermodulation in capacitively coupled microelectromechanical filters is derived. A simple expression for the input third-order intercept point is given. This is valuable in designing micromechanical filters, for example, for communication applications. The validity of the analytic model is verified with numerical harmonic-balance simulations and experimental measurements.**

***Index Terms*—Communication systems, filter distortion, filters, intermodulation distortion, microelectromechanical devices.**

I. Introduction

WIRELESS communication devices rely on high-quality-factor ceramic, SAW, or FBAR filters for RF and IF filtering. While these macroscopic filters offer excellent performance, the cost and size make them unattractive for portable devices. Consequently, receiver architectures such as direct conversion have been developed in order to reduce the need for off-chip components [1]. However, it is unlikely that the high-Q filters can completely be eliminated.

Micromechanical resonators are a potential replacement for off-chip filters due to their compact size and integrability with IC electronics [2]. The demonstrated quality factors of microresonators, $Q > 100\,000$ at 10 MHz [3] and $Q > 1\,000$ at 1 GHz [4], are comparable to their macroscopic counterparts. Unfortunately, as the resonator size is reduced, its power handling capacity and linearity are also lowered [5]. In filter applications, signal intermodulation (IM) due to odd-order nonlinearities is especially detrimental as it can result in unwanted frequency components within the filter passband. For example, cubic mixing of two fundamental signals having frequencies ω_1 and ω_2 results in third-order intermodulation (IM3) products at frequencies $2\omega_1 - \omega_2$ and $2\omega_2 - \omega_1$. Consequently, a useful measure of filter linearity is the third-order intercept point (IP3) defined as the crossing point of the linear extrapolations of the small-signal fundamental current (or voltage or power) and the IM3 current (or voltage or power) in the filter output. The signal level at the filter input, corresponding to IP3, is termed IIP3.

In this letter, the first published closed-form expression for in-band IIP3 is given for capacitively coupled microresonators, and the result is verified with simulations and experiments. The analysis differs from prior modeling where off-resonance forces were considered [6]. Here, the filter passband output currents are considered directly and all nonlinear terms are included to third-order. The results in this letter provide a practical starting point in evaluating and designing the microresonators for commercial filter applications.

Manuscript received January 4, 2005; revised February 22, 2005. This work was supported by the Academy of Finland under Grant 20542 and by Aplac Solutions. The review of this letter was arranged by Editor J. Sin.

The authors are with Microsensing, VTT Information Technology, VTT Technical Research Center of Finland, FIN-02044 VTT Espoo, Finland (e-mail: ari.alastalo@vtt.fi, ville.kaajakari@vtt.fi).

Digital Object Identifier 10.1109/LED.2005.846589

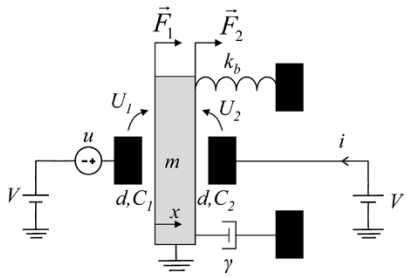

Fig. 1. Harmonic resonator (k_b, m, and γ) coupled capacitively for filtering of an electronic signal u. Signal u near the resonance excites mechanical motion that is sensed as current i.

II. Analysis

Fig. 1 shows a simplified model for a capacitively coupled mechanical resonator used as a filter. Here V is the bias voltage, u is the small-signal input voltage, and i is the current at the filter output. The zero-voltage gap of the input and output transducers is denoted by d and x is the displacement of the resonating mass m. The spring constant and the damping coefficient of the resonator are k_b and γ, respectively. The resonator quality factor is given by $Q = \sqrt{k_b m}/\gamma$. The capacitance values of the input and output transducers are $C_1 = \epsilon_0 A/(d+x)$ and $C_2 = \epsilon_0 A/(d-x)$, where A is the area of the transducer electrodes. The voltages across the transducers are $U_1 = V + u$ and $U_2 = V$, and the forces exerted by the transducers to the resonating mass are $F_i = (1/2)U_i^2 \partial C_i/\partial x$, $i \in \{1,2\}$.

For small gaps, capacitive nonlinearities dominate and mechanical spring nonlinearities do not contribute to IIP3 [5]. Thus, the equation of motion for the resonator in Fig. 1, taking capacitive nonlinearities into account up to third order in small parameters $\bar{u} \equiv u/V$ and $\xi \equiv x/d$, is

$$m\ddot{\xi} + \gamma\dot{\xi} + \bar{k}\xi = -k_e\bar{u} + k_e\left[2\bar{u}\xi - \frac{\bar{u}^2}{2} + 4\xi^3 - 3\bar{u}\xi^2 + \bar{u}^2\xi\right]. \tag{1}$$

where $k_e \equiv \eta V/d$, with $\eta \equiv C_0 V/d$ and $C_0 \equiv \epsilon_0 A/d$, is the electromechanical spring constant and $\bar{k} \equiv k_b - 2k_e$. The time derivative is denoted with a dot. The output current $i = d(C_2 U_2)/dt$ can be expanded as

$$\bar{i} \equiv \frac{i}{d} = \eta\left(1 + 2\xi + 3\xi^2 + 4\xi^3 + \cdots\right)\dot{\xi}. \tag{2}$$

0741-3106/$20.00 © 2005 IEEE

We use a high-Q approximation such that motion ξ has no frequency components outside the resonator passband. Thus, for signals near the resonance, only the linear force term and the three third-order force terms in (1) contribute to the motion. Similarly, only the first and third terms in (2) contribute to the in-band current.

A two-tone IM3 test is made with a signal $\bar{u}(t) = \bar{u}_0(\cos\omega_1 t + \cos\omega_2 t)$ where ω_1 and ω_2 are inside the filter passband. The resulting linear solution to (1), $\xi_{\rm lin} = -q\bar{u}_0\,(\sin\omega_1 t + \sin\omega_2 t)$, and (2) give the linear fundamental current

$$\bar{i}_{\rm fund} = \eta\dot{\xi}_{\rm lin} = -\eta q\bar{u}_0(\omega_1\cos\omega_1 t + \omega_2\cos\omega_2 t) \qquad (3)$$

where $q \equiv k_e Q/\bar{k}$. The main nonlinear contributions to the current (2) at $\omega_3 = 2\omega_1 - \omega_2$ come from the terms $\bar{i}_{\rm NL1} \equiv 3\eta\xi_{\rm lin}^2\dot{\xi}_{\rm lin}$ and $\bar{i}_{\rm NL2} \equiv \eta\dot{\xi}_{\rm NL}$, where $\xi_{\rm NL}$ is the in-band motion due to nonlinear forces in (1). A lowest order estimate for $\xi_{\rm NL}$ is found by inserting the linear solution $\xi_{\rm lin}$ to the third-order force terms into (1) and using the linear response to find the corresponding motion at ω_3. One finds

$$\bar{i}_{\rm NL1} = -\frac{3}{4}\eta\omega_3\bar{u}_0^3 q^3\cos\omega_3 t \qquad (4a)$$

$$\bar{i}_{\rm NL2} = -\eta\omega_3\bar{u}_0^3 q\left[\frac{3}{4}q^2\cos\omega_3 t + \left(3q^3 + \frac{q}{4}\right)\sin\omega_3 t\right]. \qquad (4b)$$

Equating the amplitude of $\bar{i}_{\rm NL} = \bar{i}_{\rm NL1} + \bar{i}_{\rm NL2}$ with the amplitude of the fundamental current (3) at ω_1 and solving for the IIP3 voltage, we obtain

$$\bar{u}_{0,\rm IIP3}^2 = \frac{\omega_1}{\omega_3\sqrt{\left(3q^3 + \frac{q}{4}\right)^2 + \frac{9q^4}{4}}} \qquad (5)$$

where, as defined above, $q = k_e Q/\bar{k} = QC_0V^2/(k_b d^2 - 2C_0V^2)$. As ω_1 and ω_3 are almost equal, they can be canceled out. For high Q, $q > 1$ in (5) and the strongest nonlinear contribution is due to the ξ^3 term in (1). Thus, a simple estimate for the IIP3 voltage is obtained as

$$u_{0,\rm IIP3} = V\bar{u}_{0,\rm IIP3} \approx \frac{V}{\sqrt{3q^3}} \approx V\left(\frac{U_{\rm pi}}{V}\right)^3\sqrt{\frac{8}{3Q^3}} \qquad (6)$$

where $U_{\rm pi} = \sqrt{k_b d^2/(2C_0)}$ is the electromechanical pull-in voltage at which bias level the spring constant $\bar{k}$ vanishes and the resonator becomes unstable.

III. Single-Beam MEMS Resonator Example

To validate the analytical results, an experimental test with a clamped–clamped beam resonator was performed. The schematic of the resonator, fabricated on a silicon-on-insulator (SOI) wafer [3], is shown in Fig. 2(a) together with an illustration of the measurement setup. Harmonic signals at ω_1 and ω_2 within the filter bandwidth are generated with two Agilent 33120A signal sources. The filter output signal is amplified with a JFET preamplifier. The filter circuitry and the preamplifier are kept at a low pressure of 8×10^{-3} mbar. The output spectrum is measured with an HP 4195A network/spectrum analyzer. To model the resonator, the S_{21} measurement was performed for

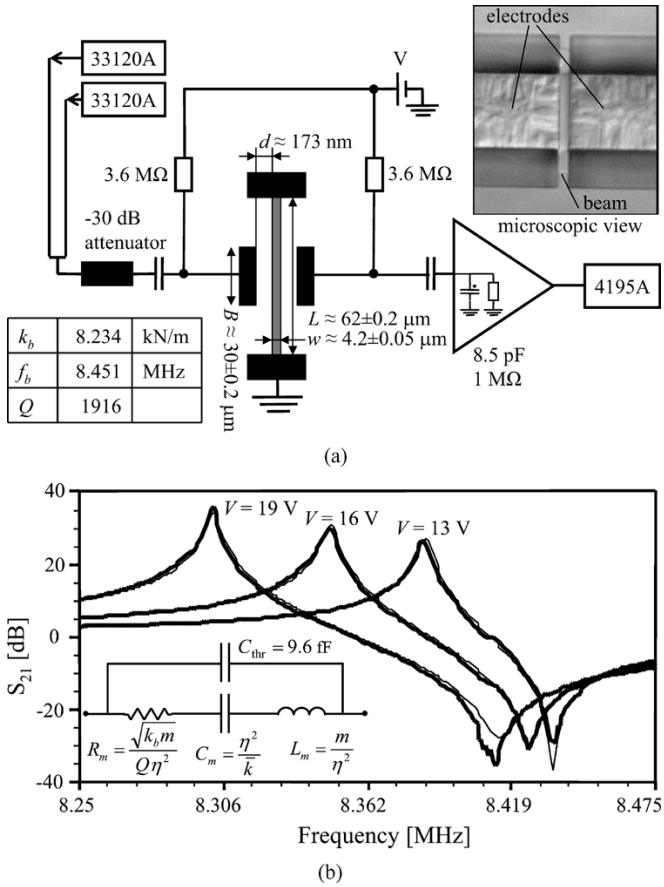

Fig. 2. Experimental setup for IIP3 measurement. (a) Measurement setup for the capacitively coupled beam resonator. The device thickness is 10 μm, and it vibrates horizontally in the plane of the wafer. Also shown are the relevant resonator parameters. Values for L, w, and B are estimated from the microscopic view while the gap size $d = 173$ nm and effective length $L_{\rm eff} = 66\ \mu$m ($> L$ due to imperfect clamping) are based on the numerical fit of Fig. 2(b). (b) Measured (thick line) and simulated (thin line) zero-bias-calibrated response of the beam resonator for different bias voltages. The electrical equivalent circuit is also shown ($R_m = 55$ kΩ, $C_m = 179.7$ aF, and $L_m = 2.022$ H at $V = 16$ V).

three different bias voltages well below the pull-in voltage, as shown in Fig. 2(b). Fitting an electromechanical model to the measured response allows one to find a good estimate of the filter parameters. Fitting was done by adjusting the effective beam length $L_{\rm eff}$, the Q value, the feed-through capacitance $C_{\rm thr}$, and the gap d. The obtained Q value is rather low due to the low aspect ratio L/w of the beam, resulting in energy leakage to supporting structures [7], [8]. The spring constant k_b is calculated from

$$k_b = \frac{16EH\left(\frac{w}{L}\right)^3}{\frac{1}{2}\left(\frac{B}{L}\right)^3 - \left(\frac{B}{L}\right)^2 + 1} \qquad (7)$$

which assumes the load to be uniformly distributed across the transducer area [9]. The eigenfrequency of the resonator is given by $f_b = 1.028\,w/L^2\sqrt{E/\rho}$ [10].

With the estimated parameter values, (6) gives 34.3 dBmV for IIP3 at $V = 16$ V (corresponding to -15.7 dBm with a 50-Ω source). This is compared to the measured behavior as well as to a two-tone harmonic-balance simulation [11] in Fig. 3. It is seen that all three approaches agree very well.

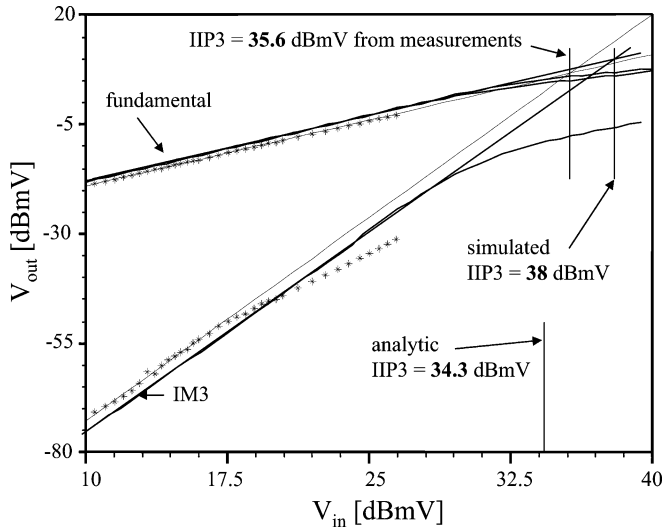

Fig. 3. Measured (asterisks) and simulated (solid curves) fundamental and IM3 voltage at the resonator output at $V = 16$ V and $\omega_2 - \omega_1 = 2\pi \times 200$ Hz (ω_1 and ω_2 are inside the filter passband). The lines extrapolate the linear behavior, found at small input voltages, to determine the IIP3.

IV. Discussion

In this letter, a concise formulation for IIP3 in capacitively coupled micromechanical filters is given. The experimental verification is given for a flexural clamped–clamped beam, but the formulation applies to all MEMS filters: 1) that are coupled with parallel-plate transducers and 2) for which the capacitive nonlinearities are the dominant intermodulation mechanism. Typically, for small gaps ($d < 200$ nm), the mechanical nonlinearities do not need to be taken into account [5].

As an example of usage of (6), the published values of $Q = 1600$, $d = 74$ nm $V = 12.9$ V, $k = 73.5$ MN/m, and $C_0 = 7.5$ fF for a demonstrated 1.1-GHz radial-mode disk resonator [4] give $u_{0,\mathrm{IIP3}} = 21$ kV while $R_m = 3.9\,\mathrm{M}\Omega$. It is thus seen that the motional impedance, rather than IM, is a challenge in using this resonator. The motional impedance can be lowered by increasing the bias voltage and reducing the electrode gap. However, while $R_m \propto d^4$, the IIP3 voltage is reduced even faster as $u_{0,\mathrm{IIP3}} \propto d^{9/2}$. For example, $d = 5$ nm and $V = 15$ V for the same resonator give $C_0 = 111$ fF, $u_{0,\mathrm{IIP3}} = 85$ mV, and $R_m = 60\,\Omega$. If this resonator were used as a bandpass filter, signal corruption due to IM can be expressed by a resulting signal-to-interference ratio $\mathrm{SIR} = u_{\mathrm{sig,in}}\, u_{0,\mathrm{IIP3}}^2 / u_{\mathrm{int,in}}^3$, where $u_{\mathrm{sig,in}}$ and $u_{\mathrm{int,in}}$ are the input signal and interference, respectively [12]. Using a GSM phone as an example, the specifications require operation with $u_{\mathrm{sig,in}} = -99$ dBm and $u_{\mathrm{int,in}} = -43$ dBm for the closest interferer [13]. With a 50-Ω antenna source, we find $\mathrm{SIR} = 7.3$ dB. This can be compared to the required receiver SIR of 9 dB [13]. Thus, it is concluded that IM specifications can set a lower limit for the gap in parallel-plate transducer coupled resonators.

Acknowledgment

The authors would like to thank J. Kiihamäki for device fabrication.

References

[1] T. Lee, *The Design of CMOS Radio-Frequency Integrated Circuits*, 2nd ed. Cambridge, U.K.: Cambridge Univ. Press, 2004.

[2] C. T.-C. Nguyen, "Frequency-selective MEMS for miniaturized low-power communication devices," *IEEE Trans. Microw. Theory Tech.*, vol. 47, no. 8, pp. 1486–1503, Aug. 1999.

[3] V. Kaajakari, T. Mattila, A. Oja, J. Kiihamäki, and H. Seppä, "Square-extensional mode single-crystal silicon micromechanical resonator for low phase noise oscillator applications," *IEEE Electron Device Lett.*, vol. 25, no. 4, pp. 173–175, Apr. 2004.

[4] J. Wang, Z. Ren, and C. T.-C. Nguyen, "Self-aligned 1.14-GHz vibrating radial-mode disk resonators," in *Proc. Transducers'03*, Jun. 2003, pp. 947–950.

[5] V. Kaajakari, T. Mattila, A. Oja, and H. Seppä, "Nonlinear limits for single-crystal silicon microresonators," *J. Microelectromech. Syst.*, vol. 13, no. 5, pp. 715–724, Oct. 2004.

[6] R. Navid, J. R. Clark, M. Demirci, and C. T.-C. Nguyen, "Third-order intermodulation distortion in capacitively-driven cc-beam micromechanical resonators," in *Proc. Int. IEEE Micro Electro Mechanical Systems Conf.*, Interlaken, Switzerland, Jan. 2001, pp. 228–231.

[7] T. Mattila, O. Jaakkola, J. Kiihamäki, J. Karttunen, T. Lamminmäki, P. Rantakari, A. Oja, H. Seppä, H. Kattelus, and I. Tittonen, "14 MHz micromechanical oscillator," *Sens. Actuators A, Phys.*, vol. 97–98, pp. 497–502, Apr. 2002.

[8] K. Y. Yasumura, T. D. Stowe, E. M. Chow, T. Pfafman, T. W. Kenny, B. C. Stipe, and D. Rugar, "Quality factors in micron- and submicron-thick cantilevers," *J. Microelectromech. Syst.*, vol. 9, no. 1, pp. 117–125, Mar. 2000.

[9] Q. Meng, M. Mehregany, and R. L. Mullen, "Theoretical modeling of microfabricated beams with elastically restrained supports," *J. Microelectromech. Syst.*, vol. 2, no. 3, pp. 128–137, Sep. 1993.

[10] W. Weaver Jr., S. P. Timoshenko, and D. H. Young, *Vibration Problems in Engineering*, 5th ed. New York: Wiley, 1990.

[11] T. Veijola and T. Mattila, "Modeling of nonlinear micromechanical resonators and their simulation with the harmonic-balance method," *Int. J. RF Microw. Computer-Aided Eng.*, vol. 11, no. 5, pp. 310–321, Sep. 2001.

[12] B. Razavi, *RF Microelectronics*. Upper Saddle River, NJ: Prentice-Hall, 1998.

[13] ETSI, *GSM Global System for Mobile Communications*, 3GPP TS 05.01/05.05, 2003.

PUBLICATION II

Third-Order Intermodulation in Microelectromechanical Filters Coupled With Capacitive Transducers

In: IEEE Journal of Microelectromechanical Systems 2006. Vol. 15, No. 1, pp. 141–148.
Reprinted with permission from the publisher.

Third-Order Intermodulation in Microelectromechanical Filters Coupled With Capacitive Transducers

Ari T. Alastalo and Ville Kaajakari

***Abstract*—Third-order intermodulation in capacitively coupled microelectromechanical filters is analyzed. Parallel-plate transducers are assumed and, in addition to the capacitive nonlinearities, also the usually much weaker second- and third-order mechanical resonator nonlinearities are taken into account. Closed-form expressions for the output signal-to-interference ratio (SIR) and input intercept point are derived. The analytical results are verified in experiments and in numerical harmonic-balance simulations. It is shown that intermodulation as a function of frequency is asymmetric with respect to the passband. The results are valuable in designing micromechanical filters, for example, for communication applications. [1544]**

***Index Terms*—Communication systems, intermodulation distortion, microelectromechanical devices.**

I. Introduction

HIGH-QUALITY factor resonators are ubiquitous in todays communication devices. Macroscopic ceramic, SAW or FBAR filters offer excellent performance but their large size, high cost and unsuitability for IC integration limit their scope of application. In order to reduce the number of these bulky off-chip filters, receiver architectures such as direct conversion have been developed [1]. However, high-Q filters remain needed as band-select or channel-select filters to suppress interfering signals.

Miniature mechanical resonators, fabricated with microelectromechanical-systems (MEMS) technology, are a potential replacement of off-chip filters as they are compact in size and integratable with IC electronics [2]. The demonstrated quality factors of MEMS resonators, $Q > 100000$ at 10 MHz [3] and $Q > 1000$ at 1 GHz [4], are comparable to their macroscopic counterparts. While the mechanical properties of microresonators are very promising, obtaining a low electrical impedance ($\approx 50\,\Omega$) is challenging, especially for the minituarized high frequency resonators that are mechanically stiff. To obtain low impedance levels, strong electromechanical transduction is needed which in case of electrostatic coupling requires a large bias voltage and/or a narrow electrode gap. As large bias voltages are not preferred, narrow electrode gaps ($< 200\,\mathrm{nm}$) are often used, which introduces nonlinear electrostatic transducer forces and higher harmonics due to the inverse relationship between the electrode capacitance and the gap spacing. Additionally, mechanical nonlinear effects are possible in microresonators and fundamentally material nonlinearities set the limit for minituarization [5].

In filter applications, signal intermodulation (IM) due to odd-order nonlinearities is especially detrimental as it can lead to unwanted frequency components within the filter passband. For example, cubic mixing of two fundamental signals having frequencies ω_1 and ω_2 results in third-order intermodulation (IM3) products at frequencies $2\omega_1-\omega_2$ and $2\omega_2-\omega_1$. If $\omega_1 = \omega_0+\Delta\omega$ and $\omega_2 = \omega_0 + 2\Delta\omega$, the IM product at $2\omega_1 - \omega_2$ is at the passband center frequency ω_0 corrupting the desired signal.

While complete linear models for the capacitively coupled resonators/filters have been developed [6], [7], intermodulation has received less attention. Navid *et al.* measured IM3 for a 10 MHz electrostatically coupled beam resonator [8]. They found that due to intermodulation distortion, there is a tradeoff between linearity and motional resistance. Their measured and calculated intermodulation results for interferers far below the passband were in agreement. However, since in [8] the analysis is based on transducer forces, not all mechanisms contributing to the intermodulation for varying interferer frequencies are taken into account. Our analysis is valid at both sides of the passband as well as for interferers within and close to the passband edge, where our results differ from those of [8]. Nolan *et al.* considered receivers with a linear MEMS filter preceding a nonlinear low-noise amplifier (LNA) [9]. They found that increasing the quality factor of the filter enhances the resulting signal-to-interference ratio (SIR). However, as we will show, this conclusion does not hold when the limiting intermodulation is due to nonlinearities of the MEMS filter.

In this paper, our prior analysis of in-band filter distortion [10] is extended to out-of-band interferers. Additionally, mechanical nonlinearities are included in the analysis. All intermodulation effects are taken into account to the first significant order and a closed form expression is derived for the signal-to-interference ratio (SIR). The analytical work is compared to numerical large-signal harmonic-balance simulations as well as to experiments and a good agreement is obtained. Due to the high motional impedance of micromechanical filters, classical filter matching to 50 Ω seems challenging and the microfilters may

Manuscript received March 10, 2005; revised August 15, 2005. This work is supported by the Academy of Finland (grant 20542), Aplac® Solutions, VTI Technologies, Okmetic, and Tekes (National Technology Agency of Finland). Subject Editor K. Najafi.

The authors are with the VTT Technical Research Center of Finland, VTT Information Technology, Microsensing, Espoo, FIN-02044 VTT, Finland (e-mail: ari.alastalo@vtt.fi, ville.kaajakari@vtt.fi).

Digital Object Identifier 10.1109/JMEMS.2005.863705

1057-7157/$20.00 © 2006 IEEE

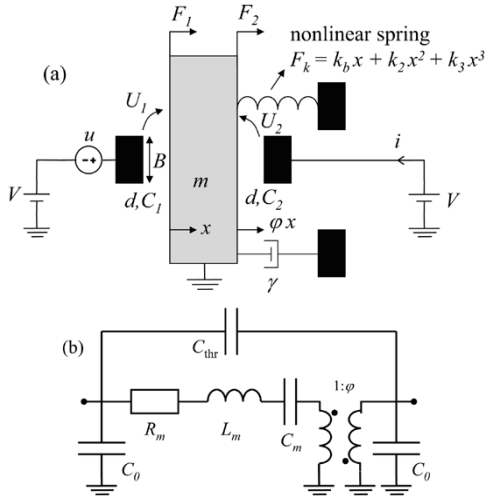

Fig. 1. (a) Capacitively coupled nonlinear resonator $\{k_b, k_2, k_3, m, \gamma\}$ filtering an electronic signal u. (b) Small-signal electrical equivalent model for the linear resonator with identical input and output transducers.

TABLE I
DEFINITIONS USED IN THE PAPER

C_0	$\epsilon_0 A/d$	ω_b	$\sqrt{k_b/m}$	$\bar{i}$	i/d
η	$C_0 V/d$	ω_0	$\sqrt{\bar{k}/m}$	α	$(\varphi-1)/2$
k_e	$\eta V/d$	ω_e	$\sqrt{k_e/m}$	Γ	$\bar{u}_{\text{int},0}/\bar{u}_{\text{sig},0}$
$\bar{k}$	$k_b - 2k_e$	ω_1	$\omega_0 + \Delta\omega$	R_m	γ/η^2
$\bar{k}_2$	dk_2/k_e	ω_2	$\omega_0 + 2\Delta\omega$	C_m	$\eta^2/\bar{k}$
$\bar{k}_3$	$d^2 k_3/k_e$	$\bar{u}$	u/V (small)	L_m	m/η^2
Q	$\sqrt{\bar{k}m}/\gamma$	ξ	x/d (small)	q	$k_e Q/\bar{k}$

be best suited for on-chip channel select filtering where interfacing to 50 Ω may not be required [2]. The analysis in this paper is therefore formulated in terms of filter input voltages and output currents to facilitate analysis with any source and load impedance with minimal effort.

The paper is organized as follows. First, in Section II, an analytical model for the intermodulation is developed. This is followed by Section III, where the analytical results are compared to measured and simulated intermodulation of two different microresonators. In Section IV, the present results are discussed and compared to other published results and the utility of the paper is demonstrated by calculating the IM for micromechanical filters at 1 GHz. Section V concludes the paper.

II. ANALYSIS

Fig. 1 shows a simplified model for a capacitively coupled mechanical resonator used as a filter and Table I collects the shorthand notations used in this paper. Here V is the bias voltage, u is a small-signal input voltage and i is the output current. The zero-voltage gap of the input and output transducers is denoted d and x is the displacement of the resonating mass m. The linear and nonlinear mechanical spring constants of the resonator are k_b, k_2 and k_3 and γ is the damping coefficient. For generality, the displacement at the output transducer is related to the resonator displacement x by φx, where (1) is shown at the bottom of the page. In Section III, we will show measurement results for the both cases of (1). The capacitance values of the input and output transducers are

$$C_1 = \frac{\epsilon_0 A}{d + x} \tag{2a}$$

$$C_2 = \frac{\epsilon_0 A}{d - \varphi x} \tag{2b}$$

where A is the area of the transducer electrodes. The voltages across the transducers are $U_1 = V + u$ and $U_2 = V$ and the forces exerted by the transducers to the resonating mass are

$$F_i = \frac{1}{2} U_i^2 \frac{\partial C_i}{\partial x}, \quad i \in \{1, 2\}. \tag{3}$$

The positive direction of the force is as shown in Fig. 1.

The equation of motion for the resonator in Fig. 1 is

$$m\ddot{x} + \gamma\dot{x} + k_b x + k_2 x^2 + k_3 x^3 = F_1 + F_2 \tag{4}$$

where F_1 and F_2 are found from (3) after expanding the capacitances of (2a) and (2b) in power series as

$$C_1 = C_0 \left[1 - \left(\frac{x}{d}\right) + \left(\frac{x}{d}\right)^2 - \left(\frac{x}{d}\right)^3 + \cdots\right] \tag{5a}$$

$$C_2 = C_0 \left[1 + \varphi\left(\frac{x}{d}\right) + \left(\frac{x}{d}\right)^2 + \varphi\left(\frac{x}{d}\right)^3 + \cdots\right] \tag{5b}$$

where $C_0 \equiv \epsilon_0 A/d$. Taking nonlinearities into account up to third order in small parameters $\bar{u} \equiv u/V$ and $\xi \equiv x/d$, one finds for the equation of motion

$$\ddot{\xi} + \frac{\omega_0}{Q}\dot{\xi} + \omega_0^2 \xi = \omega_e^2 \left[\overset{(a)}{\alpha} - \overset{(b)}{\bar{u}} + \left(3\alpha - \overset{(c)}{\bar{k}_2}\right)\xi^2 + 2\overset{(d)}{\bar{u}}\xi - \frac{\overset{(e)}{\bar{u}^2}}{2} + \left(4 - \overset{(f)}{\bar{k}_3}\right)\xi^3 - 3\overset{(g)}{\bar{u}}\xi^2 + \overset{(h)}{\bar{u}^2}\xi\right] \equiv F. \tag{6}$$

For definitions of the variables in (6), see Table I. The time derivative is denoted with a dot. The fundamental frequency of the resonator is ω_0. The dc force term (a) is nonzero for $\varphi = -1$ (1) which is the case for example for a BAW resonator in the square-extensional mode [3] or for a flexural-beam resonator if the input and output transducers are at the same side of the beam. For $\varphi = 1$ in (1), the dc force vanishes $(\alpha = 0)$. For intermodulation performance, the dc term has no effect and will not be considered in what follows.

$$\varphi = \begin{cases} 1, & \text{e.g., for transducers at different sides of a flexural beam.} \\ -1, & \text{e.g., for transducers at the same side of a flexural beam or for a BAW resonator.} \end{cases} \tag{1}$$

For a force term $F(\omega)$ in the right-hand side of (6), the response function

$$H(\omega) = H'(\omega) + jH''(\omega) \equiv \left(\omega_0^2 - \omega^2 + j\frac{\omega\omega_0}{Q}\right)^{-1} \quad (7)$$

with real and imaginary parts

$$H'(\omega) = \frac{\omega_0^2 - \omega^2}{\left(\omega_0^2 - \omega^2\right)^2 + \left(\frac{\omega\omega_0}{Q}\right)^2}$$
$$H''(\omega) = \frac{\frac{-\omega\omega_0}{Q}}{\left(\omega_0^2 - \omega^2\right)^2 + \left(\frac{\omega\omega_0}{Q}\right)^2} \quad (8)$$

gives the linear solution as

$$\xi_{\text{lin}}(\omega) = FH' + \frac{\dot{F}H''}{\omega} \quad (9)$$

where the second term is due to dissipations. Note the short notation for the real and imaginary parts, H' and H'', respectively. For the resonance frequency we have

$$H'(\omega_0) = 0$$
$$H''(\omega_0) = -\frac{Q}{\omega_0^2} \equiv H_0''. \quad (10)$$

The output current

$$i = \frac{\partial(C_2U_2)}{\partial t} = V\frac{\partial C_2}{\partial x}\dot{x} \quad (11)$$

can be expanded with (5b) as

$$\bar{i} \equiv \frac{i}{d} = \eta\left(\underset{\bar{i}_{\text{sig}},\bar{i}_{\text{IM3}}^{(1)}}{\underset{\downarrow}{\varphi}} \quad +2\xi + 3\varphi\xi^2 + \underset{\bar{i}_{\text{IM3}}^{(2)}}{\underset{\downarrow}{4}}\xi^3 + \cdots\right)\dot{\xi}. \quad (12)$$

Here we have indicated the terms that contribute to the signal and intermodulation currents at the fundamental frequency ω_0. Since φ scales all the considered current terms and therefore does not affect SIR, φ is set to unity in the following analysis for simplicity.

Analytical expressions will now be derived for the signal current $\bar{i}_{\text{sig}}$ as well as for the two IM3 terms $\bar{i}_{\text{IM3}}^{(1)}$ and $\bar{i}_{\text{IM3}}^{(2)}$ in (12) and the resulting SIR will be discussed. The desired signal $\bar{u}_{\text{sig}}$ at the resonance frequency ω_0 and an interfering signal $\bar{u}_{\text{int}}$ at the filter input are

$$\bar{u}_{\text{sig}} = \bar{u}_{\text{sig},0}\cos\omega_0 t \quad (13a)$$
$$\bar{u}_{\text{int}} = \bar{u}_{\text{int},0}\left(\cos\omega_1 t + \cos\omega_2 t\right) \quad (13b)$$

where

$$\omega_1 \equiv \omega_0 + \Delta\omega$$
$$\omega_2 \equiv \omega_0 + 2\Delta\omega. \quad (14)$$

The linear motion due to the excitations (13a) and (13b) is easily found with (6) (b), and (9)

$$\xi_{\text{sig}} = H_0''\omega_e^2\bar{u}_{\text{sig},0}\sin\omega_0 t \quad (15a)$$
$$\xi_{\text{int}} = -\omega_e^2\bar{u}_{\text{int},0}\Big(H_1'\cos\omega_1 t - H_1''\sin\omega_1 t + H_2'\cos\omega_2 t - H_2''\sin\omega_2 t\Big). \quad (15b)$$

Here $H_i \equiv H(\omega_i)$. The signal output current is with (12)

$$\bar{i}_{\text{sig}} = \eta\dot{\xi}_{\text{sig}} = \eta H_0''\omega_e^2\omega_0\bar{u}_{\text{sig},0}\cos\omega_0 t \equiv \bar{i}_{\text{sig}}^{\text{I}}\cos\omega_0 t. \quad (16)$$

The signal current is in phase with the signal input voltage (13a) and its amplitude is denoted $\bar{i}_{\text{sig}}^{\text{I}}$.

To obtain a first-order estimate for the intermodulation current $\bar{i}_{\text{IM3}}$ at ω_0 due to the interference motion at ω_1 and ω_2 (15b) requires some work. We assume that $\Delta\omega \ll \omega_0$ and that the Q value of the resonator is high enough to forbid motion at the harmonics of the excitation frequencies. Thus, the second-order terms (c,d,e) in (6) can be ignored. When the interference motion $\xi = \xi_{\text{int}}$ of (15b) and signal of (13b) are substituted to the third-order terms (f,g,h) in (6), a force $F_{\text{IM3}}(\omega_0)$ at $\omega_0 = 2\omega_1 - \omega_2$ is generated according to the formulas expressing trigonometric exponents and products, such as $\cos^2(\omega_1 t)\cos(\omega_2 t)$, in terms of first order functions, such as $\cos((2\omega_1 - \omega_2)t)$. The corresponding motion ξ_{IM3} at ω_0, given by (9), results in an intermodulation current contribution $\bar{i}_{\text{IM3}}^{(1)}$ in (12)

$$\bar{i}_{\text{IM3}}^{(1)} = \eta\dot{\xi}_{\text{IM3}} \equiv \bar{i}_{\text{IM3}}^{\text{I1}}\cos\omega_0 t + \bar{i}_{\text{IM3}}^{\text{Q1}}\sin\omega_0 t, \quad (17)$$

where the subscripts I and Q refer to in-phase and quadrature components, respectively. The second contribution $\bar{i}_{\text{IM3}}^{(2)}$ to the intermodulation current is obtained by substituting $\xi = \xi_{\text{int}}$ of (15b) to the $3\eta\xi^2\dot{\xi}$ term in the current expansion (12) and is given by

$$\bar{i}_{\text{IM3}}^{(2)} = 3\eta\xi_{\text{int}}^2\dot{\xi}_{\text{int}} \equiv \bar{i}_{\text{IM3}}^{\text{I2}}\cos\omega_0 t + \bar{i}_{\text{IM3}}^{\text{Q2}}\sin\omega_0 t. \quad (18)$$

The total intermodulation current is a sum of the two contributions (17) and(18)

$$\bar{i}_{\text{IM3}} = \bar{i}_{\text{IM3}}^{(1)} + \bar{i}_{\text{IM3}}^{(2)} \equiv \bar{i}_{\text{IM3}}^{\text{I}}\cos\omega_0 t + \bar{i}_{\text{IM3}}^{\text{Q}}\sin\omega_0 t \quad (19)$$

where

$$\bar{i}_{\text{IM3}}^{\text{I}} = \bar{i}_{\text{IM3}}^{\text{I1}} + \bar{i}_{\text{IM3}}^{\text{I2}} \quad (20a)$$
$$\bar{i}_{\text{IM3}}^{\text{Q}} = \bar{i}_{\text{IM3}}^{\text{Q1}} + \bar{i}_{\text{IM3}}^{\text{Q2}}. \quad (20b)$$

Thus, the two IM3 mechanisms, force intermodulation 1) and current intermodulation 2), can be summarized as:

1) & 2) Interfering signal: $\bar{u}_{\text{int}}(\omega_1,\omega_2)$
$\xrightarrow{(6)(b)}$ interfering force: $F_{\text{int}}(\omega_1,\omega_2)$
$\xrightarrow{(9)}$ linear displacement: $\xi_{\text{int}}(\omega_1,\omega_2)$

1) linear displacement $\xi_{\text{int}}(\omega_1,\omega_2)$
$\xrightarrow{(6)(f,g,h)}$ IM3 force: $F_{\text{IM3}}(\omega_0)$
$\xrightarrow{(9)}$ IM3 displacement: $\xi_{\text{IM3}}(\omega_0)$
$\xrightarrow{(12)}$ IM3 current: $\bar{i}_{\text{IM3}}^{(1)}(\omega_0)$.

2) linear displacement $\xi_{\text{int}}(\omega_1,\omega_2)$
$\xrightarrow{(12)}$ IM3 current $\bar{i}_{\text{IM3}}^{(2)}(\omega_0)$

The approximative nature of the analysis is mainly due to the IM3 displacement being only a first-order estimate of the solution to the nonlinear equation of motion (6).

After some algebra, the current contributions $\bar{i}^{\mathrm{I1}}_{\mathrm{IM3}}$, $\bar{i}^{\mathrm{Q1}}_{\mathrm{IM3}}$, $\bar{i}^{\mathrm{I2}}_{\mathrm{IM3}}$, and $\bar{i}^{\mathrm{Q2}}_{\mathrm{IM3}}$ in (17) and(18) can be written as

$$\bar{i}^{\mathrm{I1}}_{\mathrm{IM3}} = \frac{1}{4}\eta H_0''\omega_e^4\omega_0\bar{u}^3_{\mathrm{int},0} \left\{2H_1' + H_2' + 3\left[H_1'^2 - H_1''^2 + 2H_1'H_2' + 2H_1''H_2''\right]\omega_e^2 + 3\left[\left(H_1'^2 - H_1''^2\right)H_2' + 2H_1'H_1''H_2''\right] \times \left(4 - \bar{k}_3\right)\omega_e^4\right\}, \tag{21a}$$

$$\bar{i}^{\mathrm{Q1}}_{\mathrm{IM3}} = -\frac{1}{4}\eta H_0''\omega_e^4\omega_0\bar{u}^3_{\mathrm{int},0} \left\{2H_1'' - H_2'' + 6\left[H_1'H_1'' + H_1''H_2' - H_1'H_2''\right]\omega_e^2 + 3\left[\left(H_1''^2 - H_1'^2\right)H_2'' + 2H_1'H_1''H_2'\right] \times \left(4 - \bar{k}_3\right)\omega_e^4\right\}, \tag{21b}$$

$$\bar{i}^{\mathrm{I2}}_{\mathrm{IM3}} = \frac{3}{4}\eta\omega_e^6\omega_0\bar{u}^3_{\mathrm{int},0}\left[\left(H_1''^2 - H_1'^2\right)H_2'' + 2H_1'H_1''H_2'\right], \tag{21c}$$

$$\bar{i}^{\mathrm{Q2}}_{\mathrm{IM3}} = \frac{3}{4}\eta\omega_e^6\omega_0\bar{u}^3_{\mathrm{int},0}\left[\left(H_1'^2 - H_1''^2\right)H_2' + 2H_1'H_1''H_2''\right]. \tag{21d}$$

Equations (21a) and (21c) give the amplitude of the in-phase intermodulation current $\bar{i}^{\mathrm{I}}_{\mathrm{IM3}}$ (20a), while (21b) and (21d) give the quadrature-phase current $\bar{i}^{\mathrm{Q}}_{\mathrm{IM3}}$ (20b). The signal-to-interference (or signal-to-intermodulation) ratio (SIR) can now be expressed as

$$\mathrm{SIR} = \frac{\bar{i}^{\mathrm{I}}_{\mathrm{sig}}}{\sqrt{\left(\bar{i}^{\mathrm{I}}_{\mathrm{IM3}}\right)^2 + \left(\bar{i}^{\mathrm{Q}}_{\mathrm{IM3}}\right)^2}}. \tag{22}$$

At the limit $Q \to \infty$, (22) is determined by the first in-phase current component $\bar{i}^{\mathrm{I1}}_{\mathrm{IM3}}$ of (21a) only. This is seen from the limits of the response functions as $Q \to \infty$: $H_0'' \to \infty$, $H_{i\neq 0}' \to 1/\left(\omega_0^2 - \omega_i^2\right) = \text{finite}$ and $H_{i\neq 0}'' \to 0$. Thus $\bar{i}^{\mathrm{I1}}_{\mathrm{IM3}}$ is the only nonlinear current component that goes to infinity in addition to the linear current $\bar{i}^{\mathrm{I}}_{\mathrm{sig}}$ in (22) resulting in finite SIR. The quadrature currents in (21b) and (21d) approach a finite value while $\bar{i}^{\mathrm{I2}}_{\mathrm{IM3}}$ in (21c) vanish as $Q \to \infty$. Consequently, (22) simplifies considerably as shown by (23) at the bottom of the page where $\Gamma \equiv \bar{u}_{\mathrm{int},0}/\bar{u}_{\mathrm{sig},0}$ is the interference-to-signal ratio at the filter input. As will be illustrated with measurements in Section III, (22) can actually be approximated by (23) as soon as the interfering signals are outside the resonator passband. The labels (f), (g) and (h) in (23) correspond to those in (6) showing the origin of different SIR contributions. As (23) contains odd powers of $\Delta\omega$, it is asymmetric around the resonance predicting different SIR values for interferers below the resonance and interferers above the resonance. Especially, the odd-order term labeled (g) in (23) proves to be important in Section III.

The third-order intercept point (IP3) is a useful measure of linearity and is typically defined as the crossing point of the linear extrapolations of the small-amplitude IM3 signal and a fundamental two-tone test signal in the device output. For frequency selective components such as filters, the above definition may be modified as IP3 being the crossing point of the linear extrapolations of the IM3 output signal and a wanted output signal when the wanted signal has the same input magnitude as the interferers and is located at the passband center. The signal level at the filter input, corresponding to IP3, is termed IIP3 and is found from SIR as [11]

$$\bar{u}^2_{0,\mathrm{IIP3}} = \frac{\mathrm{SIR}\bar{u}^3_{\mathrm{int},0}}{\bar{u}_{\mathrm{sig},0}} = \mathrm{SIR}\bar{u}^2_{\mathrm{sig},0}\Gamma^3. \tag{24}$$

Alternatively, IIP3 is obtained by setting $\Gamma = \bar{u}_{\mathrm{int},0}/\bar{u}_{\mathrm{sig},0} = 1$ in (22) or (23) and solving for the signal amplitude that gives $\mathrm{SIR} = 1$.

The in-band result, given in [10], is obtained in the limit $\Delta\omega \to 0$ and $\bar{k}_3 \to 0$. With nonvanishing mechanical nonlinearities $\left(\bar{k}_3 \neq 0\right)$, the result of [10] is slightly modified to

$$\bar{u}^2_{0,\mathrm{IIP3},\Delta\omega=0} = \frac{1}{\sqrt{\left[3\left(\frac{1-\bar{k}_3}{4}\right)q^3 + \frac{q}{4}\right]^2 + \frac{9q^4}{4}}} \tag{25}$$

where

$$q \equiv \frac{k_e Q}{\bar{k}} = \frac{Q\omega_e^2}{\omega_0^2} \approx \frac{Q}{\beta}\left(\frac{V}{U_{\mathrm{pi}}}\right)^2. \tag{26}$$

Here the approximation is valid if $k_e \ll k \Leftrightarrow V \ll U_{\mathrm{pi}}$ and the electromechanical pull-in voltage, at which bias level the resonator becomes unstable, is

$$U_{\mathrm{pi}} = \sqrt{\frac{k_b d^2}{\beta C_0}} \tag{27}$$

where $\beta = 2$ for $\varphi = 1$ (bias forces act at opposite directions on the resonator) and $\beta = 27/8$ for $\varphi = -1$ in (1). As discussed in [10] the strongest contribution in (25) for high q is due to the ξ^3 nonlinearity in (6) (f). On the other hand, as the interferers are moved far outside the passband, the ξ^3 term becomes unimportant in SIR.

III. Experimental Verification

To verify the intermodulation model, narrow gap single-crystal silicon (SCS) resonators fabricated on silicon-on-insulator (SOI) wafers were characterized with linear and nonlinear

$$\mathrm{SIR}_\infty = \frac{16|\Delta\omega|^3(\omega_0+\Delta\omega)(2\omega_0+\Delta\omega)^2}{\left[\underset{(h)}{9\Delta\omega^4} + \underset{(h)}{28\Delta\omega^3\omega_0} + \underset{(h)}{2\Delta\omega^2}\left(\underset{(h)}{10\omega_0^2} - \underset{(g)}{9\omega_e^2}\right) - \underset{(g)}{24\Delta\omega\omega_e^2\omega_0} + 3\left(4 - \underset{(f)}{\bar{k}_3}\right)\omega_e^4\right]\Gamma^3\bar{u}^2_{\mathrm{sig},0}\omega_e^2} \tag{23}$$

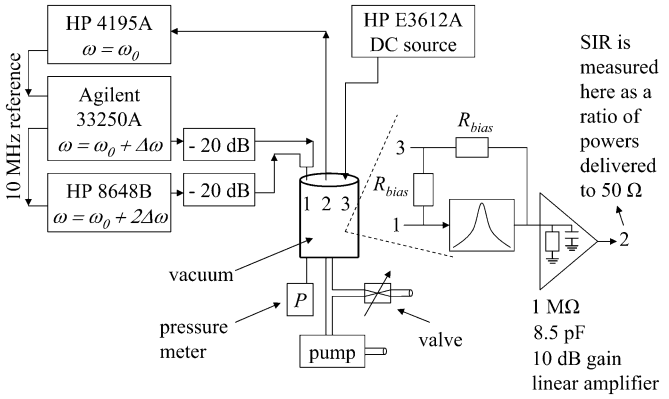

Fig. 2. Measurement setup. Pressure (P) in the vacuum chamber is measured and controlled using the valve to vary the Q value of the resonator.

excitation. As the fabrication process is detailed elsewhere [12], only the experimental setup and results are given here.

A. Measurement Setup

Fig. 2 shows the measurement setup used to validate the analytical results. The resonator is kept in a vacuum chamber together with a JFET preamplifier that has a gain of 10 dB, an input resistance of 1 $\mathrm{M}\Omega$, and an input capacitance of 8.5 pF. Pressure in the camber is controlled with a valve to tune the Q value of the resonator. To measure the intermodulation at ω_0, signals at $\omega_0+\Delta\omega$ and $\omega_0+2\Delta\omega$ are generated and summed at the resonator input. The signal generators (Agilent 33250A and HP 8648B) are isolated with 20 dB attenuators to prevent intermodulation at the signal sources. The resonator output signal is buffered with a preamplifier and measured with a spectrum analyzer (HP 4195A). As the preamplifier is kept in its linear range, it does not affect the SIR. The signal generators and the spectrum analyzer are locked to a common frequency reference. The desired-signal output power is measured with one of the signal generators turned off and the other tuned to ω_0.

B. Simulation Model

To accurately model the characterized microresonators, the resonator, the electric biasing, and read-out circuitry are implemented in a circuit simulator [14]. The resonator is modeled as an electrical equivalent of the spring-mass system in Fig. 1. For the capacitive coupling, the accurate nonlinear model is used [13]. The simulations are used: i) to obtain good estimates of the mechanical and electrical parameters by fitting the simulated transmission curves to the measured responses and ii) to verify the analytical model of the intermodulation. For the intermodulation simulations, the large-signal harmonic-balance analysis with multiple input and output signal tones is used. As the harmonic-balance analysis is carried out in the frequency domain, it is computationally efficient for systems that have high quality factors and are thus slow to settle in the time-domain (transient) analysis [15]. Schematic of the simulation setup is shown in Fig. 3.

C. BAW Resonator

Fig. 4(a) shows the schematic of a bulk-acoustic-wave (BAW) resonator oscillating in the square-extensional mode [3]

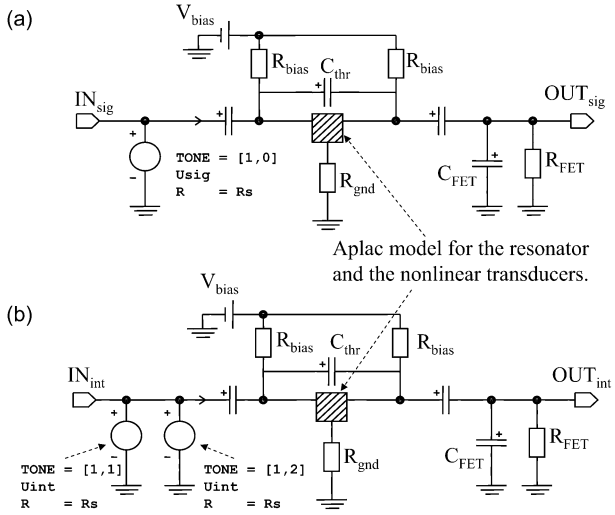

Fig. 3. Schematic of the harmonic-balance Aplac®-circuit-simulator model [13] for the desired signal (a) and the interferers (b). The model for the resonator (see Fig. 1) and the nonlinear transducers are included in the shaded three-port components. SIR is determined as the ratio of $\mathrm{OUT_{sig}}$ voltage to $\mathrm{OUT_{int}}$ voltage at the fundamental frequency.

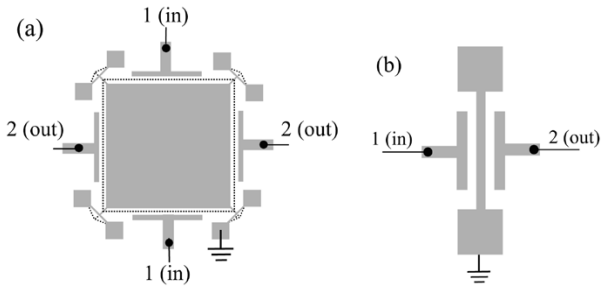

Fig. 4. Schematics of the two experimentally characterized resonators. Also indicated are the input and output ports corresponding to 1 and 2 in Fig. 2. (a) BAW resonator in the square-extensional mode [3]. The dotted lines illustrate the movement of the plate from the rest position. The two input ports as well as the two output ports are electrically shorted. (b) Clamped-clamped flexural beam resonator [10].

for which $\varphi=-1$ in (1) (all the faces of the square plate move in phase). The resonator is fabricated on a silicon-on-insulator (SOI) wafer and has a size of 320 μm$\times$ 320 μm$\times$ 10 μm. Two transducers at opposite sides of the square plate are used for signal input and output. Fitting the simulated response to measured behavior at different bias voltages, as shown in Fig. 5, allows one to find the equivalent-model parameters given in Table II. Fitting was done by adjusting the spring constant k_b, eigenfrequency ω_b, Q value, feed-through capacitance C_{thr}, gap d, and R_{gnd} that is a parasitic contact resistance at the ground connect of the resonator and accounts for the weakening of the antiresonance in Fig. 5(a). The same order of DC resistance for R_{gnd} was also measured. As the capacitive nonlinearity is the dominant effect, the mechanical nonlinearities k_2 and k_3 are neglected (for the 184 nm gap, the capacitive nonlinearity dominates at bias voltages greater than 2.5 V) [5]. With a 5.77 V bias voltage, corresponding to the middle curve in Fig. 5, the theoretical estimate of in-band IIP3 given by (22) is 21 dBm (corresponding to a 50 Ω source impedance) and the estimate for off-resonance interferers with $\Delta f=1$ kHz, given by (23) and (24), is $\mathrm{IIP3}=38$ dBm.

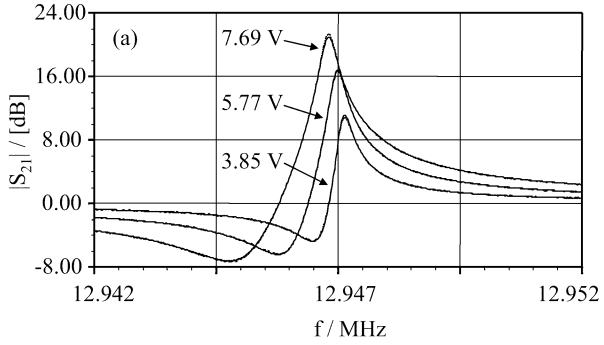

(a) Amplitude of S_{21}. The antiresonance is weakened due to nonzero resistance in the ground connect of the resonator.

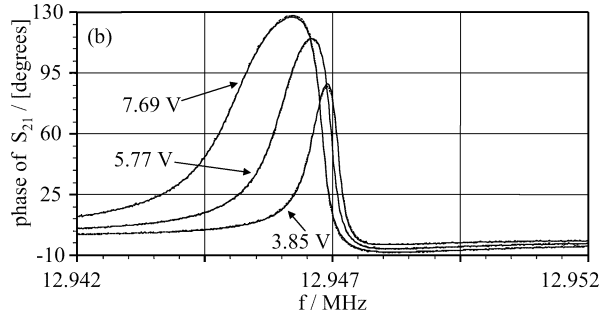

(b) Phase of S_{21}.

Fig. 5. Measured (dashed lines) and simulated (solid lines) S_{21} for the BAW resonator with three different bias voltages. The result is calibrated with a zero-bias response, that is, S_{21} is defined as the ratio of the motional current through the electrical-equivalent RLC circuit of Fig. 1 to the parasitic feed-through current through $C_{\rm thr}$. Measured and simulated results differ slightly only at the peaks of the curves.

TABLE II
PARAMETER VALUES FOR THE BAW RESONATOR. VALUES AT THE BOTTOM ROW ARE FOR 5.77 V BIAS VOLTAGE

k_b	16.3 MN/m	f_b	12.947 MHz	$U_{\rm pi}$	730 V
d	184 nm	Q	46900	k_e	300 N/m
C_0	307 fF	$C_{\rm thr}$	35.4 fF	$R_{\rm gnd}$	1.2 kΩ
R_m	46.2 kΩ	L_m	26.6 H	C_m	5.67 aF

Fig. 6(a) shows the measured, simulated and analytic results, all in very good agreement, for the SIR as a function of interferer separation at the output of the BAW resonator with the signal (13a) and interferer (13b) input powers of $P_{\rm sig} = -50$ dBm and $P_{\rm int} = 0$ dBm, respectively. The large interferer power was chosen to obtain a sufficient signal-to-noise ratio in the measurements. The infinite-Q limit of (23) becomes valid as soon as the interferers are outside the resonator passband of $\Delta f_{3\rm dB} = f_0/Q \approx 300$ Hz for $Q = 46\,900$ in vacuum. Also, as predicted from the theory, at intermediate frequencies of 50 Hz $< |\Delta f| <$ 1 kHz we observe that the SIR is much lower for interferers below the resonance ($\Delta f < 0$) than for interferers above the resonance ($\Delta f > 0$). The difference between the SIR for $\Delta f > 0$ and $\Delta f < 0$ is at greatest when the interferer frequencies are close to the 3-dB-passband edge of the resonator. Of the odd-order $\Delta\omega$ terms in (23) that explain this difference, the one originating from (g) in (6) dominates.

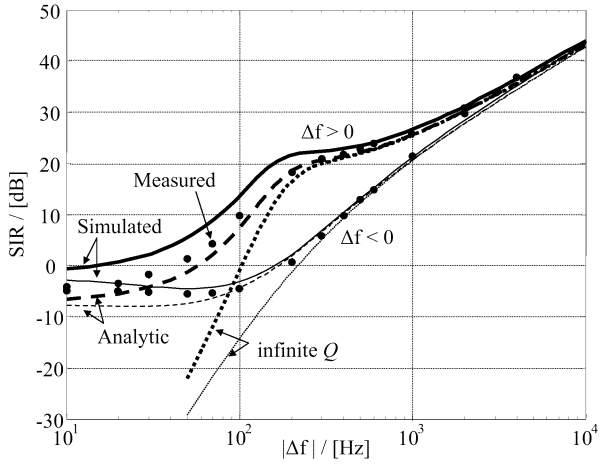

(a) Signal-to-intermodulation ratio with $Q = 46900$ as a function of interferer frequency separation Δf.

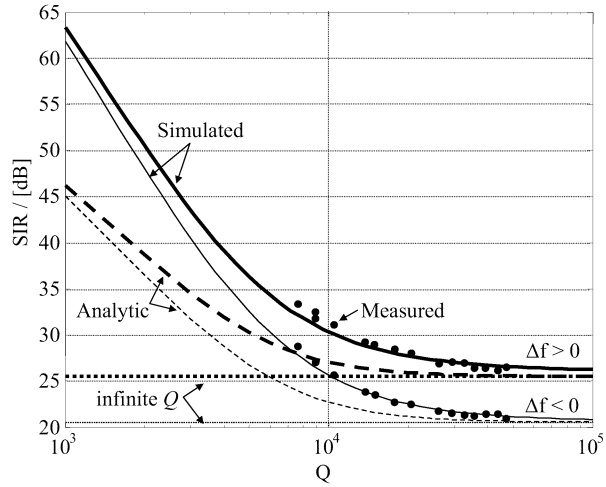

(b) Signal-to-intermodulation ratio as a function of resonator Q value with $|\Delta f| = 1$kHz.

Fig. 6. Simulated (solid), analytic (22) (dashed), analytic for $Q \to \infty$ (23) (dotted) and measured (large dots) intermodulation results for the BAW resonator are shown for $\Delta f < 0$ (thin lines) and $\Delta f > 0$ (thick lines). Bias voltage is 5.77 V corresponding to the middle curve in Fig. 5. The signal and interferer input powers are $P_{\rm sig} = -50$ dBm and $P_{\rm int} = 0$ dBm.

Fig. 6(b) shows the SIR at constant interferer separation for different quality factors obtained by adjusting the chamber pressure. At low Q, the analytic estimates expectedly deviate from the measured and simulated results due to the approximations utilized in Section II. Increasing Q reduces SIR toward the infinite-Q limit (23).

Fig. 7 shows the different intermodulation current components $\bar{i}^{\rm I1}_{\rm IM3}$, $\bar{i}^{\rm Q1}_{\rm IM3}$, $\bar{i}^{\rm I2}_{\rm IM3}$, and $\bar{i}^{\rm Q2}_{\rm IM3}$ in (21a)–(21d) as functions of the interferer frequency separation. It is seen that the force intermodulation mechanism 1) dominates over the current intermodulation 2), that is, $\left|\bar{i}^{\rm I1}_{\rm IM3}\right| \geq \left|\bar{i}^{\rm I2}_{\rm IM3}\right|$ and $\left|\bar{i}^{\rm Q1}_{\rm IM3}\right| \geq \left|\bar{i}^{\rm Q2}_{\rm IM3}\right|$ except at small positive Δf for which $\left|\bar{i}^{\rm I1}_{\rm IM3}\right| < \left|\bar{i}^{\rm I2}_{\rm IM3}\right|$.

D. Flexural Beam Resonator

To have a further justification of the analysis of Section II, we consider a flexural-beam resonator [10], shown schematically in Fig. 4(b), with $P_{\rm sig} = -50$ dBm, $P_{\rm int} = -10$ dBm and

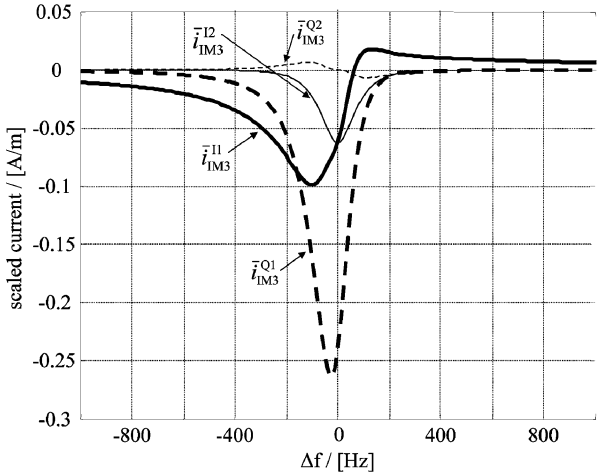

Fig. 7. Intermodulation current contributions (21a)–(21d) for the BAW resonator.

TABLE III
PARAMETERS FOR THE FLEXURAL-BEAM RESONATOR WITH A 13 V BIAS

k_b	8.3 kN/m	f_b	8.452 MHz	$U_{\rm pi}$	102 V
d	188 nm	Q	1803	k_e	66 N/m
R_m	92.6 kΩ	L_m	3.14 H	C_m	115 aF

$V = 13\,\mathrm{V}$. Equivalent-model parameters for the beam resonator are given in Table III.

Fig. 8(a) shows the measured, simulated and analytic results for the SIR as a function of interferer separation. Again, a very good agreement is obtained and the predicted asymmetry in Δf is observed. At small Δf, the analytic result deviates from the measured and simulated. This is because the interferer power is of the same order as the in-band IIP3 point [10] and thus the intermodulation signal at ω_0 is weaker than its analytical estimate. Fig. 8(b) shows the SIR at different quality factors. Here the Q value is considerably lower than for the BAW resonator and as much tuning range is not obtained by varying the pressure in the vacuum chamber.

IV. DISCUSSION

In this paper, a concise formulation for SIR and IIP3 in capacitively coupled micromechanical filters is given. The experimental verification is provided for two single-resonator structures but the formulation applies to all single-stage MEMS filters that are coupled with parallel-plate transducers. Such filters could be used to construct a receiver front-end structure having a bank of narrow-band (ultimately channel-select) filters with different passbands to cover all the RX channels [2]. While the results in the present paper are believed to be indicative of the MEMS filter performance in general, further work is needed to expand the analytical results to more complex multi-stage filter structures. This will be a subject of future research.

In the paper, the motional impedances are much higher (> 40 kΩ) than the source and load impedances (see Figs. 1 and 2). As the analysis has been formulated in terms of input voltages and output currents, the derived expressions for SIR and IIP3 are valid also for tightly coupled resonators with source and load impedances being comparable to or larger than the motional impedance provided that: i) the source and filter input impedances are used to adjust the resonator input voltages and ii) the loaded in-circuit quality factor is used for SIR calculations. What is not taken into account is that in the strongly coupled case, the motional impedance is a strong function of frequency and the different interfering signals now see different mechanical impedances. Consequently, the interference input voltage levels do not remain equal as assumed in this paper. However, simulations show that this effect is not significant. Finally, we note that for strong interferers within the passband, Duffing effect results in signal compression that may also limit the filter performance [5].

The previously obtained experimental IM3 results of [8] for $\Delta f \ll -f_0/Q$ are in good agreement with (23). For example, assuming that the spring constant of the beam can be approximated by the point-force result $k_b = 16YH(w/L)^3$ [16], where Y is the Young modulus, (23) and (24) give the same IIP3 voltage of $V_{\rm IIP}3 \equiv u_{0,\rm IIP3} = 68\,\mathrm{dBmV}$ (corresponding to 18 dBm with a 50 Ω source impedance) as reported in Fig. 5 of [8]. On the other hand, for $\Delta f > 0$ as well as for the interferers close to the passband edge, our results (22)–(24) differ from the analytical results (absolute value of (11)) in [8] by up to 10 dB for the BAW and flexural-beam examples of this paper.

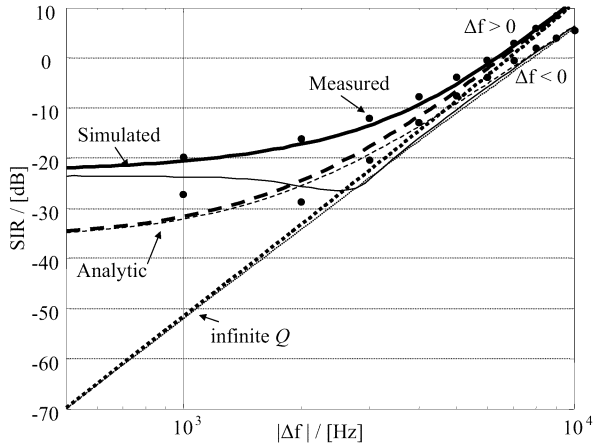

(a) Signal-to-intermodulation ratio with $Q = 1803$ as a function of interferer frequency separation Δf.

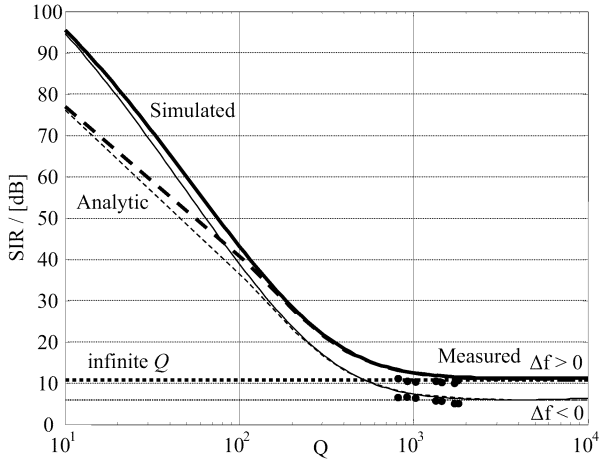

(b) Signal-to-intermodulation ratio as a function of resonator Q value with $|\Delta f| = 10$kHz.

Fig. 8. As Fig. 6 (thick lines for $\Delta f > 0$ and thin lines for $\Delta f < 0$) but for the flexural-beam resonator [10]. Bias voltage is 13 V, $P_{\rm sig} = -50\,\mathrm{dBm}$, and $P_{\rm int} = -10\,\mathrm{dBm}$.

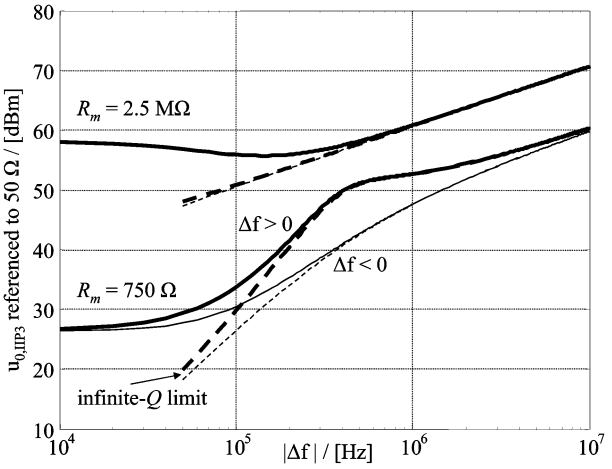

Fig. 9. The theoretical IIP3 voltage from (22)–(24) for the 1.156 GHz resonators of [4]. The curves for $R_m = 2.5\ \mathrm{M}\Omega$ are for a fabricated device while $R_m = 750\ \Omega$ corresponds to a theoretical device.

To further demonstrate the utility of this paper, we consider the recently reported radial-mode 1.156 GHz disk resonators of [4]. Fig. 9 shows the IIP3 voltage, corresponding to a 50 Ω source impedance, given by (22)–(24) for a measured and a theoretical improved resonator. For the fabricated device with a motional resistance of $R_m = 2.5\ \mathrm{M}\Omega$, the SIR is symmetric around the passband. The exceptionally high IIP3 is not suprising as most of the power is reflected due to impedance mismatch. For the theoretical device with $R_m = 750\ \Omega$ that has an improved electromechanical coupling and correspondingly better impedance match and lower IIP3, there is a clear asymmetry of IIP3 with respect to Δf also outside the passband of $\Delta f_{3\mathrm{dB}} = f_0/Q \approx 200\ \mathrm{kHz}$. Both resonators of Fig. 9 have an IIP3 that meet the requirements set, for example, for GSM receivers [17]. On the other hand, the motional resistance is still far from 50 Ω even for the theoretical device. Lower resistances can be obtained, for example, by reducing the gap and/or increasing the bias voltage which, however, lowers the IIP3 [8].

V. Conclusion

Detailed analysis of intermodulation in capacitively coupled MEMS filters was presented and closed form expressions for SIR and IIP3 were derived. It was shown that the force intermodulation mechanism is usually the dominant effect. However, close to or within the filter passband, the current intermodulation mechanism is also important. The analytical results were verified with experiments and simulations and excellent agreement was obtained.

The results of this paper may be used in designing micromechanical filters, for example, for communication applications. Well outside the passband, the obtained SIR does not depend on the quality factor. Within the passband, increasing the quality factor lowers the IIP3. The asymmetry observed near the passband edge results in interferers below the passband being more difficult to block than interferers above the passband.

Acknowledgment

The authors would like to thank J. Kiihamäki for fabricating the microresonators used in the measurements and J. Holmberg for useful discussions concerning the measurements.

References

[1] T. Lee, *The Design of CMOS Radio-Frequency Integrated Circuits*. Cambridge, U.K.: Cambridge University Press, 1998.
[2] C. T.-C. Nguyen, "Frequency-selective mems for miniaturized low-power communication devices," *IEEE Trans. Microw. Theory Tech.*, vol. 47, pp. 1486–1503, Aug. 1999.
[3] V. Kaajakari, T. Mattila, A. Oja, J. Kiihamäki, and H. Seppä, "Square-extensional mode single-crystal silicon micromechanical resonator for low phase noise oscillator applications," *IEEE Electron Device Lett.*, vol. 25, pp. 173–175, Apr. 2004.
[4] J. Wang, Z. Ren, and C. T.-C. Nguyen, "1.156-GHz self-aligned vibrating micromechanical disk resonator," *IEEE Trans. Ultrason., Ferroelect., Freq. Contr.*, vol. 51, pp. 1607–1628, Dec. 2004.
[5] V. Kaajakari, T. Mattila, A. Oja, and H. Seppä, "Nonlinear limits for single-crystal silicon microresonators," *J. Microelectromech. Syst.*, vol. 13, pp. 715–724, Oct. 2004.
[6] H. Tilmans, "Equivalent circuit representation of electromechanical transducers: I. Lumped-parameter systems," *J. Micromech. Microeng.*, vol. 6, no. 1, pp. 157–176, Mar. 1996.
[7] L. Lin, R. T. Howe, and A. P. Pisano, "Microelectromechanical filters for signal processing," *J. Microelectromech. Syst.*, vol. 7, pp. 286–294, Sep. 1998.
[8] R. Navid, J. R. Clark, M. Demirci, and C. T. C. Nguyen, *Proc. Third-Order Intermodulation Distortion in Capacitively-Driven Cc-Beam Micromechanical Resonators*, Interlaken, Switzerland, 2001, pp. 228–231.
[9] T. C. Nolan and W. E. Stark, "Mitigation of cosite interference in nonlinear receivers with mems filters," in *Proc. MILCOM 2000. 21st Century Military Communications Conference*, Oct. 2000, pp. 769–773.
[10] A. T. Alastalo and V. Kaajakari, "Intermodulation in capacitively coupled microelectromechanical filters," *IEEE Electron Device Lett.*, vol. 26, pp. 289–291, May 2005.
[11] B. Razavi, *RF Microelectronics*: Prentice Hall, 1998.
[12] J. Kiihamäki, V. Kaajakari, H. Luoto, H. Kattelus, and M. Ylikoski, "Fabrication of single crystal silicon resonators with narrow gaps," in *Proc. Transducers'05, The 13th International Conference on Solid-State Sensors, Actuators and Microsystems*, Seoul, Korea, Jun. 5–9, 2005, pp. 1354–1357.
[13] T. Veijola and T. Mattila, "Modeling of nonlinear micromechanical resonators and their simulation with the harmonic-balance method," *International Journal of RF and Microwave Computer Aided Engineering*, vol. 11, no. 5, pp. 310–321, Sep. 2001.
[14] Aplac RF Design Tool. APLAC Solutions Corp.. [Online]. Available: www.aplac.com
[15] S. Maas, *Nonlinear Microwave and RF Circuits*, 2nd ed. Norwood, MA: Artech House, 2003.
[16] J. W. Weaver, S. Timoshenko, and D. Young, *Vibration Problems in Engineering*, 5th ed. New York, NY: Wiley, 1990.
[17] "GSM Global System for Mobile Communications," ETSI, 3GPP ts 05.01/05.05, 2003.

Ari T. Alastalo received the M.Sc. degree in technical physics from Helsinki University of Technology (HUT), Finland, in 1997.

From 1996 to 1998 he was an assistant at HUT working in the area of magnetic quantum impurities. From 1998 to 2001, he was with Nokia Research Center carrying out research of radio propagation, RF architectures, baseband algorithms, and protocols for adaptive-antenna systems. Since 2002, he has been a Research Scientist at VTT Information Technology, Finland. His present research focuses on RF MEMS.

Ville Kaajakari received the M.S. and Ph.D. degrees in electrical and computer engineering from University of Wisconsin-Madison in 2001 and 2002, respectively.

He is currently Senior Research Scientist at VTT Information Technology, Finland, where his research interest is RF-MEMS.

PUBLICATION III

Systematic Design Approach for Capacitively Coupled Microelectromechanical Filters

In: IEEE Transactions on Ultrasonics, Ferroelectrics, and Frequency Control 2006. Vol. 53, No. 9, pp. 1662–1670.
Reprinted with permission from the publisher.

Systematic Design Approach for Capacitively Coupled Microelectromechanical Filters

Ari T. Alastalo and Ville Kaajakari, *Member, IEEE*

***Abstract*—A design procedure for microelectromechanical (MEMS) band-pass filters is formulated that takes into account specifications set for carrier-to-interference ratio (C/I) and insertion loss. Since suppressing intermodulation distortion to maximize C/I in MEMS filter design typically leads to increased loss and vice versa, it is necessary to aim at a feasible compromise in filter performance that meets all of the requirements. In order to meet specifications that are typical for a handheld communication terminal, an integrated receiver architecture, where filter input and output impedances other than 50 Ω can be used, is found to be more feasible than resistively terminating the front-end filter at source and load to 50 Ω.**

I. Introduction

Communication systems operate in noisy environments where interferer powers may be 10^{10} times larger than the wanted-signal power. In order to ease the linearity and dynamic-range requirements of the receiver, high-quality-factor analog filters are used to block the interfering signals. Off-chip macroscopic ceramic surface acoustic wave (SAW) or film bulk acoustic resonator (FBAR) filters offer excellent performance but their large size, high cost, and unsuitability for integrated circuit (IC) integration limit their scope of application.

Miniature mechanical resonators, fabricated with microelectromechanical systems (MEMS) technology, are a potential replacement for off-chip filters as they are compact in size and integratable with IC electronics. The potential of miniature filters was already realized in the 1960s, leading to the development of the "resonant-gate transistor"—a field-effect transistor with a vibrating metal gate [1]. However, this early work was plagued by problems with a low quality factor (∼500 at 5 kHz), poor stability of the metal resonator, and limited dynamic range due to nonlinear electrostatic effects arising from the inverse gate capacitance-displacement relationship.

In the 1990s, the advances in processing technology and the tremendous growth of the communication-device market led to renewed interest in micromechanical resonators and filters [2]–[5]. The demonstrated quality factors of MEMS resonators, $Q > 100\,000$ at 10 MHz [6] and $Q > 1\,000$ at 1 GHz [7], are comparable to those of their macroscopic SAW and FBAR counterparts. While the mechanical properties of MEMS resonators now are very promising, the electrostatically coupled resonators characteristically suffer from high electrical impedance due to the weak electromechanical coupling. Increasing the coupling by reducing the electrode gap also increases the nonlinear electrostatic effects leading to trade-off between insertion loss and linearity [8].

In this paper, we quantify the trade-off in MEMS filter performance between the insertion loss and intermodulation distortion. Our prior analysis of filter distortion for the interferers at filter passband [9] and at stopband [10], [11] is summarized and a design procedure for MEMS bandpass filters is formulated in more general terms than in [11]. By means of advanced simulation tools, the analytical and experimental results on intermodulation in capacitively weakly coupled resonators are shown to also hold for higher-order filters as well as for tightly coupled filters. The central challenges for MEMS in high-frequency filter design are identified and exemplified by using the Global System for Mobile Communications (GSM) 900 specifications as a case study. Different filter architectures are compared and bandpass MEMS filters are shown to be more suitable for novel integrated receiver architectures than for the conventional resistive 50-Ω termination at filter input and output.

II. Theory of MEMS Filters

To facilitate practical filter design, the exact theory of MEMS filter distortion for single-stage weakly coupled filters, presented in [9], [10], is generalized to hold for tightly coupled and multi-stage filters. With simplifying assumptions, a set of easy-to-use design equations is derived.

A. Electrical Model

Fig. 1(a) shows a schematic of a MEMS resonator with spring coefficient k, effective mass m, resonance frequency $\omega_{\text{res}} = \sqrt{k/m}$, and dissipation $\gamma = \sqrt{km}/Q$, where Q is the unloaded quality factor of the resonator. The electrical transduction is provided by two capacitive transducers biased with DC voltage V_{bias}. The resonator is electrically grounded. Identifying the electromechanical coupling coefficient $\eta = C_0 V_{\text{bias}}/d$ and electromechanical spring constant $k_e \equiv \eta V_{\text{bias}}/d$, where C_0 is the rest capacitance of the electrostatic transducers and d is the transducer gap, the well-known electrical-equivalent model, shown in

Manuscript received October 13, 2005; accepted April 26, 2006. This work is supported by the Academy of Finland (grant 20542), Aplac® Solutions, VTI Technologies, Okmetic, and Tekes (National Technology Agency of Finland).

The authors are with VTT Technical Research Center of Finland, Tietotie 3, Espoo, FIN-02150, Finland (emails: ari.alastalo@vtt.fi, ville.kaajakari@vtt.fi).

0885–3010/$20.00 © 2006 IEEE

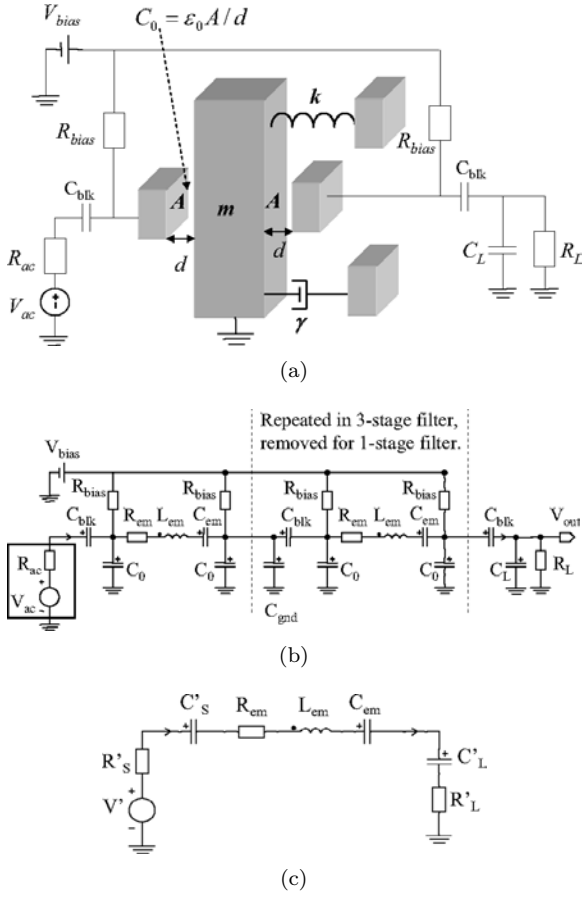

Fig. 1. MEMS resonator and filter models. The DC-blocking capacitance is denoted $C_{\rm blk}$. The electrical equivalent of the resonator in (a) is the RLC series-resonance circuit ($R_{\rm em}$, $L_{\rm em}$, $C_{\rm em}$) with the two shunt capacitors C_0 in (b). Close to the resonance frequency, the single-stage filter has a series equivalent shown in (c). (a) Schematic of a micromechanical resonator (k, m, γ) operating as a single-stage band-pass filter for capacitively coupled signals. (b) Electrical equivalent of a single-stage (a) and multi-stage MEMS filters. Coupling of the filter stages is done with a shunt capacitance $C_{\rm gnd}$. (c) Series equivalent of the single-stage filter.

Fig. 1(b) [3], [4], [12], can be developed. Here, $R_{\rm em} = \gamma/\eta^2$, $L_{\rm em} = m/\eta^2$ and $C_{\rm em} = \eta^2/(k - 2k_e)$ are the resistance-inductance-capacitance (RLC)-equivalent parameters of the MEMS resonator. The inter-stage coupling is represented with a shunt capacitance $C_{\rm gnd}$ but it may be either a physical capacitance or a mechanical spring.

For the single-resonator filter, the loaded in-circuit quality factor Q' can be calculated as

$$Q' = \sqrt{k'm}/\gamma'. \tag{1}$$

Here,

$$\gamma' = \eta^2 \left(R_{\rm em} + R'_S + R'_L\right), \tag{2}$$

$$k' = \eta^2 \left(1/C_{\rm em} + 1/C'_S + 1/C'_L\right), \tag{3}$$

where R'_S, C'_S, R'_L, and C'_L are the narrow-band series-equivalent resistances and capacitances of the parallel source ($R_{\rm ac}||C_0$) and load ($R_L||(C_0+C_L)$) circuits, respectively, given by

$$R'_S = \frac{R_{\rm ac}}{(R_{\rm ac}\omega_0 C_0)^2 + 1}, \tag{4}$$

$$C'_S = \frac{C_0\left[(R_{\rm ac}\omega_0 C_0)^2 + 1\right]}{(R_{\rm ac}\omega_0 C_0)^2}, \tag{5}$$

$$R'_L = \frac{R_L}{\left[R_L\omega_0(C_0 + C_L)\right]^2 + 1}, \tag{6}$$

$$C'_L = \frac{(C_0 + C_L)\left\{\left[R_L\omega_0(C_0 + C_L)\right]^2 + 1\right\}}{\left[R_L\omega_0(C_0 + C_L)\right]^2}, \tag{7}$$

and $\omega_0 = \omega' \equiv \sqrt{k'/m}$ is the loaded resonance frequency. In addition to the loaded Q value of (1), the Thévenin-equivalent input voltage

$$V'_{\rm ac} = V_{\rm ac}\frac{1}{1 + j\omega C_0 R_{\rm ac}} \tag{8}$$

must be used in order to utilize the unloaded third-order input intercept point (IIP3) and signal-to-intermodulation ratio (SIR) results of [9] and [10] for tightly coupled filters, as in what follows.

B. Intermodulation

In filter applications, signal intermodulation (IM) due to odd-order nonlinearities is especially detrimental as it can lead to unwanted frequency components within the filter passband. For example, cubic mixing of two fundamental signals having frequencies ω_1 and ω_2 results in third-order intermodulation (IM3) products at frequencies $2\omega_1 - \omega_2$ and $2\omega_2 - \omega_1$. If $\omega_1 = \omega_0 + \Delta\omega$ and $\omega_2 = \omega_0 + 2\Delta\omega$, the IM product at $2\omega_1 - \omega_2$ is at the passband center frequency ω_0, corrupting the desired signal.

The SIR in the output of a capacitively coupled MEMS single-resonator filter for interferers outside the passband is given in [10] for a general case. For present purposes, we assume that: 1) the passband desired-signal frequency ω_0 is much higher than the frequency separation $\Delta\omega$ to the interferers present in the filter input at frequencies $\omega_1 = \omega_0 + \Delta\omega$ and $\omega_2 = \omega_0 + 2\Delta\omega$; 2) the bias voltage is much lower than the electromechanical pull-in voltage at which bias level the resonator becomes unstable; and 3) mechanical nonlinearities in the spring k of Fig. 1(a) can be ignored as much weaker than the capacitive transducer nonlinearities. With these assumptions, (23) of [10] simplifies as

$$\mathrm{SIR} = \frac{8\,|\Delta\omega|\,\omega_0\,V_{\rm bias}^2\sqrt{P_{\rm sig}}}{5\,\omega_e^2\,R'_S\,P_{\rm int}\sqrt{P_{\rm int}}}, \tag{9}$$

where $\omega_e \equiv \sqrt{k_e/m}$. It is convenient to use (9) for filter design instead of the general solution of [10] because (9) can be solved for the gap d in the closed form (ω_e and R'_S are functions of d). The AC-source powers (see Fig. 1) for the signal and interference are $P_{\rm sig} = V_{\rm ac,sig}^2/(2R_{\rm ac})$ and

$P_{\rm int} = V_{\rm ac,int}^2/(2R_{\rm ac})$, respectively. The AC power corresponding to the IIP3 is related to the SIR as

$$P_{\rm IIP} = {\rm SIR}\sqrt{\frac{P_{\rm int}^3}{P_{\rm sig}}}. \quad (10)$$

When the interferers are inside the passband, we have [9]

$$P_{\rm IIP}^{\rm IB} = \frac{V_{\rm bias}^2}{R_S'\sqrt{(6q^3+q/2)^2+9q^4}}, \quad (11)$$

where $q \equiv Q'\,\omega_e^2/\omega_0^2 = Q'\,k_e/k'$.

C. Insertion Loss

The passband voltage gain is

$$G_V = \frac{V_{\rm out}}{V_{\rm ac}/2} = \frac{2}{\omega_0 C_L'(R_S' + nR_{\rm em} + R_L')}\frac{|1+j\omega_0 C_L' R_L'|}{|1+j\omega_0 C_0 R_{\rm ac}|}, \quad (12)$$

where n is the filter order and R_S', $R_{\rm em}$, R_L', $R_{\rm ac}$, C_L', C_0, $V_{\rm ac}$, and $V_{\rm out}$ are as shown in Fig. 1. We note that with a dominantly capacitive termination ($|1/\omega_0 C_L'| > R_L'$) it is possible to obtain voltage gain because the filter acts as an RLC impedance transformer.

III. Model Verification

The validity of the analytical SIR model has been verified by harmonic-balance Aplac® circuit simulations [13], [14] and experiments for single-stage filters [9], [10]. In what follows, simulations with one-, two-, and three-stage filters are performed to show that the analytical SIR model can also be applied for higher-order filters as well. Moreover, by analyzing 1-GHz MEMS filters and comparing their performance to GSM specifications, it is shown that the simplified expressions (9) and (11) suffice to estimate the linearity properties of MEMS filters.

A. 13-MHz Band-Pass Filters

We consider the one-, two-, and three-stage filters of Fig. 1 with the 13-MHz bulk acoustic wave (BAW) MEMS resonators of [10] where $Q = 47000$ but with a reduced gap of 25.5 nm in order to have a low mechanical impedance of 38 Ω. The other relevant resonator parameters are summarized in Table I. We use $C_{\rm gnd} = 20$ pF and $C_{\rm gnd} = 30$ pF for the two-stage and three-stage filters, respectively. Furthermore, we use a resistive termination with $C_L = 0$ and $R_L = R_{\rm ac}$ in Fig. 1. What is not included is a parasitic feed-through capacitance between input and output that would reduce the stopband attenuation of the filters but would not affect the intermodulation properties.

Fig. 2 shows simulated responses of the filters with 2 Ω (unloaded, $R_{\rm ac} \ll R_{\rm em}$) and 450 Ω (loaded, $R_{\rm ac} \gg R_{\rm em}$) source and load impedances. The 450-Ω source and load yields $Q' = 1900$ for the in-circuit quality factor (1) of the resonator. The unloaded case is not useful as a filter due to the large insertion loss and ripple in the passband. The loaded cases demonstrate that, with increasing filter order, the stopband slope steepens but the insertion loss increases also due to the increasing series resistance at resonance.

TABLE I
Parameters for the BAW Resonator.

k	16.3 MN/m	$f_{\rm res}$	13 MHz	Q	47000
d	25.5 nm	C_0	2 pF	$U_{\rm pi}$	38 V
$V_{\rm bias}$	3.8 V	η	335 μFV/m	k_e	51 kN/m
$R_{\rm em}$	38 Ω	$L_{\rm em}$	22 mH	$C_{\rm em}$	7 fF

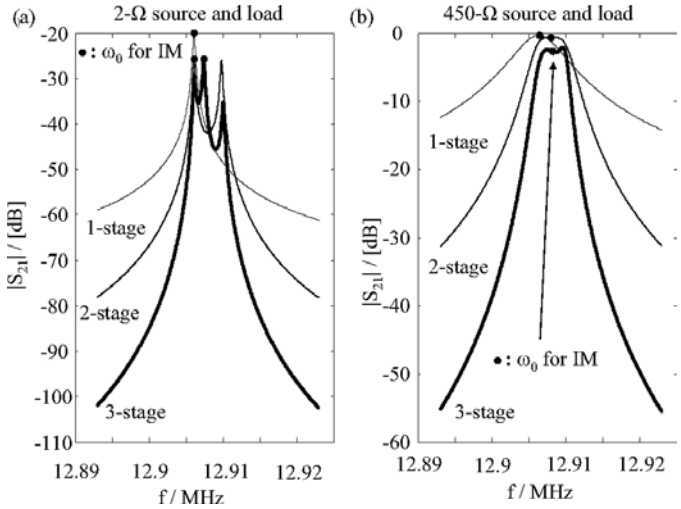

Fig. 2. Unloaded (a) and loaded (b) responses of the filters composed of one, two, and three BAW resonators, as shown in Fig. 1. The desired-user frequency ω_0 for the SIR results of Fig. 3 is marked with a dot.

Fig. 3 shows the analytic and simulated SIR for the filters with ω_0 as indicated in Fig. 2. A different choice for ω_0 within the passband would be equally justified. The analytic results, calculated with the exact formulas of [10] for the single-stage filter, are in excellent agreement with the simulations. Moreover, for out-of-band interferers with $\Delta\omega \to \infty$, the approximate expression (9) (marked as approximation in Fig. 3) becomes valid. It is seen that outside the passband the unloaded single-resonator result is also valid for the higher-order filters as well as for the tightly coupled filters provided that the loaded quality factor of (1) and the Thévenin-equivalent input voltage of (8) are used. Intuitively, this is to be expected because for the out-of-band interferer frequencies, the resonator impedances are high and the resonators are therefore only weakly coupled. Thus, the first resonator and the first transducer effectively set the SIR. At some frequencies close to the passband edge, the numerical harmonic-balance simulation does not converge for the unloaded two-stage and three-stage filters. This is seen in the discontinuities of the corresponding curves of Fig. 3 with $R_{\rm ac} = 2$ Ω.

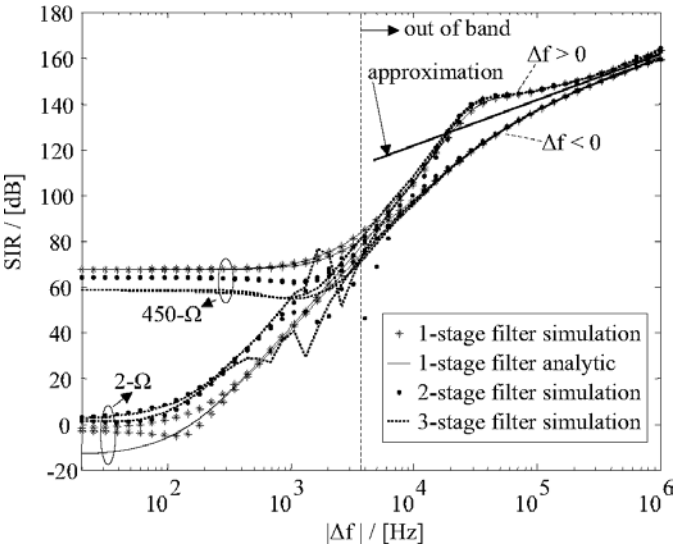

(a)

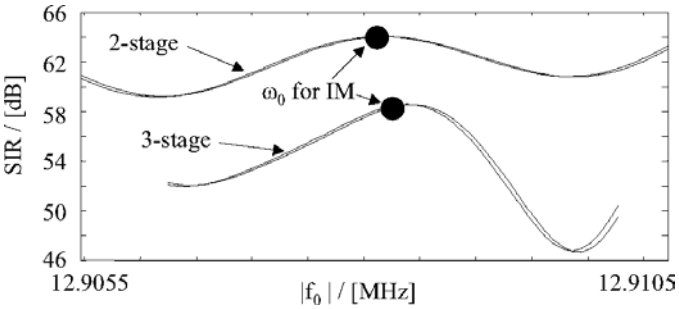

(b)

Fig. 3. Signal-to-intermodulation ratio as a function of the interferer frequency separation $\Delta f = \Delta\omega/(2\pi)$ for the filters of Fig. 2. (a) SIR as a function of Δf for the filters of Fig. 2 with a −20 dBmV desired signal at ω_0, marked with a dot in (b) and in Fig. 2, and with 0 dBmV interferers. The result given by (9), used in this paper for filter design, is marked approximation. (b) In-band SIR for the loaded two-stage and three-stage filters in (a) with $\Delta f = 20$ Hz and with the signal frequency $f_0 = \omega_0/(2\pi)$ swept across the passband.

For the single-stage filters in Fig. 3, the in-band approximation (11) approaches the exact results as $\Delta\omega \to 0$. Namely, (11) and (10) give SIR = −13.4 dB (IIP3 = 3.3 dBmV) and SIR = 67 dB (IIP3 = 43.5 dBmV) for the unloaded and loaded single-stage filters, respectively. The higher source and load resistances result in a lower loaded quality factor of the filter and thus a higher SIR. The deviation of the analytical estimate from the simulated results for the unloaded filter, when $\Delta f \to 0$, is understood since the interferer voltage of 0 dBmV is of the same order as the IIP3 input voltage of 3.3 dBmV. Consequently, for such strong interferers, harmonics higher than third order, that are not taken into account in theory, become important and reduce the gain for the IM3 products.

For the higher-order filters, the in-band SIR is seen to depend on the chosen ω_0 within the passband as demonstrated in Fig. 3(b). This is expected because the S_{21} also has ripples as the coupled resonators move in and out of phase. However, the single-stage approximation is still shown to be a good order-of-magnitude estimation.

TABLE II
PARAMETERS FOR THE 1-GHZ FILTER CONFIGURATIONS.*

	A	B	C	Units
V_{bias}	40	**147**	**16**	V
d	30	30	**10**	nm
ω_e	152	560	316	10^6 rad/s
R_{ac}	1000	50	50	Ω
R'_S	690	49.9	49.5	Ω
R_{em}	663	49	51	Ω
C_0	93	93	278	fF
Q'	2500	2500	2600	
f'	1.149	1.143	1.148	GHz
G_V	−16	8.3	6.7	dB

*(A) The theoretical resonator of [7]; (B) same as (A) but scaled to $R_{\text{em}} \approx 50$ Ω by increasing the bias voltage; (C) same as (A) but scaled to $R_{\text{em}} \approx 50$ Ω by reducing the gap.

TABLE III
SIR FOR THE RESONATORS OF TABLE II USED AS A FILTER FOR GSM 900.*

GSM 900		resulting SIR			
Δf	P_{int}	A	B	C	
−10	0	**−2**	**14**	**−10**	outside GSM-RX band
−3	−23	55	63	44	
−0.6	−43	96	87	76	
0.6	−43	111	90	85	
3	−23	59	77	58	
10	0	**−1**	**28**	**−5**	outside GSM-RX band
± 10	0	**−2**	**21**	**−8**	(9)
MHz	dBm	dB	dB	dB	

*The approximation (9) gives a good estimate for $|\Delta f| = 10$ MHz. The signal power ($P_{\text{sig}} = -99$ dBm) and the interferer powers (P_{int}) are as specified in [15].

B. 1-GHz Single-Stage Filters

As another example, we consider 1-GHz single-stage filters based on the resonators of [7] with $k = 373.1$ MN/m, $f_{\text{res}} = 1.150$ GHz, and $Q = 5100$. The load of the filter is now taken to be an FET amplifier stage with $R_L = 1$ MΩ and $C_L = 1$ pF in Fig. 1. This does not reduce the in-circuit Q value (1) as much as the resistive termination at both sides of the filter. Furthermore, by effectively tapping the mechanical RLC resonator, voltage gain becomes attainable, enabling the use of resonators with $R_{\text{em}} \sim 1$ kΩ without introducing significant signal attenuation. The filter input is thought to be directly connected to an antenna, where different impedances can be realized, but the different impedance levels can also be realized with a transformer. For a given impedance level, the source voltage V_{ac} is calculated from the source power level.

Table II shows relevant parameters for three different filter configurations where (A) is based on the resonator of [7] whereas for (B) and (C) the mechanical impedance is reduced to $R_{\text{em}} \approx 50$ Ω by changing the bias voltage and the gap. Table III shows the resulting SIR when the filters (A), (B), and (C) of Table II are used as a front-end filter for GSM 900. As the filter passband is narrower here than

the GSM-RX band, one would need a multitude of such filters with different center frequencies to cover all of the channels. The filters could be connected in parallel or a switch could be used to select only one of the filters, corresponding to a particular channel, to be used at a time. The signal and interference powers in Table III are as specified for a desired signal and for blockers in [15]. Furthermore, we assume two blockers of equal amplitude at frequencies $f_0+\Delta f$ and $f_0+2\Delta f$ to interfere with the desired signal at f_0. The same SIR is found in simulations and with the theory of [10]. The approximation (9) gives a good estimate for $|\Delta f| = 10$ MHz. It is seen that two 0-dBm interferers at 10-MHz and 20-MHz separation from the desired signal reduce the SIR below acceptable levels except for filter (B) for which the bias voltage is not feasible at least in portable devices. For these interferers, marked as outside GSM-RX band in Table III, the desired-user frequency is taken to be at the edge of the GSM-RX band.

As the results in Table III clearly show, the hardest linearity requirements are set by the 0-dBm out-of-GSM-RX-band interferers at 10 MHz and 20 MHz off the desired-signal frequency[1]. As the SIR for the other interferers is easily sufficient, it is enough to use the simplified expression (9) as a starting point for filter design. Moreover, successful filter design is not trivial and a systematic design approach is needed. This is developed in Section IV.

IV. Filter Design

In what follows, we derive design criteria for the resonator dimensions, transducer gap, Q value, and bias voltage from specified in-band and out-of-band filter attenuation and maximum distortion. The criteria yield a systematic procedure to design MEMS filters for communication applications.

A. Out-of-Band Attenuation

For minimum performance, the filter should suppress the interferers situated outside the systems reception (RX) band to the same level as the strongest interferers within the RX band. If this is achieved, the linearity requirement for the low noise amplifier (LNA) and mixer are set by the in-band interferers that normally are not affected by band-select filtering. Denoting the minimum attenuation at frequency f with respect to the desired-signal frequency f_0 (selectivity) as $A_{\min}$, the minimum required in-circuit Q' value in (1) can be derived. For the single-stage MEMS filter, this leads to

$$Q' \geq \frac{\sqrt{A_{\min}^2 - (f/f_0)^2}}{\left|1-(f/f_0)^2\right|} \equiv Q'_{\min}. \tag{13}$$

[1]The intermodulation performance for out-of-band blockers is not clearly defined in the GSM specifications. However, the out-of-band intermodulation is known to set the strongest linearity requirements in code division multiple access (CDMA) design [16]. The out-of-band intermodulation is therefore considered also for GSM.

Increasing the filter order makes the stopband response a steeper function of frequency, and thus a lower quality factor for the resonators is sufficient at the cost of a higher insertion loss.

B. Out-of-Band Intermodulation

The weakest signal, with power P_{sig}, to be detected in the presence of interferers, having powers P_{int}, at $f_0+\Delta f$ and $f_0+2\Delta f$ leads to requirements for intermodulation performance. Typically, this is specified with the minimum SIR ($\text{SIR}_{\min}$) that the filter needs to satisfy in its output in order to meet the overall system carrier-to-interference (C/I) ratio target. Requiring that the SIR be greater than or equal to the minimum $\text{SIR}_{\min}$ gives from (9)

$$d^3 + (\epsilon_0 A\omega_0 R_{\text{ac}})^2 d \geq \frac{\epsilon_0 A R_{\text{ac}}}{m}\frac{5P_{\text{int}}\sqrt{P_{\text{int}}}\text{SIR}_{\min}}{8|\Delta\omega|\omega_0\sqrt{P_{\text{sig}}}}, \tag{14}$$

which is also valid for higher-order filters as shown in Section II. Result (14) is easily derived after noting that both ω_e and R'_S in (9) are functions of the gap. If $R'_S \approx R_{\text{ac}} \Leftrightarrow (R_{\text{ac}}\omega_0 C_0)^2 \ll 1$, (14) simplifies to

$$d \geq \left(\frac{\epsilon_0 A R_{\text{ac}}}{m}\frac{5P_{\text{int}}\sqrt{P_{\text{int}}}\text{SIR}_{\min}}{8|\Delta\omega|\omega_0\sqrt{P_{\text{sig}}}}\right)^{1/3}. \tag{15}$$

Eq. (14) and (15) show that to meet the performance requirements given as $\text{SIR}_{\min}$, there is a minimum for the gap.

C. In-Band Loss

Requiring that the passband voltage gain G_V, given by (12), be greater than a minimum gain $G_{\min}$, set by the insertion loss specifications, gives

$$QV_{\text{bias}}^2 \geq \frac{nd^4\sqrt{km}}{(\epsilon_0 A)^2\left\{\frac{2}{\omega_0 C'_L G_{\min}}\frac{|1+j\omega_0 C'_L R'_L|}{|1+j\omega_0 C_0 R_{\text{ac}}|} - R'_S - R'_L\right\}}. \tag{16}$$

Thus, once the gap d is chosen, the unloaded quality factor Q and the bias voltage V_{bias} need to be chosen to meet the insertion loss specifications. As the unloaded quality factor is usually determined by material properties, effectively this gives a requirement for the bias voltage.

D. In-Band Intermodulation

The in-band intermodulation is estimated from (11) by considering 1) the signal self distortion, and 2) in-band interferers. However, typically the out-of-band interferers give more stringent linearity requirements. Therefore, after choosing the filter parameters, it is usually sufficient to check that the filter meets the in-band specifications. If these are not met, then the filter gap should be increased and the design adjusted accordingly.

TABLE IV
SIMPLIFIED FILTER REQUIREMENTS FOR GSM 900 [15].

Specification		Comment
$\mathrm{SIR}_{\min}$	9 dB	(9) ⇒ (14), full rate speech
$G_{\min}$	−3 dB	(12) ⇒ (16), in-band loss
$A_{\min}(f - f_0 = 10\ \mathrm{MHz})$	23 dB	(13), minimum selectivity
to be met with :		
P_{sig}	−99 dBm	Signal
$P_{\mathrm{int}}(\Delta f = 0\ \mathrm{Hz})$	−49 dBm	In-band interferer
$P_{\mathrm{int}}(\Delta f = 10\ \mathrm{MHz})$	0 dBm	Out-of-band interferer

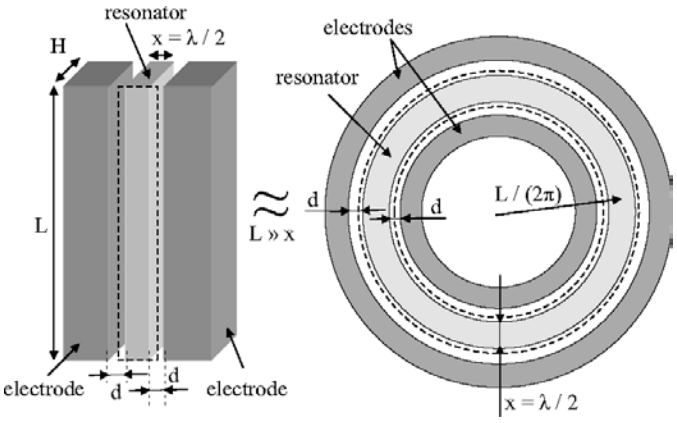

Fig. 4. Test geometry for resonator design showing the resonator surrounded by the electrodes. The dotted line indicates the vibration mode shape in the extended state.

V. GSM 900 Filter Design Example

In the following, the usage of the design equations of Section IV is illustrated by a single-stage MEMS front-end filter design for $f_0 = 1$ GHz with the requirements of the GSM 900 mobile device. The simplified requirements are shown in Table IV. These specifications should be considered as exemplary performance requirements and a realistic system design may set more or less stringent goals.

A. Resonator Geometry

Let us now, as a simple example, consider a bar geometry shown in Fig. 4. The resonating dimension is $x = \lambda/2 = v/(2f_0) \approx 4\ \mu$m for $f_0 = 1$ GHz. Here $v = \sqrt{Y/\rho}$ is the bulk acoustic wave velocity with $\rho = 2330\ \mathrm{kg/m^3}$ the density and $Y = 168$ GPa the Young's modulus of silicon. This simple geometry can also approximate the ring geometry [17], shown at the right-hand side of Fig. 4, when the ring radius $L/(2\pi)$ is much larger than the ring width x. The capacitive transducers at both sides of the resonator have an area of $A = HL$ and rest capacitance of $C_0 = \epsilon_0 HL/d$, where d is the gap. The effective mass and spring coefficient are now [18]

$$m = \rho L x H/2, \tag{17}$$

$$k = \pi^2 Y L H/(2x). \tag{18}$$

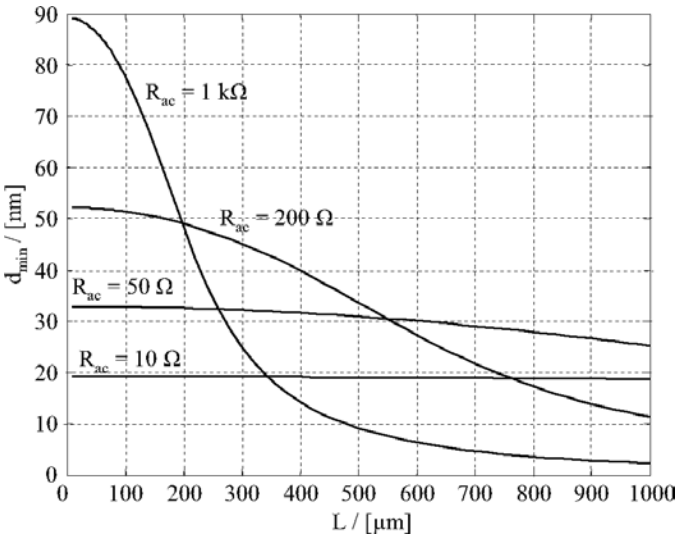

Fig. 5. Minimum gap (14), determined by the maximum out-of-band intermodulation, for the resonators of Fig. 4 with $H = 10\ \mu$m.

B. Minimum Quality Factor

From the minimum interference attenuation requirements in Table IV, one obtains (13) $Q' = 700$ for the minimum loaded quality factor. For channel-select filtering, the passband is 200 kHz, corresponding to a much higher in-circuit quality factor of $Q' = 5000$, which would also be enough for $A_{\min} = 40$ dB at 10 MHz off the passband in (13), as typically satisfied by commercial FBAR filters.

C. Minimum Gap (Linearity)

Given the resonator geometry, the minimum gap $d_{\min}$ is solved from (14). Fig. 5 shows the minimum gap for $R_{\mathrm{ac}} \in \{10, 50, 200, 1000\}\ \Omega$ as a function of the transducer length L with $H = 10\ \mu$m. For small L, (15) is a good approximation and gives, for example, $d_{\min} = 19$ nm and $d_{\min} = 33$ nm for $R_{\mathrm{ac}} = 10\ \Omega$ and $R_{\mathrm{ac}} = 50\ \Omega$, respectively. With increasing L, the effect of increasing C_0 requires the use of (14). As Fig. 5 illustrates, the minimum gap $d_{\min}$ increases with increasing source impedance R_{ac}. This is due to increase in source voltage level V_{ac} for given source power.

D. Minimum QV_{bias}^2 (Insertion Loss)

We now set the gap close to its minimum value for the resonators of Fig. 5, say, $d(L) = d_{\min} + 3$ nm, after which C_0 and the other needed parameters are determined in order to calculate the minimum value for QV_{bias}^2 in (16). In what follows, two architectures are considered: 1) the conventional resistive termination, and 2) an integrated filter where the filter output is directly connected to a capacitive FET LNA load while the filter input is fed from a resistive source such as an antenna.

Fig. 6 shows the calculated minimum QV_{bias}^2 for three different loads: a resistive load and two different capacitive

loads. Note that in Fig. 6, the $d(L) = d_{\min} + 3$ depends on the resonator length L and is obtained from Fig. 5. The central challenge in MEMS filter design for portable low-voltage devices, namely, very high QV_{bias}^2, is clearly illustrated. To calculate the actual filter parameters, we assume $Q = 5000$ and $H = 10$ μm. Table V summarizes the selected filter designs that are indicated in Fig. 6 with circles and labels (A) and (B). All designs of Table V, except the one with a 1-kΩ resistive load, satisfy the requirements in Table IV. For the resistive 1-kΩ load, the loaded quality factor is too low for (9) to be a good approximation for the SIR. A solution would be to correct the design by requiring a somewhat higher $\text{SIR}_{\min}$. It is also seen that with the resistive load quite a large resonator size and a small electrode gap are needed.

As is evident from (12), terminating the resonator with a capacitive load enables voltage gain as the resonator RLC circuit is effectively tapped. Consequently, a capacitive load of $C_L = 1$ pF corresponding to a typical LNA FET input, would allow a more realistic filter size. With an even higher load impedance of $C_L = 0.1$ pF, the filter could be realized at $V_{\text{bias}} < 5$ V.

In Fig. 6, it was assumed for the gap that $d = d_{\min} + 3$ nm corresponding to the minimum gap $d_{\min}$ of Fig. 5. If the minimum achievable gap is determined by the fabrication process, Figs. 7 and 8 may be used to determine the minimum QV_{bias}^2 for capacitive and resistive loads, respectively. It is seen that for a fixed gap, there is an optimal resonator size resulting in the lowest QV_{bias}^2. For a capacitive load (see Fig. 7), a smaller source impedance R_{ac} results in smaller QV_{bias}^2 as larger impedances load the resonator more and thus reduce the attainable voltage gain from the resonator. The opposite holds for resistively terminated resonators as shown in Fig. 8. That is, for a resistive load with fixed gap, the source and load impedances should be large in comparison to R_{em} to minimize the insertion loss.

E. In-Band Linearity Check

For the in-band interference with $P_{\text{int}} = -49$ dBm [15] and a signal with $P_{\text{sig}} = -99$ dBm, (10) with a minimum SIR of 9 dB gives the requirement of

$$P_{\text{IIP}}^{\text{IB}} \geq -19.5 \text{ dBm} \equiv P_{\text{IIP,min}}^{\text{IB}}, \tag{19}$$

where $P_{\text{IIP}}^{\text{IB}}$ is given by (11). As shown in Table V, all designs satisfy the in-band linearity requirement.

VI. Conclusions

In this paper, the capacitive MEMS filter design was analyzed and the trade-off between linearity and insertion loss was qualified. For simplicity, a single-stage filter was considered and it was assumed that several filters would be in parallel to cover the entire RX band. For GSM, this would require more than ten filters which may be impractical. However, as the SIR analysis was shown to be valid

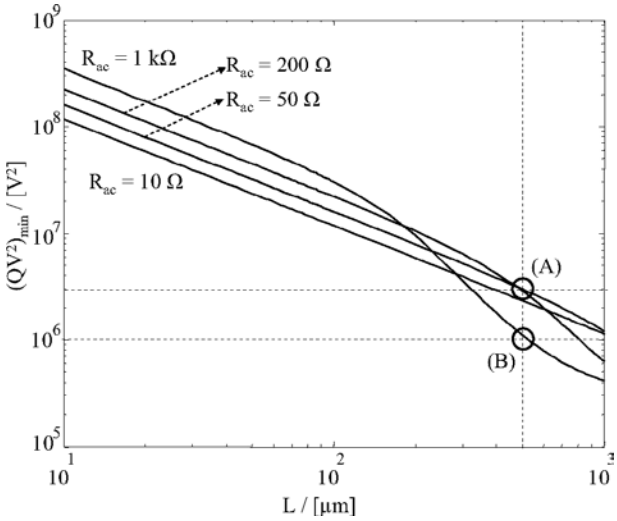

(a)

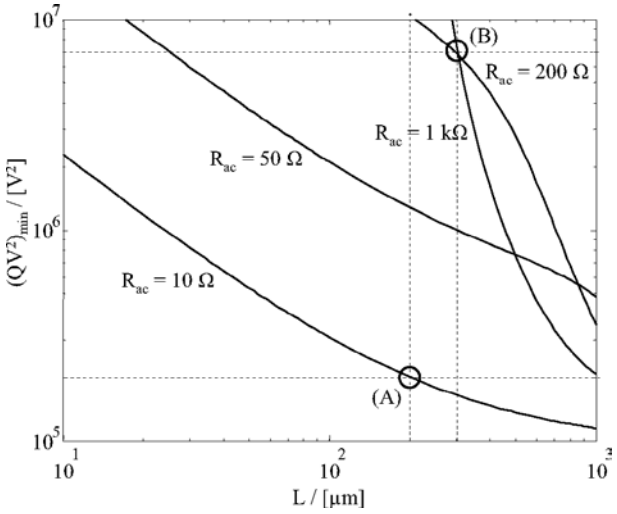

(b)

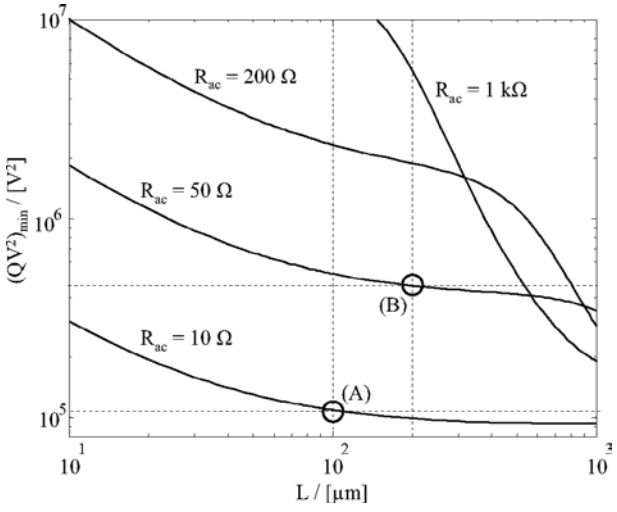

(c)

Fig. 6. Minimums of QV_{bias}^2 (16), determined by the maximum in-band loss of the filter, corresponding to the resonator geometries of Fig. 5 with $d(L) = d_{\min} + 3$ nm. The circles labeled (A) and (B) correspond to the designs of Table V. (a) Resistive load ($C_L = 0$, $R_L = R_{\text{ac}}$); (b) capacitive load ($C_L = 1$ pF, $R_L = 1$ MΩ); (c) capacitive load ($C_L = 0.1$ pF, $R_L = 1$ MΩ).

TABLE V
GSM 900 FILTER DESIGNS* INDICATED WITH CIRCLES IN FIG. 6.

Load impedance in Fig. 6	Selected case in Fig. 6	R_{ac} [Ω]	L [μm]	d [nm]	V_{bias} [V]	R_{em} [Ω]	Q' Eq. (1)	SIR Eq. (9) [dB]	SIR [10] $\Delta f < 0$ [dB]	SIR [10] $\Delta f < 0$ [dB]	P_{IIP}^{IB} Eq. (11) [dBm]	G_V Eq. (12) [dB]
Resistive load	(A)	200	500	37	24	52	1500	10	11	9.7	34	−3
Fig. 6(a)	(B)	1k	500	12	15	1.5	1400	11	17	5.6	15	−2.9
Capacitive load	(A)	10	200	22	**6.4**	230	4800	13	13	12	30	−2.6
1 pF, Fig. 6(b)	(B)	200	300	48	37	102	2200	10	11	9.6	29	−3
Capacitive load	(A)	10	100	22	**4.7**	841	4900	13	13	12	33	−2.6
0.1 pF, Fig. 6(c)	(B)	50	200	36	9.8	690	4700	12	12	11	33	−2.9

*In all designs $H = 10$ μm and $Q = 5000$.

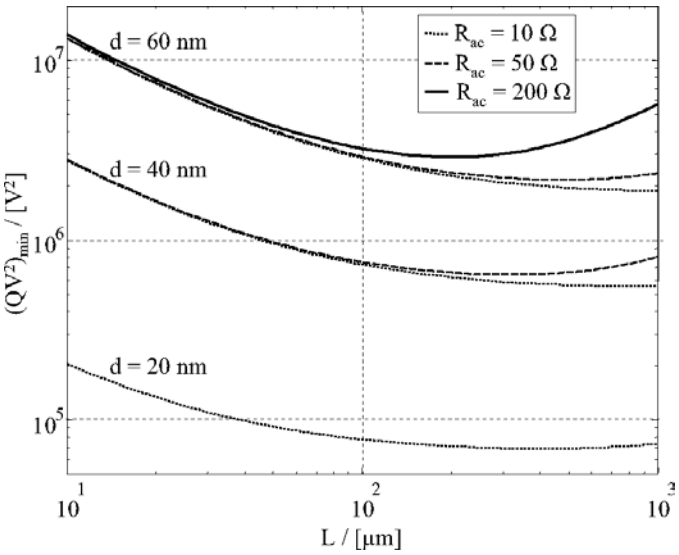

Fig. 7. Minimum of QV_{bias}^2, for a filter with capacitive load (C_L = 0.1 pF, $R_L = 1$ MΩ), and fixed gap sizes of $d \in \{20, 40, 60\}$ nm.

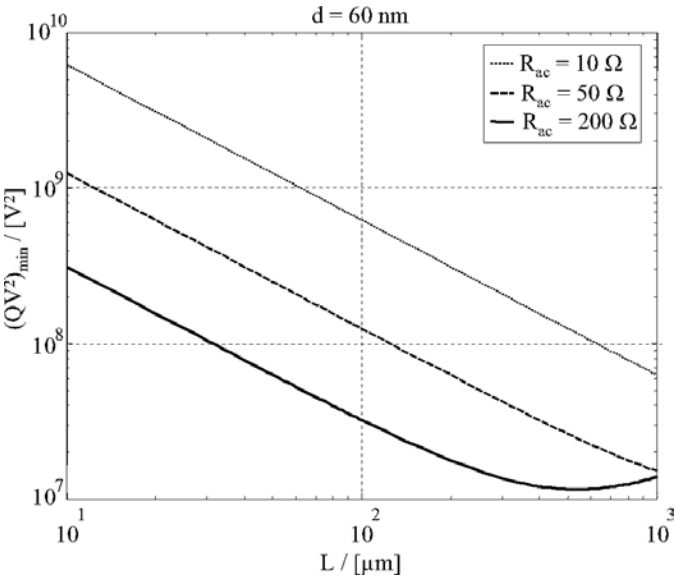

Fig. 8. Minimum of QV_{bias}^2, for a filter resistive load ($R_L = R_{ac}$) and a fixed gap size of $d = 60$ nm.

also for multi-stage filters, the conclusions also hold for higher-order pass-band filter designs. What is different for higher-order filters is that the losses in each stage add up and, consequently, the motional resistance has to be even lower than for the single-stage designs.

After the analysis, a systematic procedure to design MEMS band-pass filters was formulated. It was found desirable to utilize the high resonator quality factor for voltage gain that is enabled by capacitive load termination at the output of the filter. This is possible in integrated receiver architectures, where 50-Ω transmission lines are not needed between the antenna and the filter and between the filter and the LNA.

Using dielectric other than air/vacuum for the electrode gap has potential in lowering the electrical impedance, thus alleviating the need for a very narrow gap [19]. The analysis procedure derived in this paper can be directly applied for such devices as long as an appropriate value for permittivity is used.

The analysis in this paper was mainly theoretical and only few references were made to manufacturing where several challenges remain: 1) The gap should be reduced below 30 nm to enable bias voltages of the order of 5 V; 2) The dimensional tolerances of the filters, manufactured with lithography, are poor, leading to wide variations in center frequency; 3) The parasitic feed through capacitance may limit the filtering performance, and differential readout may be required. If these challenges are addressed, MEMS filters can have a large economic potential.

REFERENCES

[1] H. C. Nathansona, W. E. Newell, R. A. Wickstrom, and J. R. Davis, "The resonant gate transistor," *IEEE Trans. Electron Devices*, vol. 14, no. 2, pp. 117–133, Mar. 1967.

[2] C. T.-C. Nguyen and R. T. Howe, "CMOS micromechanical resonator oscillator," in *Tech. Dig. IEEE Int. Electron Devices Meeting*, Washington, DC, 5–8 Dec. 1993, pp. 199–202.

[3] H. Tilmans, "Equivalent circuit representation of electromechanical transducers: I. Lumped-parameter systems," *J. Micromech. Microeng.*, vol. 6, no. 1, pp. 157–176, Mar. 1996.

[4] L. Lin, R. T. Howe, and A. P. Pisano, "Microelectromechanical filters for signal processing," *J. Microelectromech. Syst.*, vol. 7, no. 3, pp. 286–294, Sep. 1998.

[5] C. T.-C. Nguyen, "Frequency-selective MEMS for miniaturized low-power communication devices," *IEEE Trans. Microwave Theory Tech.*, vol. 47, no. 8, pp. 1486–1503, Aug. 1999.

[6] V. Kaajakari, T. Mattila, A. Oja, J. Kiihamäki, and H. Seppä, "Square-extensional mode single-crystal silicon micromechanical resonator for low phase noise oscillator applications," *IEEE Electron Device Lett.*, vol. 25, no. 4, pp. 173–175, Apr. 2004.

[7] J. Wang, Z. Ren, and C. T.-C. Nguyen, "1.156-GHz self-aligned vinrating micromechanical disk resonator," *IEEE Trans. Ultrason., Ferroelect., Freq. Contr.*, vol. 51, no. 12, pp. 1607–1628, Dec. 2004.

[8] R. Navid, J. R. Clark, M. Demirci, and C. T.-C. Nguyen, "Third-order intermodulation distortion in capacitively-driven cc-beam micromechanical resonators," in *Tech. Dig. Int. IEEE Microelectromechanical Syst. Conf.*, Interlaken, Switzerland, 21–25 Jan. 2001, pp. 228–231.

[9] A. T. Alastalo and V. Kaajakari, "Intermodulation in capacitively coupled microelectromechanical filters," *IEEE Electron Device Lett.*, vol. 26, no. 5, pp. 289–291, May 2005.

[10] A. T. Alastalo and V. Kaajakari, "Third-order intermodulation in microelectromechanical filters coupled with capacitive transducers," *J. Microelectromech. Syst.*, vol. 15, no. 1, pp. 141–148, Feb. 2005.

[11] A. T. Alastalo and V. Kaajakari, "Designing capacitively coupled microelectromechanical filters," in *Proc. IEEE Ultrason. Symp.*, Rotterdam, The Netherlands, 18–21 Sep. 2005, pp. 1588–1591.

[12] S. Pourkamali and F. Ayazi, "Electrically coupled MEMS bandpass filters: Part I: With coupling element," *Sens. Actuators A*, vol. 122, no. 2, pp. 307–316, Aug. 2005.

[13] Aplac RF Design Tool, APLAC An AWR Company, www.aplac.com.

[14] T. Veijola and T. Mattila, "Modeling of nonlinear micromechanical resonators and their simulation with the harmonic-balance method," *Int. J. RF Microwave Computer-Aided Eng.*, vol. 11, no. 5, pp. 310–321, Sep. 2001.

[15] European Telecommunications Standards Institute (ETSI), "GSM global system for mobile communications, 3GPP TS 05.01/05.05," 2003.

[16] T. Ranta, J. Ellä, and H. Pohjonen, "Antenna switch linearity requirements for GSM/WCDMA mobile phone front-ends," in *8th Eur. Conf. Wireless Technol.*, Paris, France, 3–4 Oct. 2005, pp. 23–26.

[17] S.-S. Li, Y.-W. Lin, Y. Xie, Z. Ren, and C. T.-C. Nguyen, "Micromechanical 'hollow-disk' ring resonators," in *Tech. Dig. Int. IEEE Microelectromechanical Syst. Conf.*, Maastricht, The Netherlands, 25–29 Jan. 2001, pp. 821–824.

[18] T. Mattila, J. Kiihamäki, T. Lamminmäki, O. Jaakkola, P. Rantakari, A. Oja, H. Seppä, H. Kattelus, and I. Tittonen, "12 MHz micromechanical bulk acoustic mode oscillator," *Sens. Actuators A*, vol. 101, no. 1-2, pp. 1–9, Sep. 2002.

[19] S. A. Bhave and R. T. Howe, "Internal electrostatic transduction for bulk-mode MEMS resonators," in *Solid State Sensor, Actuator and Microsystems Workshop (Hilton Head 2004)*, Hilton Head Island, SC, 6–10 June 2004, pp. 59–60.

Ari T. Alastalo received the M.Sc. degree in technical physics in 1997 from Helsinki University of Technology (HUT). From 1996 to 1998 he was an assistant at HUT working in the area of magnetic quantum impurities. From 1998 to 2001 he was with Nokia Research Center carrying out research of radio propagation, RF architectures, baseband algorithms and protocols for adaptive-antenna systems. Since 2002 he has been a Research Scientist at VTT. His present research focuses on RF MEMS.

Ville Kaajakari received his M.S. and Ph.D. degrees in electrical and computer engineering from University of Wisconsin-Madison in 2001 and 2002, respectively. He is currently Senior Research Scientist at VTT Information Technology, Finland, where his research interest is RF-MEMS.

PUBLICATION IV

Analysis of a MEMS Transmission Line

In: IEEE Transactions on Microwave Theory and Techniques 2003. Vol. 51, No. 8, pp. 1977–1981.
Reprinted with permission from the publisher.

Analysis of a MEMS Transmission Line

Ari T. Alastalo, Tomi Mattila, *Member, IEEE*, and Heikki Seppä

***Abstract*—A microelectromechanical system (MEMS) sound waveguide is considered as a transmission line for RF signals. We analyze a device geometry of a straight one-dimensional microsize silicon rod, where a longitudinal acoustic wave is generated and detected using capacitive transducers. Linear, isotropic, and nondispersive acoustic-wave propagation is assumed. Based on the calculation of the electromechanical impedance, an electrical equivalent model is derived for the acoustic transmission line. A numerical example and a comparison to measured properties of a MEMS–transmission-line resonator shows that the characteristic impedance level of the waveguide is typically high, which causes challenges for matched termination. Solutions to overcome the matching problems are discussed.**

***Index Terms*—Electromechanical coupling, microelectromechanical system (MEMS) devices, RF MEMS, transmission line, waveguide.**

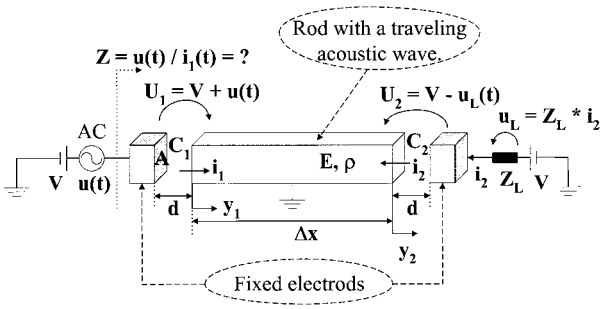

Fig. 1. Schematic representation of a setup where an electric signal is transmitted through a micromechanical rod as an acoustic plane longitudinal wave. Coupling between the electric signal and acoustic wave is done capacitively at both ends of the rod.

I. Introduction

ACOUSTIC-WAVE propagation in solids is an old and widely studied topic [1], [2]. Typical applications, such as delay lines, filters, and resonators, bear an analogy with the microwave electromagnetic devices [1], [3]. Acoustic wave theory is extensively used e.g. in bulk acoustic-wave (BAW) resonators and surface acoustic-wave (SAW) filters [3], [4]. The recent advances in microelectromechanical system (MEMS) technology have opened the possibility for creating miniaturized acoustical devices. As an example, a micromechanical resonator based on BAW operation has been demonstrated to be well suited for creating a high spectral purity oscillator [5]. Integrability with CMOS electronics, as well as size reduction and power savings of MEMS components compared to off-chip solutions (such as SAW devices) facilitate design of efficient single-chip radio transceivers that could revolutionize wireless communication devices [6]–[8].

In this paper, we investigate the possibility of creating microacoustical components, such as delay lines, for RF signals. We focus on a typical device geometry of a straight one-dimensional microsize silicon rod, where a longitudinal acoustic wave is generated and detected using capacitive transducers. Linear, isotropic, and nondispersive acoustic-wave propagation is assumed.[1] Based on the calculation of the electromechanical impedance, an electrical equivalent model is derived for the acoustic transmission line. The acoustic reflection and voltage transmission at the receiving transducer are evaluated using typical values for electrostatic coupling. The results show that obtaining perfect nonreflecting termination for the microsize transmission line is not straightforward, but requires tailored impedance-transforming techniques.

Manuscript received December 19, 2002; revised February 27, 2003.

The authors are with VTT Information Technology, Microsensing, Espoo FIN-02044 VTT, Finland (e-mail: ari.alastalo@vtt.fi).

Digital Object Identifier 10.1109/TMTT.2003.815270

[1]For a review of nonlinear and dispersive one-dimensional models see, e.g., [9] and the references therein.

II. Electromechanical Modeling

The setup that we are considering is schematically illustrated in Fig. 1. An electric signal is capacitively coupled to and from the MEMS rod at both ends through fixed electrodes. The rod is allowed to vibrate longitudinally between the electrodes to enable wave propagation along the rod. The rod is assumed to be anchored to the surrounding structures such that the wave propagation is not notably disturbed. In practice, the circuitry to connect the bias and signal voltages, as well as the shape of the electrodes and other details can differ from the simplified system of Fig. 1, which, however, captures the relevant physical properties. Some generalizations, e.g., for nonsymmetric bias, will be discussed after analyzing the system of Fig. 1. The electrodes and waveguide can be fabricated, e.g., on a device layer of a silicon-on-insulator (SOI) wafer. To reduce dissipation caused by air friction to moving MEMS structures, the device can be packaged in a vacuum.

In Fig. 1, V is a constant bias voltage applied to the electrodes at both ends of the rod and $u(t)$ is a time-dependent signal voltage at the left (input) electrode. The signal is taken to be harmonic $u(t) = u_0 \exp(j\omega t)$. The signal voltage $u(t)$ induces currents $i_1(t)$ and $i_2(t)$ through the input (left-hand side) and output (right-hand side) transducer capacitors C_1 and C_2, respectively. Consequently, voltage across the load impedance Z_L is $u_L(t) = Z_L i_2(t)$. Since the rod is grounded, voltages $U_1(t) = V + u(t)$ and $U_2(t) = V - u_L(t)$ are seen across the transducer capacitors. The rod has a length Δx, a constant

0018-9480/03$17.00 © 2003 IEEE

cross-sectional area A, Young's modulus E, density ρ, and is assumed to have no mechanical[2] or electrical[3] losses. When no voltages are applied ($U_1 = U_2 = 0$), the gap between the rod and electrodes is d at both ends. With nonzero voltages, the ends of the rod are displaced by y_1 and y_2, as shown in Fig. 1. We assume the transducer capacitors to be ideal parallel-plate capacitors with capacitances $C_1 = \epsilon_0 A/(d + y_1)$ and $C_2 = \epsilon_0 A/(d - y_2)$. The voltages across and currents through the capacitors are thus related by $i_1 = d(C_1 U_1)/dt$ and $i_2 = d(C_2 U_2)/dt$. We further assume that the voltage sources are ideal with no internal losses. The electric input impedance is now $Z = u(t)/i_1(t)$.

We assume that the voltages $u(t)$ and $u_L(t)$ are small with respect to the bias voltage V and that the displacements y_1 and y_2 are much smaller than the zero-voltage gap d. We also assume the system to be linear. Expanding the currents i_1 and i_2 up to linear order in the small parameters (u/V), (u_L/V), (y_1/d), and (y_2/d), we obtain

$$i_1 = j\omega C_0 u - \eta \dot{y}_1 \tag{1a}$$

$$i_2 = \frac{\eta \dot{y}_2}{1 + j\omega C_0 Z_L}. \tag{1b}$$

Here, $C_0 \equiv \epsilon_0 A/d$ is the zero-voltage capacitance and $\eta \equiv C_0 V/d$ is the electromechanical coupling constant. For vanishing mechanical motion, the electric input impedance is from (1a) $Z = Z_0 \equiv 1/(j\omega C_0)$.

For the forces f_1 and f_2 exerted by the capacitors C_1 and C_2 to the left- and right-hand-side ends of the rod, respectively, one finds through $f = (1/2)U^2 dC/dy$ up to linear order

$$f_1 = \eta\left(\frac{V}{2} + u\right) - k_e y_1 \tag{2a}$$

$$f_2 = \frac{\eta V}{2} + k_e y_2 - \gamma \dot{y}_2 \tag{2b}$$

where $k_e \equiv V\eta/d$ is the electrical spring-softening term and $\gamma \equiv \eta^2 (Z_L || Z_0)$ (Z_L and Z_0 in parallel) is a complex damping coefficient. Here, the sign of f_1 is selected as shown in Fig. 2. k_e usually represents only a small correction and can be omitted.

The mechanical model is now as follows. The longitudinal displacement field $y(x,t)$ of the rod obeys a wave equation

$$\frac{\partial^2 y(x,t)}{\partial t^2} = c^2 \frac{\partial^2 y(x,t)}{\partial x^2}, \qquad t \geq 0; \quad x \in [0, \Delta x] \tag{3}$$

with boundary conditions following from (2a) and (2b) assuming Hooke's law to be valid:

$$\left.\frac{\partial y(x,t)}{\partial x}\right|_{x=0} = \frac{f_1}{AE} \qquad \left.\frac{\partial y(x,t)}{\partial x}\right|_{x=\Delta x} = \frac{f_2}{AE} \tag{4}$$

and has a harmonic time dependence due to the harmonic force. Here, $c \equiv \sqrt{E/\rho}$ is the phase velocity of the longitudinal wave. The mechanical model is illustrated in Fig. 2.

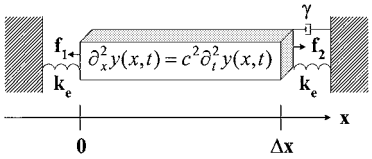

Fig. 2. Mechanical equivalent model of the setup of Fig. 1. Here, $\partial_x^2 y$ and $\partial_t^2 y$ are shorthand notations for the second-order space and time derivatives of the displacement field, respectively.

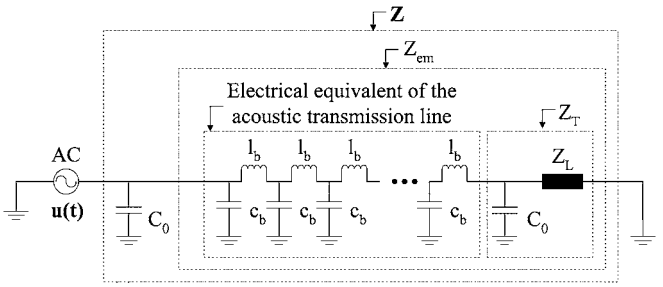

Fig. 3. Electrical small-signal equivalent model of Fig. 1.

III. Analytical Solution

A solution to the wave-propagation problem of (3) and (4) is found by subtracting a time-independent zero-signal solution $y_0(x)$ from the displacement field $y(x,t)$ and seeking a solution in the form

$$\bar{y}(x,t) = \left(Be^{((j\omega x)/c)} + De^{((-j\omega x)/c)}\right) e^{j\omega t} \tag{5}$$

for the deviation $\bar{y}(x,t) \equiv y(x,t) - y_0(x)$, which also satisfies the wave equation (3) and a zero-bias form of the boundary conditions (4). For the current i_1 in (1a) through the input capacitor C_1, we find

$$i_1(t) = j\omega C_0 u(t) - \eta \dot{\bar{y}}(0,t) = \frac{u(t)}{Z} \equiv u(t)\left(\frac{1}{Z_0} + \frac{1}{Z_{\rm em}}\right) \tag{6}$$

where the electromechanical impedance (see Fig. 3)

$$Z_{\rm em} \equiv \frac{j u_0}{\eta\omega(B + D)} \tag{7}$$

[2]We assume that despite doping and imperfections, acoustic properties of the SOI device layer material can be approximated by those of single-crystal silicon within the frequency range of interest. At $f = 10$ MHz, for longitudinal plane-wave propagation in cube-edge direction in single-crystal bulk silicon, one has an attenuation factor of $\alpha \approx 10^{-4}$ dB/mm $\propto f^2$ [1]. This corresponds to an acoustical quality factor of $Q \approx 3.3 \times 10^5 \propto 1/f$ [1]. An electrical equivalent resistance R_s, of the mechanical dissipation over a distance of 1 mm, in series with a load resistance R_L is found by voltage division to be $R_s = R_L(10^{\alpha \times 1\ \mathrm{mm}/20} - 1)$. For $\alpha = 10^{-4}$ dB/mm at $f = 10$ MHz, we find $R_s = R_L \times 10^{-5}$. For longitudinal wave propagation in a micromechanical narrow rod, a quality factor of $Q \approx 1.8 \times 10^5$ has been reported [5], which is only half of the bulk value above and yields a doubling of α and R_s. Thus, at least for frequencies in the range of 10 MHz, mechanical losses can be neglected for small systems.

[3]In practice, one places electrical ground connections closer to the ends of the rod and not only in the middle, as shown in Fig. 1, for simplicity. This is in order to reduce dissipation caused by nonzero resistivity r_b of the rod material. Groundings can be done in places where the rod is hanged to the surrounding structures. Details of hanging are not studied in this paper. Resistance at the ends of the rod can be calculated as $R_b = r_b l_g/A$, where l_g is the distance from the end of the rod to the closest grounding and A is the cross-sectional area of the rod. For the heavily boron-doped material of [5] ($r_b \approx 2 \times 10^{-4}\ \Omega$m [14]), with $l_b = 100\,\mu$m and $A = 100\,\mu\mathrm{m} \times 10\,\mu$m, one finds $R_b \approx 20\ \Omega$, which, as will be seen, is much smaller than other typical impedances of the system and will be ignored in this paper. If taken into account, R_b becomes in series with the capacitances C_0 in Fig. 3.

expresses the coupling of the electric signal to the mechanical motion and is, thus, the quantity of primary interest here. Substituting (5) to the boundary conditions (4) with zero bias allows one to solve for the unknown coefficients B and D and to obtain $Z_{\rm em}$ in (7). For simplicity, we only consider the case where $k_e = 0$, which generally is a good approximation for practical MEMS structures. Consequently, one obtains the standard expression [2], [10], [11]

$$Z_{\rm em} = Z_b \frac{Z_T + Z_b \tanh(j\beta\Delta x)}{Z_b + Z_T \tanh(j\beta\Delta x)} \tag{8}$$

where $\beta \equiv \omega/c$, $Z_b \equiv AE/(c\eta^2)$, and $Z_T \equiv Z_0 || Z_L$ (see Fig. 3). The mechanical losses can be included in (8) by substituting $j\beta$ with $j\beta + \alpha$, where α is the attenuation coefficient [1], [10], [11].

The mechanical amplitude reflection coefficient for the right-hand-side end of the rod can be expressed as

$$r^2 \equiv \left|\frac{B}{D}\right|^2 = \left|\frac{Z_T - Z_b}{Z_T + Z_b}\right|^2. \tag{9}$$

For zero reflection, one needs $Z_T = Z_b$, which gives with (8)

$$Z_{\rm em} = Z_b = \frac{AE}{c\eta^2} = \frac{A\sqrt{\rho E}}{\eta^2} = \frac{d^4\sqrt{\rho E}}{A(\epsilon_0 V)^2} \equiv R_{\rm em}. \tag{10}$$

Here, $Z_c \equiv A\sqrt{\rho E}$ is the mechanical characteristic impedance of the rod [2]. The corresponding matched load impedance is $Z_L = (R_{\rm em} || Z_0^*)$. The above discussion shows that $Z_b = Z_c/\eta^2$ can be seen as an electrical characteristic impedance of the acoustic waveguide. One can thus relate the inductance l_b and capacitance c_b densities in Fig. 3 to Z_b and to the phase velocity c through $Z_b = \sqrt{l_b/c_b}$ and $c = 1/\sqrt{l_b c_b}$. One finds $l_b = A\rho/\eta^2$, and $c_b = \eta^2/(AE)$ that are similar to the corresponding relations known for MEMS resonators [5].

Of interest are also the current i_2 in (1b) through the output capacitor and the voltage $u_L = Z_L i_2$ across the load impedance. The transfer impedance $Z_{12} \equiv u(t)/i_2(t)$ is found similarly to the input-impedance calculation above as follows:

$$Z_{12} = \frac{-ju_0\left(1 + \dfrac{Z_L}{Z_0}\right)}{\omega\eta\left(Be^{((j\omega\Delta x)/c)} + De^{-((j\omega\Delta x)/c)}\right)} \tag{11}$$

and gives the load voltage through $u_L = i_2 Z_L = u\, Z_L/Z_{12}$. In particular, for the matched load, one finds

$$u_L = u\big(-\cos(\beta\Delta x) + j\sin(\beta\Delta x)\big) = -ue^{-((j\omega\Delta x)/c)} \tag{12}$$

in which case, the acoustic waveguide only introduces a sign change and a phase shift to the electric signal and delivers a power of $|u|^2/(2Z_b)$ to the load.

If the matched load is represented by an inductance[4] of $L_{\rm em} \equiv 1/(\omega_0^2 C_0)$ in parallel with a resistance of $R_{\rm em}$, transmission through the line becomes bandpass centered at ω_0 with a 3-dB bandwidth of $W_{\rm 3dB} \equiv 1/(2\pi R_{\rm em} C_0)$. Due to the reactances in the system, it is now possible that the load voltage u_L exceeds the source voltage u. This can be prevented by requiring $\cos(\omega_0\Delta x/c) = 0 \Rightarrow \Delta x = \lambda/4 + n\lambda/2 (n \in \{0, 1, 2, \ldots\})$.

[4]Wide-band termination would require a reactance of $+j/(\omega C_0)$.

IV. Generalization of the System

More insight is gained by separating the problem into electrical and mechanical propagation. This is conveniently done by introducing transmission matrices. We take the mechanical equivalent of voltage u and current i to be negative of the force field $(-f)$ and the velocity field (v) in the waveguide. The mechanical impedance along the waveguide is now $Z_m \equiv -f/v$. The input (left-hand side) end current and force relations (1a) and (2a) now give

$$\begin{pmatrix} u \\ i_1 \end{pmatrix} = -\frac{1}{\eta_1}\begin{pmatrix} 1 & 0 \\ j\omega C_{0,1} & \eta_1^2 \end{pmatrix}\begin{pmatrix} -f_1 \\ v_1 \end{pmatrix} \equiv T_{\rm in}\begin{pmatrix} -f_1 \\ v_1 \end{pmatrix} \tag{13}$$

where $T_{\rm in}$ is the left-hand-side-end transmission matrix. Here, η_1 and $C_{0,1}$ denote η and C_0 at the input end. Similarly for the right-hand-side (output) end, one finds from (1b) and (2b)

$$\begin{pmatrix} -f_2 \\ v_2 \end{pmatrix} = -\frac{1}{\eta_2}\begin{pmatrix} \eta_2^2 & 0 \\ j\omega C_{0,2} & 1 \end{pmatrix}\begin{pmatrix} u_L \\ i_2 \end{pmatrix} \equiv T_{\rm out}\begin{pmatrix} u_L \\ i_2 \end{pmatrix} \tag{14}$$

with η_2 and $C_{0,2}$ denoting η and C_0 at the right-hand-side transducer. The mechanical propagation is given by the familiar waveguide transmission matrix

$$\begin{aligned}\begin{pmatrix} -f_1 \\ v_1 \end{pmatrix} &= \begin{pmatrix} \cos(\beta\Delta x) & jZ_c\sin(\beta\Delta x) \\ j\sin\dfrac{(\beta\Delta x)}{Z_c} & \cos(\beta\Delta x) \end{pmatrix}\begin{pmatrix} -f_2 \\ v_2 \end{pmatrix} \\ &\equiv T_{\rm mech} \times (-f_2, v_2)^T \end{aligned} \tag{15}$$

yielding for mechanical impedances the same result shown above in (8) for the electromechanical impedance (with interchanges $Z_{\rm em} \leftrightarrow Z_1$, $Z_T \leftrightarrow Z_2$, and $Z_b \leftrightarrow Z_c$). The electrical input impedance Z is now found using the total transmission matrix of the system $T_{\rm tot} \equiv T_{\rm in} T_{\rm mech} T_{\rm out}$ from $(u, i_1)^T = T_{\rm tot} \times (u_L, i_2)^T$.

The matrix formulation enables one to consider more general situations with, for example, nonsymmetric bias or transducer geometries. Also, other transducer coupling mechanisms can be considered. The formulation also applies to different waveguide geometries, e.g., with varying cross-sectional area, for which the transmission matrix can be formulated. Furthermore, anchoring effects can be taken into account.

V. Numerical Example

Table I shows η, C_0, resistance $R_{\rm em}$, inductance $L_{\rm em}$, and bandwidth $W_{\rm 3dB}$ at center frequency $f_0 = 10.573$ MHz for a 1-mm-long silicon rod ($E = 166.7$ GPa, $\rho = 2330$ kg/m^3 $\Rightarrow$ $c \approx 8458$ m/s [5]) with $A = 8\ \mu$m $\times$ $10\ \mu$m and $A = 8\ \mu$m $\times$ $100\ \mu$m (one of the dimensions is limited by the typical height of the device layer of the SOI wafer), and $V = 100$ V. The center frequency is selected to obey $\cos(\omega_0\Delta x/c) = 0$ (see discussion in Section III). We consider three different values for the gap d (reaching a controllable gap size of 0.1 μm has been demonstrated [12]). The values of Table I (such as $R_{\rm em} = 3\ M\Omega$ for $d = 0.1\ \mu m$ and $A = 8\ \mu$m $\times$ $100\ \mu$m) reveal that, for practical realization of the MEMS waveguide, impedance matching is a challenge. This is because the weakness of the capacitive coupling makes the characteristic electrical impedance of the waveguide extremely high.

TABLE I
PARAMETERS FOR MATCHED TERMINATION OF AN ACOUSTIC TRANSMISSION LINE AT $f = 10.573$ MHz

A \ d	1 μm	0.5μm	0.1μm	variable
8 × 10	0.07	0.28	7.1	η / [μFV/m]
8 × 100	0.7	2.8	71	
8 × 10	0.7	1.4	7.1	C_0 / [fF]
8 × 100	7	14	71	
8 × 10	310	20	0.030	$R_{\rm em}$ / [GΩ]
8 × 100	31	2	0.003	
8 × 10	320	160	32	$L_{\rm em}$ / [mH]
8 × 100	32	16	3.2	
8 × 10	0.72	5.7	720	$W_{\rm 3dB}$ / [kHz]
8 × 100	0.72	5.7	720	
μ m × μ m				

Equation (10) shows that $R_{\rm em}$ can be made smaller by having a smaller gap d, softer or sparser rod material (smaller E or ρ), a larger area A, higher permittivity material in the gap, or a higher bias voltage V. On the other hand, the maximum displacement of the end of the rod is limited by $y_{\max} < \xi d$, where $\xi \approx 0.3$, in order to avoid pull-in. Considering only the bias voltage V, it is easy to show that the requirement to avoid pull-in leads to a lower limit for $R_{\rm em}$ as follows:

$$R_{\rm em} > R_{\rm em}^{\rm min} \equiv \frac{\sqrt{\rho}}{AE^{(5/6)}} \left(\frac{V}{\epsilon_0}\right)^{(2/3)} \left(\frac{\Delta x}{0.6}\right)^{(4/3)}. \quad (16)$$

For example, in Table I, with $R_{\rm em} = 3$ MΩ, we have $R_{\rm em}^{\rm min} \approx 2.7$ MΩ for a 1-mm-long rod. Increasing now the bias voltage by a factor of ten, decreases $R_{\rm em}$ to 30 kΩ, but leads to $R_{\rm em}^{\rm min} > R_{\rm em}$, resulting in pull-in. Thus, both (10) and (16) must be taken into account. One candidate for a softer and sparser rod material is porous silicon. For example, for a porosity of 60%, the Young's modulus is reported to drop almost 90% of the value for nonporous material [13]. This would divide $R_{\rm em}$ by five, but also yield a four times larger $R_{\rm em}^{\rm min}$.

Fig. 4 shows the voltage ratio u_L/u and mechanical reflection coefficient r^2 when an inductor of $L_{\rm em} = 1/(\omega_0^2 C_0)$ is used to tune out the transducer capacitance. The solid curves are for a center frequency satisfying $\cos(\omega_0 \Delta x/c) = 0$, while, for the dashed curves, a slightly different frequency with $\cos(\omega_0 \Delta x/c) \neq 0$ is considered.

VI. COMPARISON TO EXPERIMENTS

The characteristic impedance of the MEMS transmission line can feasibly be probed in the short- or open-circuited resonator configuration [10], [11], when the quality factor Q of the resonator is sufficiently large. For example, for an open-circuited transmission-line resonator, the lumped-element values for an equivalent *RLC* series-resonant circuit are $R = r_b \Delta x/2$, $L = \pi Z_b/(4\omega_0)$, and $C = 1/(L\omega_0^2)$ [11]. Here, $\Delta x = \lambda_0/4$ is the length of the line, λ_0 is the wavelength corresponding to the resonant frequency ω_0, Z_b is the electrical characteristic impedance of the waveguide in (10), and r_b is the resistance per unit length of the line. The equivalent *RLC* circuit is valid in the vicinity of the resonant frequency. Since losses in the waveguide are not considered in this paper, resistance r_b is not shown in Fig. 3 in series with the inductance l_b. Measurements for such a high-Q MEMS transmission-line resonator were reported in [5] at 11.75 MHz corresponding to $\Delta x = 180$ μm. Other resonator dimensions and parameter values of [5] were the same as here in Table I with $d = 1$ μm and $A = 8$ μm × 10 μm. The parameter values for the equivalent *RLC* circuit were obtained through fitting the simulation results to the measured data. In particular, it was found in [5] that $C = 0.05$ aF and $L = 3.62$ kH. Using the results of this paper, one obtains $L = \pi Z_b/(4\omega_0) = 3.34$ kH and $C = 1/(L\omega_0^2) = 0.05$ aF, which are in good agreement with the measurement-based values of [5]. Direct experimental study of the transmission-line operation of the MEMS waveguide requires solution to the impedance-matching problem that is one of the focuses of future research in this area.

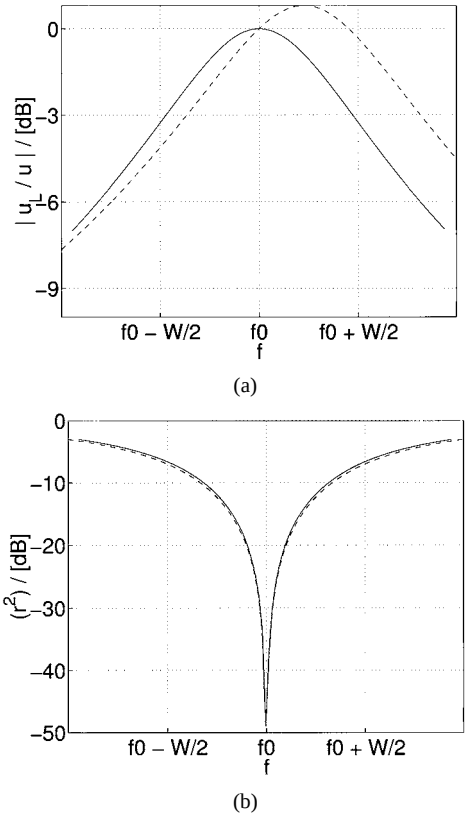

Fig. 4. (a) Voltage transmission $|u_L/u|$ and (b) mechanical reflection coefficient r^2 for center frequencies $f_0 = 10.573$ MHz (solid line) and $f_0 = 10$ MHz (dashed line). Other parameter values are the same as in Table I with the larger values of area and gap.

VII. DISCUSSION AND CONCLUSIONS

Using sound waveguides as delay lines for RF signals is desirable since much smaller group velocities can be reached than with electromagnetic waveguides. However, impedance levels needed for efficient signal transmission through an acoustic waveguide become extremely high, as shown in this paper, for a single-crystal silicon rod with capacitive coupling. This is due to the weakness of the electromechanical coupling constant. Thus, one needs to consider different coupling mechanisms, softer and sparser rod materials, electrical and mechanical impedance transformations, and other structures for acoustic-wave propagation. It is easy to show that, for example, with a microsize piezoelectric quartz transducer,

one does not reach a stronger coupling to a silicon rod when the length of the rod is much larger than the transducer size and when small enough capacitor gaps (of the order of half a micrometer) and high enough bias voltages (tens of volts) can be used. On the other hand, high-Q values of microelectromechanical resonators suggest that, at least for narrow bandwidths below 100 MHz, mechanical impedance transformation can enable efficient acoustic waveguide operation with capacitive coupling.

REFERENCES

[1] B. A. Auld, *Acoustic Fields and Waves in Solids*, 2nd ed. Melbourne, FL: Krieger, 1990, vol. 1.

[2] H. F. Pollard, *Sound Waves in Solids*. London, U.K.: Pion Ltd., 1977.

[3] J. F. Rosenbaum, *Bulk Acoustic Wave Theory and Devices*. Boston, MA: Artech House, 1988.

[4] D. P. Morgan, *Surface-Wave Devices for Signal Processing*. Amsterdam, The Netherlands: Elsevier, 1991.

[5] T. Mattila, J. Kiihamäki, T. Lamminmäki, O. Jaakkola, P. Rantakari, A. Oja, H. Seppä, H. Kattelus, and I. Tittonen, "A 12 MHz bulk acoustic micromechanical oscillator," *Sens. Actuators A, Phys.*, vol. 101, pp. 1–9, Sept. 2002.

[6] C. T.-C. Nguyen, "Frequency-selective MEMS for miniaturized low-power communication devices," *IEEE Trans. Microwave Theory Tech.*, vol. 47, pp. 1486–1503, Aug. 1999.

[7] D. F. Moore and R. R. A. Syms, "Recent developments in micromachined silicon," *Electron. Commun. Eng. J.*, vol. 11, no. 6, pp. 261–270, Dec. 1999.

[8] J. J. Yao, "RF MEMS from a device perspective," *J. Micromech. Microeng.*, vol. 10, pp. R9–R38, 2000.

[9] V. I. Erofeev and N. V. Klyueva, "Solitons and nonlinear periodic strain waves in rods, plates, and shells (a review)," *Acous. Phys.*, vol. 48, no. 6, pp. 643–655, 2002.

[10] D. M. Pozar, *Microwave Engineering*, 2nd ed. New York: Wiley, 1998.

[11] R. E. Collin, *Foundations for Microwave Engineering*. New York: McGraw-Hill, 1966.

[12] W.-T. Hsu, J. R. Clark, and C. T.-C. Nguyen, "A sub-micron capacitive gap process for multiple-metal-electrode lateral micromechanical resonators," in *Proc. IEEE MEMS Conf.*, Interlaken, Switzerland, 2001, pp. 349–352.

[13] D. Bellet, P. Lamagnère, A. Vincent, and Y. Brèchet, "Nanoindentation investigation of the Young's modulus of porous silicon," *J. Appl. Phys.*, vol. 80, no. 7, pp. 3772–3776, Oct. 1996.

[14] S. M. Sze, *Semiconductor Devices*, 2nd ed. New York: Wiley, 2002.

Ari T. Alastalo received the M.Sc. degree in technical physics from Helsinki University of Technology (HUT), Helsinki, Finland, in 1997.

From 1996 to 1998, he was an Assistant with HUT, where he was involved in the area of magnetic quantum impurities. From 1998 to 2001, he was with the Nokia Research Center, where he carried out research on radio propagation, RF architectures, baseband algorithms, and protocols for adaptive-antenna systems. Since 2002, he has been a Research Scientist with VTT Information Technology, Espoo, Finland. His current research focuses on RF MEMS.

Tomi Mattila (M'01) received the M.Sc. and Dr.Tech. degrees in technical physics from the Helsinki University of Technology (HUT), Helsinki, Finland, in 1994 and 1997, respectively.

From 1997 to 1999, he was a Post-Doctoral Research Fellow with National Renewable Energy Laboratory, Golden, CO. Since 1999, he has been a Senior Research Scientist with VTT Information Technology, Espoo, Finland. His current research interests concentrate on micromechanical RF devices.

Heikki Seppä received the M.Sc., Lic. Tech., and Dr. Tech. degrees in technology from the Helsinki University of Technology (HUT), Helsinki, Finland, in 1977, 1979 and 1989, respectively.

From 1976 to 1979, he was an Assistant with HUT, where he was involved in the area of electrical metrology. In 1979, he joined the Technical Research Centre of Finland (VTT), Espoo, Finland, where, since 1989, he has been a Research Professor. In 1994, he became Head of the measurement technology field with VTT, and in 1996–1998, he was Research Director of VTT automation. Since 2002, he has been the Research Director of VTT Information Technology. He has performed research, in general, on electrical metrology and, in particular, on superconducting devices for measurement applications. He also conducts research on dc superconducting quantum interference devices (SQUIDs), quantized Hall effect, mesoscopic devices, RF instruments, and MEMS devices.

PUBLICATION V

Micromechanical slow-velocity delay lines

In: Proc. 33rd European Microwave Conference, Münich, Germany, 6–10 October, 2003. Pp. 967–970.
Reprinted with permission from the publisher.

Micromechanical slow-velocity delay lines

Ari T Alastalo[1], Tomi Mattila[1], Heikki Seppä[1], James Dekker[2]

[1]VTT Information Technology, Microsensing, P.O. Box 1207, FIN-02044 VTT, Finland, Email: ari.alastalo@vtt.fi
[2]VTT Information Technology, Microelectronics, P.O. Box 1208, FIN-02044 VTT, Finland

***Abstract*— We consider a chain of coupled micromechanical resonators as a delay line for radio-frequency signals. Wave propagation in the chain is generated and detected using capacitive transducers. Analytical results, numerical simulations and rst measurements for the response of a prototype device are presented. The delay line is shown to have a bandpass response and a very low signal group velocity of the order of only few meters per second. Weaknesses of the rst prototypes are identi ed through simulations and a more optimal design is suggested.**

I. Introduction

Acoustic wave propagation in solids is an old and widely-studied topic. Typical applications, such as delay lines, filters and resonators, bear an analogy with the microwave electromagnetic devices [1]. Acoustic wave theory is extensively used e.g. in bulk-acoustic-wave (BAW) resonators and surface-acoustic-wave (SAW) filters. The recent advances in micro-electromechanical systems (MEMS) technology have opened the possibility for creating miniturised acoustical devices. As an example, a micromechanical resonator based on BAW-operation has been demonstrated to be well suited for creating a high spectral purity oscillator [2], [3]. Integrability with CMOS electronics as well as size reduction and power savings of MEMS components compared to off-chip solutions (such as SAW devices) facilitate design of efficient single-chip radio transceivers that could revolutionise wireless communication devices [4], [5].

In this paper we focus on a device geometry of a chain of coupled micromechanical resonators. Wave propagation along the chain is excited and detected using capacitive transducers. We present an analytical model for the device as well as numerical simulations and measurements for a first prototype device operating at 1.85MHz. The numerical simulations are done in Aplac® circuit simulator where both the mechanical resonators and the electronic circuitry of the measurement setup are modelled. It is shown, in particular, that reducing the feed-through capacitances to a minimum level is essential for good performance. Also dimensions of the resonator structures need to be carefully chosen, for example, to compensate for electrical spring softening introduced by the capacitive transducers. The first prototype device reported here does not reach sufficient performance but validates the analytical and numerical models. Improvements for the structure are suggested and will be concentrated on in future work. Furthemore, to reach higher frequencies the dimensions of the delay line need to be scaled down.

II. Prototype Delay Line

An IR spectroscope picture of a prototype spring-mass-chain delay-line structure is shown in Fig. 1. The device has been fabricated at VTT on a silicon-on-insulator (SOI) wafer having a device-layer thickness of 10μm. The silicon is heavily boron doped having a resistivity of $r \approx 2 \times 10^{-4}\Omega$m. The chain consists of 16 coupled tuning-fork elements that are released from the substrate below to vibrate in the plane of the picture. The tuning forks are identical and each of them has two beams of size $2.5\mu\text{m}\times100\mu$m coupled at the ends of the beams and anchored to the surrounding structures by the vertical connects of size $2.5\mu\text{m}\times10\mu$m. The size of the coupling connect between the tuning forks is $2.5\mu\text{m}\times5\mu$m. The capacitive transducer pads at left and right ends of the chain have a size of $40\mu\text{m}\times75\mu$m and are separated from the first and last tuning fork by a gap of size 0.5μm. The gap has to be made as small as possible in order to maximize the strength of the capacitive coupling (reaching gaps of size 0.1μm has been demonstrated [6]). The signal is brought to the capacitive transducer pads along the metallizations as shown in left and right edges of Fig. 1.

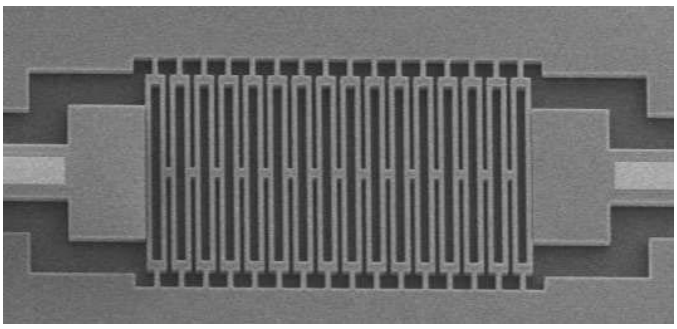

Fig. 1. IR microscope picture (top view) of a spring-mass-chain delay-line structure consisting of 16 coupled tuning forks. Length of the period in the chain is 12.5μm.

The fabrication process is illustrated in Fig. 2. Process begins with a SOI wafer having a 1μm buried oxide beneath a 10μm silicon device layer. After depositing a 1μm low temperature oxide on the wafer backside (a), an Al metallization is deposited and patterned on the front side (b). This metallization consists of a TiW diffusion barrier, 1μm Al, and a thin Mo top layer. Etching is carried out using either dry chlorine-based chemistry or wet etching. A short dip in Freckle etchant is used to remove the residual etch debris. Sawing lines are then patterned into the backside oxide and etched a few microns deep. The next step (c) is the patterning of the resonator structures, with nominal gaps of 0.5μm, and release holes with 1.5μm diameter. Inductively coupled plasma (ICP) etching is used to form the narrow gaps using the resist mask, which is then stripped in oxygen plasma before the backside sawlines are etched to a greater depth (d), again using ICP etching but with the previously patterned oxide as a mask. The buried oxide (and backside LTO) is then etched several minutes in 49% HF followed by drying in supercritical

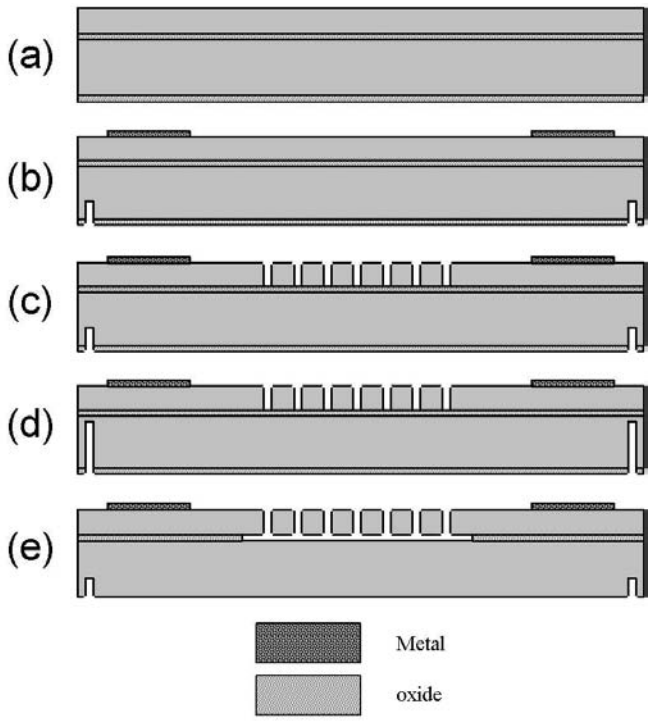

Fig. 2. MEMS device fabrication process. (a) Oxide deposition, (b) metallization, (c) device patterning, (d) sawline etching, (e) device releasing.

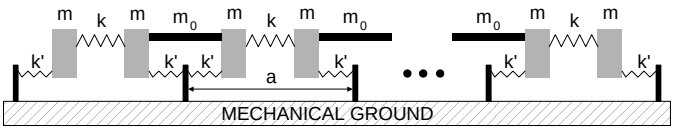

Fig. 3. Simplified model of the tuning-fork chain of Fig. 1.

CO2 (e). The devices may be separated by cleaving along the sawlines or by sawing.

III. Analytical Model

At the frequency range of interest, each tuning fork can be modelled as two equal masses m connected to each other by a coupling spring k and anchored to walls with springs k'. The squared frequency ratio $(\omega_a/\omega_s)^2$ of the antisymmetric (masses moving with 180° phase difference) and symmetric (masses moving in phase) resonances of the tuning forks determines the ratio of the spring constants k and k':

$$k'/k = \frac{2}{(\omega_a/\omega_s)^2 - 1}. \tag{1}$$

If the masses coupling the consecutive tuning forks have a size of m_0, the chain can be modelled as shown in Fig. 3 without dissipation that can easily be included. Calculation of the dispersion relation for the anchored spring-mass chain of Fig. 3 is a straightforward generalization of the common text-book result for an unanchored chain [7]. Defining $K \equiv k'/k$ one finds for the center frequency $\omega_0 = 2\pi f_0$, bandwidth $\Delta\omega = 2\pi\Delta f$ and signal group velocity in the center of the passband v_g of the chain:

$$\begin{aligned}
\omega_0 &= \sqrt{\frac{2k}{2m+m_0}}\sqrt{K+1} \\
\Delta\omega &= \sqrt{\frac{2k}{2m+m_0}}\left(\sqrt{K+2}-\sqrt{K}\right) \\
v_g &= \frac{a}{2}\sqrt{\frac{2k}{2m+m_0}}/\sqrt{K+1}\ ,
\end{aligned} \tag{2}$$

where a is the length of the period of the chain. For the structure in Fig. 1 we have $a = 12.5\mu$m, and assume $k' = 258$N/m, $k = 33.5$N/m, $m = 2.1\times10^{-12}$kg, and $m_0 = 2.91\times10^{-13}$kg. Parameters k', k and m have been approximated based on FEM simulations with ANSYS® and with the well known results for vibrating beams [8] using an isotropic approximation for the SOI material with Young's modulus $Y = 130$GPa and density $\rho = 2330\text{kg/m}^3$. The coupling mass m_0 is taken as the dimensional mass of the connect. One finds with (2) $f_0 \approx 1.8$MHz, $\Delta f \approx 210$kHz and $v_g \approx 8.2$m/s. Result (2) furthermore shows that increasing the strength of the anchoring spring k' with respect to the coupling spring k increases the center frequency while decreasing both bandwidth and group velocity.

IV. Measurement and Simulation Results

Measurement of the S_{21} for the delay line has been done with HP4195A network analyser. The MEMS device and a JFET preamplifier were placed in a vacuum chamber having a 0.001bar pressure. The circuit diagram of the measurement setup is shown in Fig. 4 with the preamplifier modelled by measured input capacitance and resistance. The resonator chain and the capacitive signal connects have been modelled with the MEMS transducer and resonator components of Aplac. Noise has not been included in the simulations. The center frequency and bandwidth expected based on the analytic calculation above is in relatively good agreement with the measured response of Fig. 5. Furthermore, as shown in Fig. 6 the Aplac simulation produces essentially the same result that has been measured. The absolute level of S_{21} has been removed in the measurement by calibrating the network analyser with zero bias voltage. Here C_{thr} has been measured for the device, $(\omega_a/\omega_s)^2$ is obtained through FEM simulations, and Q is selected based on measured properties of single tuning-fork resonators.

It is found that the main reasons for suboptimal performance in Fig. 5 are the feed-through capacitance C_{thr}, too low bias voltage and electrical softening of the first and last springs in the chain introduced by the capacitive transducers. Improving on these issues leads to significantly better performance as suggested by the simulation results of Fig. 7 where also the resulting group delay has been shown. In particular, we have reduced the feed-through capacitance to 1fF, increased the bias voltage close to its limits to $U_{\text{dc}} = 35$V (76% of the pull-in voltage), and canceled the electrical spring softening in the first and last tuning fork. Compensation for the electrical spring softening by strengthening the first and last springs is critical for optimum signal coupling to the line. The reduction of the feed-through capacitance has a smaller effect on the dynamic range and pass-band ripple of the device. The feed-through capacitance can be reduced, for example, by using a differential readout amplifier as suggested in [9]. The ripple in the passband response and in the group delay can be further

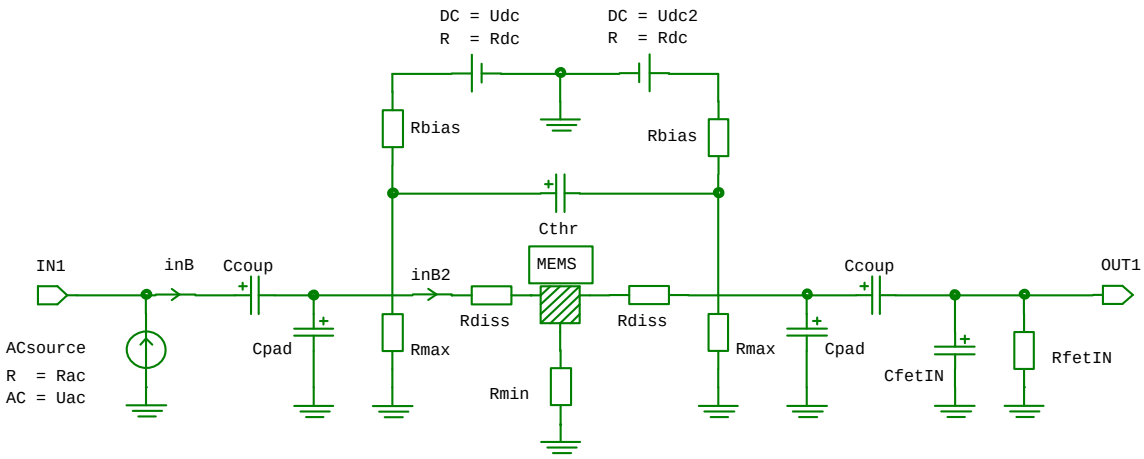

Fig. 4. Circuit diagram used in the Aplac simulation of the measurement setup. Here symmetric bias has been used ($U_{dc} = U_{dc2}$), and $R_{ac} = R_{dc} = 50\Omega$, C_{coup}=100nF, $C_{pad} = 0.3$pF and $R_{bias} = 10M\Omega$. The input capacitance and resistance of the measurement preamplifi er are C_{fetIN} =6pF, $R_{fetIN} = 10M\Omega$.

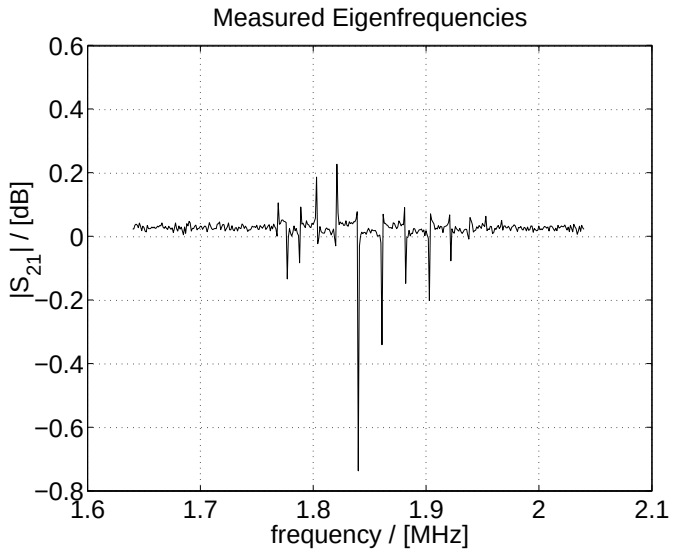

Fig. 5. Measured amplitude response of the device of Fig. 1 with 15V bias voltage and 0dBm signal level. Calibration of the network analyser is done with 0V bias.

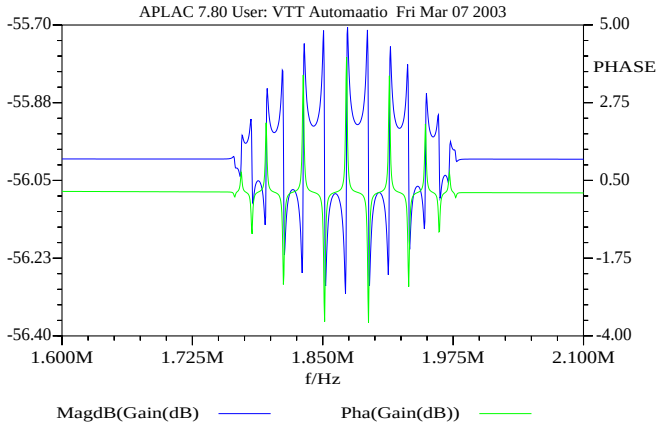

Fig. 6. Simulated voltage gain V_{out}/V_{in} corresponding to the measurement in Fig. 5 with $C_{thr} = 10$fF, $U_{dc} = 15$V, $Q = 10^3$, $N = 16$, $(\omega_a/\omega_s)^2 = 1.26$, and $R_{diss} = 0$. Values of C_{thr} and Q are measured for the device on Fig. 5. The frequency ratio $(\omega_a/\omega_s)^2$ is obtained through FEM simulations. Parameters of the model in Fig. 3 are as stated in text below (2).

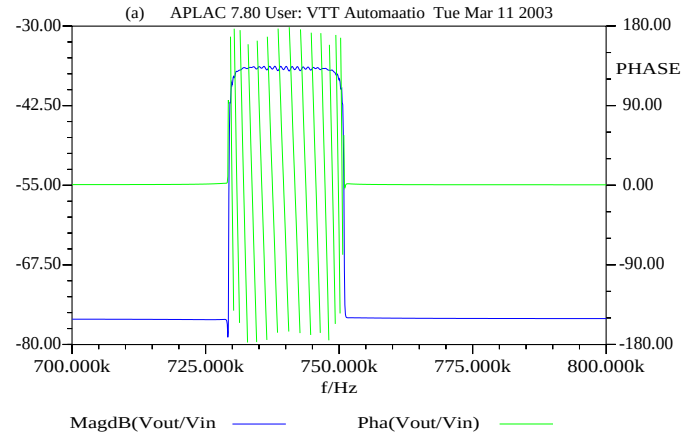

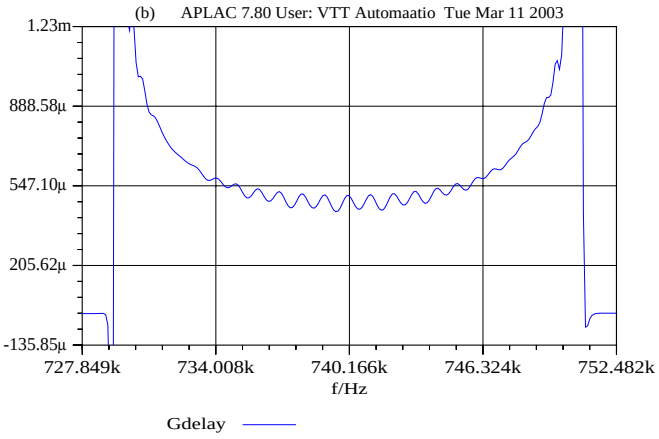

Fig. 7. (a) Simulated V_{out}/V_{in} in a measurement setup of Fig. 4 for a structure where extra masses of m_0 =2.5e-11kg are added between the tuning forks with $(\omega_a/\omega_s)^2 = 1.06$ and $Q = 10^4$ in a chain of $N = 32$ (period of the chain is now 25μm). Half of the extra mass is added before the fi rst and after the last tuning fork in the chain. Furthermore, bias voltage is set to $U_{dc} = 35$V, feed-through capacitance is reduced to $C_{thr} = 1$fF, and resistors of $R_{diss} = 1M\Omega$ are used to reduce the quality factor (smooth out the resonances of the chain). The fi rst and last tuning-fork springs are strengthend to cancel the electrical softening. For the rest of the chain we have (see Fig. 3) $k' = 307$N/m, $k = 9$N/m and $m = 2.1 \times 10^{-12}$kg. (b) Group delay in seconds through the structure considered in (a). At the passband center the delay is 450μs corresponding to signal group velocity of 1.8m/s. The simulated results are in agreement with (2).

reduced by increasing the number of the periods in the chain, increasing the electrical dissipation R_{diss} and decreasing the bandwidth by strengthening the achoring springs as discussed above.

The characteristic impedance level of the MEMS transmission line can conveniently be probed in Aplac simulations. With 0.5μm transducer gaps, the impedance level varies accross the passband in the few-megaohms range. Reducing the transducer gap is an effective solution to reach significantly lower impedances. Namely, the characteristic impedance depends on the gap as $Z \propto d^4$ while the depence on other parameters, such as resonator mass (m), spring constant (k), transducer area (A) and bias voltage (U_{dc}), is at most of the second order. In fact, the result for the characteristic impedance of bulk-acoustic rod wavequides in [10] ($Z = d^4\sqrt{\rho E}/(A(\varepsilon_0 V)^2)$, where E and ρ are the Young modulus and density of the rod material, respectively) roughly generalizes to the current situation when the mechanical characteristic impedance of the rod $A\sqrt{\rho E}$ is replaced by $\sqrt{km}$ (see Fig. 3). Furthermore, comparing to [10], it is found that the characteristic impedance of the spring-mass chain typically is several orders of magnitude lower than the rod-wavequide values. Thus the spring-mass-chain approach can provide a more feasible realization for a MEMS delay line when the needed operation frequency is not too high. Among other possible solutions to reduce the impedance level of MEMS delay lines is to use inductive coupling instead of the capacitive transducers. This, however, would require an external magnetic field.

V. Conclusion

We have described a MEMS structure where mechanical wave propagation with extremely low velocity can be used for signal trasmission to construct a delay line reaching high delays without digital signal processing. Future work focuses on optimizing the performance of the line and on reducing the gap as well as the vibrating dimensions of the structure in order to reach higher frequencies and lower characteristic impedances of the delay line.

Acknowledgement

This work is supported by the Academy of Finland (grant 20542).

References

[1] B. A. Auld, *Acoustic Fields and Waves in Solids*, 2nd ed., Krieger, 1990.

[2] T. Mattila, J. Kiihamäki, T. Lamminmäki, O. Jaakkola, P. Rantakari, A. Oja, H. Seppä, H. Kattelus, and I. Tittonen, "A 12 MHz Bulk Acoustic Micromechanical Oscillator," *Sensors and Actuators A: Physical*, vol. 101, pp. 1–9, Sept. 2002.

[3] Ville Kaajakari, Tomi Mattila, Aarne Oja, Jyrki Kiihamäki, Hannu Kattelus, Mika Koskenvuori, Pekka Rantakari, Ilkka Tittonen, and Heikki Seppä, "Square-Extensional Mode Single-Crystal Silicon Micromechanical RF-resonator," in *Proc. Transducers´03*, June 8–12, 2003.

[4] Clark T.-C. Nguyen, "Frequency-Selective MEMS for Miniaturized Low-Power Communication Devices," *IEEE Trans. Microwave Theory Tech.*, vol. 47, no. 8, pp. 1486–1503, Aug. 1999.

[5] J Jason Yao, "RF MEMS from a device perspective," *J. Micromech. Microeng.*, vol. 10, pp. R9–R38, 2000.

[6] Wan-Thai Hsu, John R. Clark, and Clark T.-C. Nguyen, "A Sub-Micron Capacitive Gap Process for Multiple-Metal-Electrode Lateral Micromechanical Resonators," in *Proc. IEEE MEMS Conference*, Interlaken, Switzerland, 2001, pp. 349–352.

[7] Neil W. Ashcroft and N. David Mermin, *Solid State Physics*, Saunders College Publishing, 1976.

[8] Warren C. Young, *Roark's Formulas for Stress and Strain*, McGraw-Hill, 1989.

[9] P. Rantakari, J. Kiihamäki, M. Koskenvuori, T. Lamminmäki, and I. Tittonen, "Reducing the Effect of Parasitic Capacitance on MEMS Measurements," in *Proc. Transducers´01*, June 8–12, 2001.

[10] Ari T. Alastalo, Tomi Mattila, and Heikki Seppä, "Analysis of a MEMS Transmission Line," to appear in: *IEEE Trans. Microwave Theory Tech.*, vol. 51, no. 8, Aug. 2003.

PUBLICATION VI

Microelectromechanical delay lines with slow signal propagation

In: Journal of Micromechanics and Microengineering 2006. Vol. 16, pp. 1854–1860.
Reprinted with permission from the publisher.
©2006 IOP Publishing Ltd
www.iop.org/journals/jmm

Microelectromechanical delay lines with slow signal propagation

Ari T Alastalo, Jyrki Kiihamäki and Heikki Seppä

VTT Technical Research Centre of Finland, P.O.B. 1000, FI-02044 VTT, Finland

E-mail: ari.alastalo@vtt.fi

Abstract. A slow-wave microelectromechanical delay line, composed of a chain of coupled resonators, is introduced. The delay line has a bandpass response and, depending on structural details, signal group velocity can be as low as $\sim$ 10 m/s that is over 100 times smaller than for acoustical SAW or BAW delay lines. Properties of the delay line are analyzed theoretically and the theory is verified in measurements.

PACS numbers: 84.40.Az, 85.85.+j

1. Introduction

Acoustic wave propagation in solids has for a long time been utilized in electronics to implement various components such as resonators, filters, and delay lines. In these applications, one benefits from i) low attenuation of acoustic waves in crystalline materials and ii) low acoustic wave velocity compared to electromagnetic waves. Low attenuation enables high Q values of mechanical resonators such as in quartz-based oscillators that are widely utilized as low-phase-noise frequency standards in mobile communication devices. Low-loss propagation is also essential in surface-acoustic-wave (SAW) and bulk-acoustic-wave (BAW) filters [1]. The acoustic SAW and BAW velocities are of the order of 5000 m/s that is approximately 10^5 times smaller than the wave velocities for electromagnetic transmission lines. Thus large signal delays can be produced with small-sized components. SAW and BAW delay lines and filters can be used up to several GHz frequencies. The microelectromechanical delay line, presented in this paper, enables a further reduction of group velocity by a factor of $\sim$ 100 for signal frequencies in the HF range (3-30 MHz) and below, which are relevant frequencies, for example, for wireless communication of low-datarate sensor applications and RFID.

Acoustic delays have been utilized in several applications. For example, in wireless passive SAW RFID tags and sensors, the transmitted data is coded into a multitude of reflections of a SAW pulse that is generated (in response to a received radio pulse) and detected by an antenna connected to a SAW chip [2, 3]. In these applications, long acoustic delays and short transmission distances guard against interference from multipath radio propagation. In radar systems, delay lines are used, for example, to

create a delayed replica of the transmit signal to correlate with the received signal reflected from the target [4], to compensate for phase errors in FMCW radars [5] or to simulate a target [6]. In delay-line oscillators, long delay stabilizes the frequency and suppresses off-carrier phase noise [7, 8, 9, 10]. Delay-line based information processing has been applied to implement convolution, time inversion and Fourier transforms [11, 12, 13]. Analog delays are also proposed for novel ultra-wideband receivers [14]. In video systems, delay lines are used, for example, in event recorders and action replay.

The recent advances in microelectromechanical systems (MEMS) technology have opened the possibility for creating miniturised acoustical devices. As an example, a micromechanical resonator based on BAW-operation has been demonstrated to be well suited for a high-spectral-purity oscillator [15] in mobile-communication applications. Integrability of MEMS technology with CMOS electronics as well as size reduction and power savings of MEMS components compared to off-chip solutions (such as SAW devices) facilitate design of efficient single-chip radio transceivers that could revolutionise wireless communication devices [16].

In this paper, a narrow-band capacitively-coupled dispersive MEMS delay line for signals at HF frequencies is analyzed in detail. The delay line consists of a chain of coupled and anchored micromechanical resonators and can have a 100 times smaller signal group velocity than in SAW or BAW delay lines thus facilitating miniaturization of delay-line components. A similar structure for lower frequencies was introduced in [17]. In this paper, general theory of anchored spring-mass-chain delay lines is formulated and an electrical-equivalent model is derived. The theory is verified with measurements of two different fabricated delay lines composed of 80 tuning-fork resonators in series. Design improvements necessary for practical applications are discussed.

2. Theory

The anchored spring-mass-chain waveguide, shown in figure 1 without dissipation, is composed of elementary resonators that can be modelled with two moving masses, m, that are coupled with a spring k and anchored to a stationary support with springs k'. Except for the ends, the chain is periodic with period a. The waveguide can be seen as a high-order bandpass filter [16, 18] with identical stages. Transduction between electrical signals and a mechanical wave propagating along the chain is done with capacitive parallel-plate transducers with gap d, area BH and rest capacitance $C_0 = \epsilon_0 BH/d$. Here H is the thickness of the device (perpendicular to the plane of the picture) and B is the length of the transducers as shown in figure 1. The model in figure 1(e) is also applicable, for example, for periodic resonator chains where the inter-stage coupling is done with a capacitor instead of the mechanical spring. In this paper, damping is not considered in theory but is modelled in simulations. For low losses, this results in good theoretical estimates of the properties of the waveguide.

The elementary resonator of figure 1 has two fundamental modes of vibration with

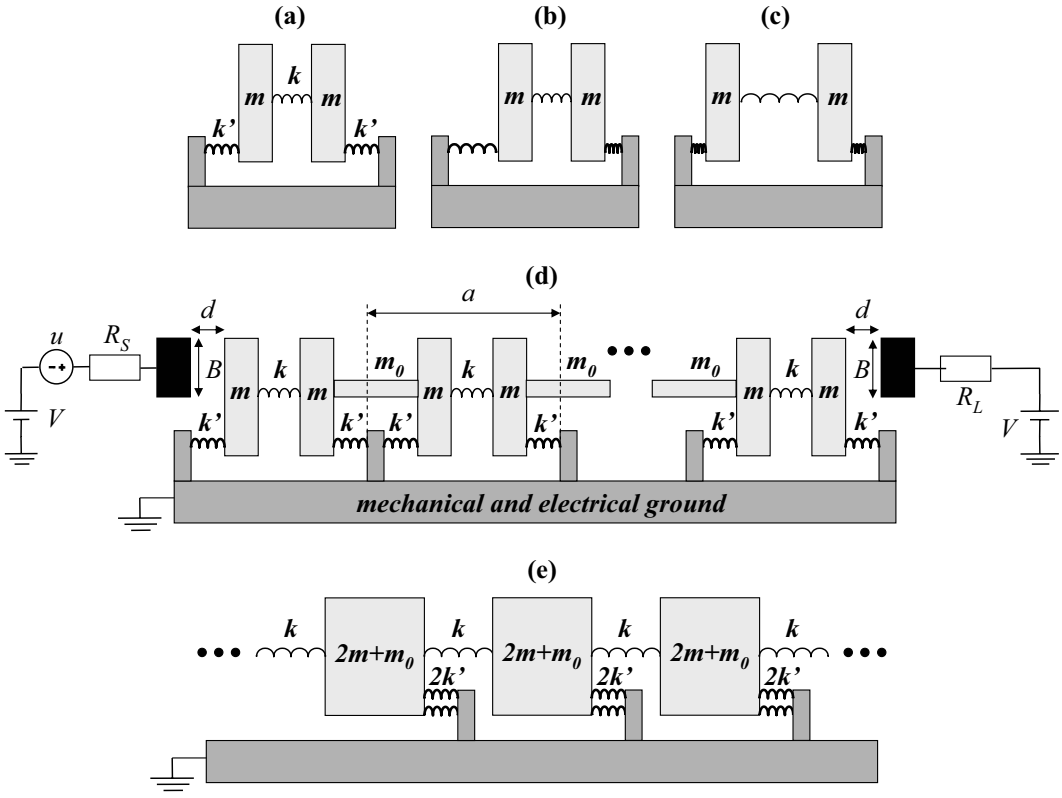

Figure 1. (a) Rest position of an elementary two-mode resonator with symmetric (b) and antisymmetric (c) eigenmodes. (d) Delay line consisting of capacitive input (left) and output (right) transducers with gap d and a chain of coupled resonators. Except for the ends of the chain, the waveguide can be modelled as shown in (e). Losses are not indicated.

resonance frequencies

$$\omega_s = \sqrt{\frac{k'}{m}} \tag{1}$$

$$\omega_a = \sqrt{\frac{2k + k'}{m}}. \tag{2}$$

In the symmetric mode, with resonance frequency ω_s (1), the masses move in phase while in the antisymmetric mode, with frequency ω_a (2), there is a 180° phase difference between the mass motions. A useful parameter is the ratio of the anchoring spring k' to the coupling spring k, determined by ω_a/ω_s as

$$K \equiv k'/k = \frac{2}{(\omega_a/\omega_s)^2 - 1}. \tag{3}$$

For a particular resonator geometry, the ratio of the resonance frequencies is obtained, for example, in FEM eigenmode analysis or in measurements.

A periodic chain of coupled resonators can vibrate and carry signals at frequencies allowed by the dispersion relation $\omega(\kappa)$ that gives the frequency ω as a function of the wave vector $\kappa \equiv 2\pi/\lambda$, where λ is the wavelength. For the anchored chain of figure 1,

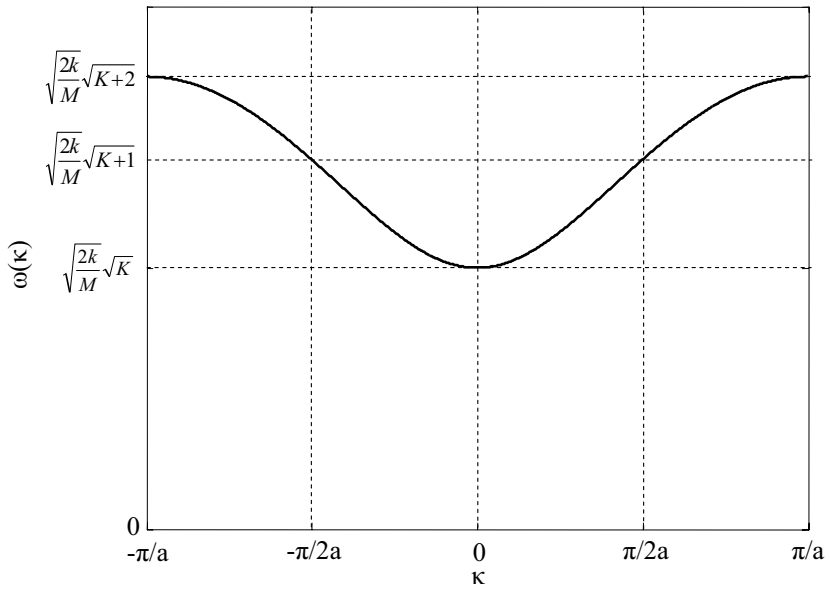

Figure 2. Dispersion relation for the anchored spring-mass chain of figure 1.

the dispersion relation is found as a generalization of the familiar text-book result for periodic unanchored (free) chains [19]. One obtains for the anchored chain

$$\omega(\kappa) = \sqrt{\frac{2k}{M}}\sqrt{1-\cos(\kappa a)+K}, \tag{4}$$

where $M \equiv 2m + m_0$ is the total coupled-resonator mass, a is the period of the chain and the wave vector $\kappa \in [-\pi/a, \pi/a]$ is restricted to the first Brillouin zone [19]. The dispersion relation (4) is illustrated in figure 2. As opposed to the low-pass character of free chains, nonzero k' forbids zero-frequency oscillations and results in passband response.

Group velocity for signal propagation along the chain is found from (4) as

$$v_g = \frac{\partial\omega}{\partial\kappa} = \frac{a}{2}\sqrt{\frac{2k}{M}}\frac{\sin(\kappa a)}{\sqrt{1-\cos(\kappa a)+K}}, \tag{5}$$

and is seen to differ from the phase velocity $v_{ph} = \omega/\kappa$. For the center frequency $\omega_0 = 2\pi f_0$ and bandwidth $\Delta\omega = 2\pi\Delta f$ of the line one finds

$$\omega_0 = \omega(\frac{\pi}{2a}) = \sqrt{\frac{2k}{M}}\sqrt{K+1} \tag{6}$$

$$\Delta\omega = \omega(\frac{\pi}{a}) - \omega(0) = \sqrt{\frac{2k}{M}}\left(\sqrt{K+2} - \sqrt{K}\right). \tag{7}$$

At the center of the passband, one obtains for the phase and group velocities

$$v_{ph}^0 \equiv \left.\frac{\omega}{\kappa}\right|_{\omega_0} = \frac{2a}{\pi}\sqrt{\frac{2k}{M}}\sqrt{K+1} \tag{8}$$

$$v_g^0 \equiv \left.\frac{\partial\omega}{\partial\kappa}\right|_{\omega_0} = \frac{a}{2}\sqrt{\frac{2k}{M}}\frac{1}{\sqrt{K+1}} \tag{9}$$

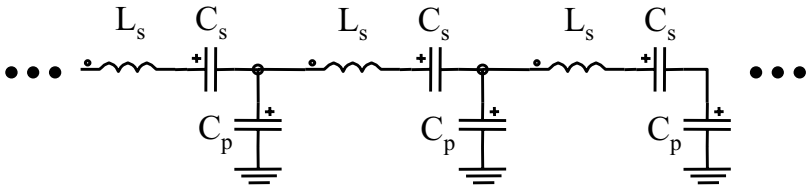

Figure 3. Electrical-equivalent model for the spring-mass-chain transmission line in figure 1 for center-band operation.

illustrating, again, clearly the dispersive character of the spring-mass chain.

For single capacitively-coupled MEMS resonators with spring constant k, mass m and quality factor Q, the electrical equivalent is a series RLC circuit (see, for example, [20]) with $R = \sqrt{km}/(Q\eta^2)$, $L = m/\eta^2$ and $C = \eta^2/k$, where $\eta = C_0V/d$ is the electromechanical coupling coefficient while C_0 is the transducer rest capacitance, V the bias voltage and d the transducer gap as in figure 1. To find a similar representation for the spring-mass-chain transmission line, the propagation constant κa in (4) is solved and its square, $(\kappa a)^2 = Z_sY_p$, [21] is expanded as a power series with respect to ω^2 around the passband center. Here Z_s is the series impedance and Y_p is the shunt admittance of the waveguide per unit length. One finds

$$(\kappa a)^2 = \left\{ \frac{j\omega M}{\eta^2} + \frac{2k}{j\omega\pi\eta^2} \left[\pi(1+K) - \left(\frac{\pi}{2}\right)^2 \right] \right\} \frac{j\omega\pi\eta^2}{2k}, \tag{10}$$

where $Z_s = j\omega L_s + 1/(j\omega C_s)$ and $Y_p = j\omega C_p$ can now be identified, as shown in figure 3, with

$$L_s = \frac{M}{\eta^2} \tag{11}$$

$$C_s = \frac{\pi\eta^2}{2k\left[\pi(1+K) - (\pi/2)^2\right]} \tag{12}$$

$$C_p = \frac{\pi\eta^2}{2k}. \tag{13}$$

Consequently, one obtains the characteristic impedance of the line as [21]

$$Z_c = \sqrt{\frac{Z_s}{Y_p}} = \frac{\sqrt{kM}}{\eta^2\sqrt{2(K+1)}}. \tag{14}$$

The scaling of the terms in (10) with the squared coupling coefficient, η^2, is done in order to have the correct $Z_c \sim 1/\eta^2$ dependence of the characteristic impedance as verified in simulations.

It is seen that increasing the strength of the anchoring spring k' with respect to the coupling spring k increases the center frequency (6) and phase velocity (8) while decreasing bandwidth (7), group velocity (9) and the characteristic impedance (14) that, typically, is much higher than 50 Ω with electrostatic coupling. Furthermore, for higher K, the variation of the group velocity as a function of frequency at band center

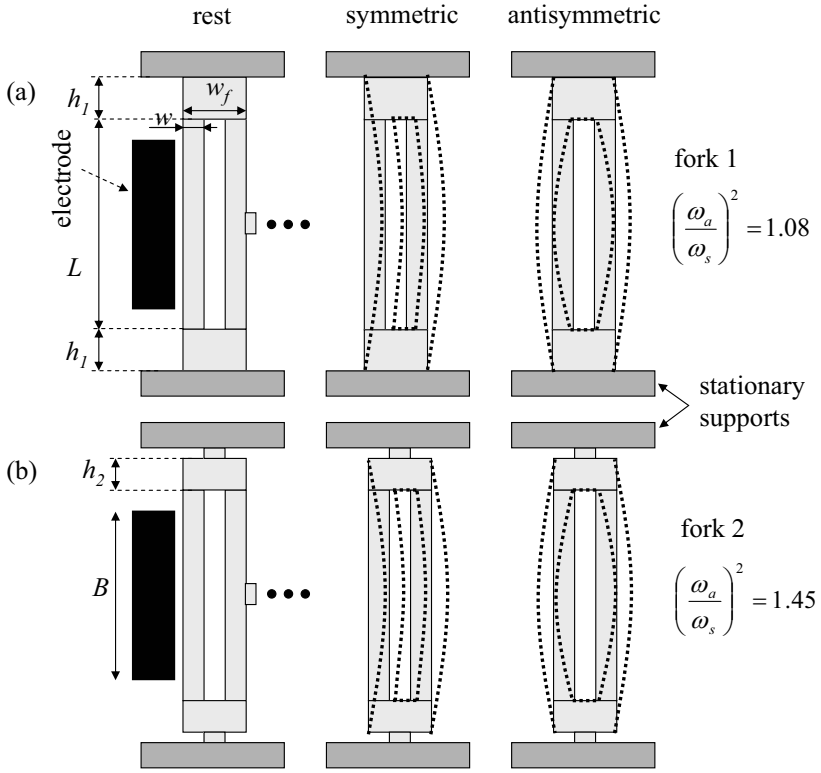

Figure 4. Two different tuning-fork designs (fork 1 in (a) and fork 2 in (b)) for the elementary resonator of figure 1.

is reduced. For good signal coupling and long delays, it is thus desirable to have K as high as possible.

3. Design with tuning-fork resonators

One possible realization for the elementary resonators in figure 1 is the doubly-supported tuning-fork structure for which two geometries are schematically shown in figure 4. For both designs, the distance between the anchoring connects to the stationary supports is the same and the vibrating beams are of same size (5 μm $\times$50 μm). The only difference in the designs is at the anchoring structure. Fork 2 (figure 4(b)) has a weaker coupling to the support than fork 1 and, correspondingly, a stronger coupling between the beams (stronger k and smaller K) resulting in wider frequency separation between the eigenmodes and higher characteristic impedance. The dimensions and central properties of the tuning forks as well as corresponding transmission lines composed of 80 resonators are collected in table 1. The FEM results are calculated with ANSYS® .

Table 1. Design values and FEM results for the parameters of the tuning-fork resonators of figure 4. For Z_c a bias voltage of $V = 25.6$ V has been used. For the group delay T_g^0, a chain of 80 resonators, with a total length of the line of $L_{line} = 1.4$ mm, is considered.

	fork 1	fork2	unit	comment
h	$h_1 = 10$	$h_2 = 7.5$	μm	design
f_s	13.573	11.406	MHz	FEM
f_a	13.992	13.748	MHz	FEM
k'	17.3	12.4	kN/m	FEM
K	31.9	4.42		FEM
M	4.77	4.81	ng	(1), (2)
f_0	13.8	12.6	MHz	(6)
Δf	0.42	2.34	MHz	(7)
v_{ph}^0	965	884	m/s	(8)
v_g^0	23	128	m/s	(9)
T_g^0	60.8	10.9	μs	$\frac{L_{line}}{v_g^0}$
Z_c	0.96	5.42	MΩ	(14)
L	50		μm	design
B	45		μm	design
w	5		μm	design
w_f	15		μm	design
d	200		nm	design
H	10		μm	design
a	17.5		μm	design
L_{line}	1.4		mm	design
C_0	20		fF	

4. Experimental verification

To verify the spring-mass-chain model, periodic narrow-gap single-crystal-silicon resonator chains, corresponding to the tuning-fork designs in figure 4 and table 1, were fabricated on silicon-on-insulator (SOI) wafers and characterized. Figure 5 shows a SEM picture of the fabricated resonator chains. The number of coupled resonators in the chain is 80 as considered in table 1. One thus expects center-band group delays of

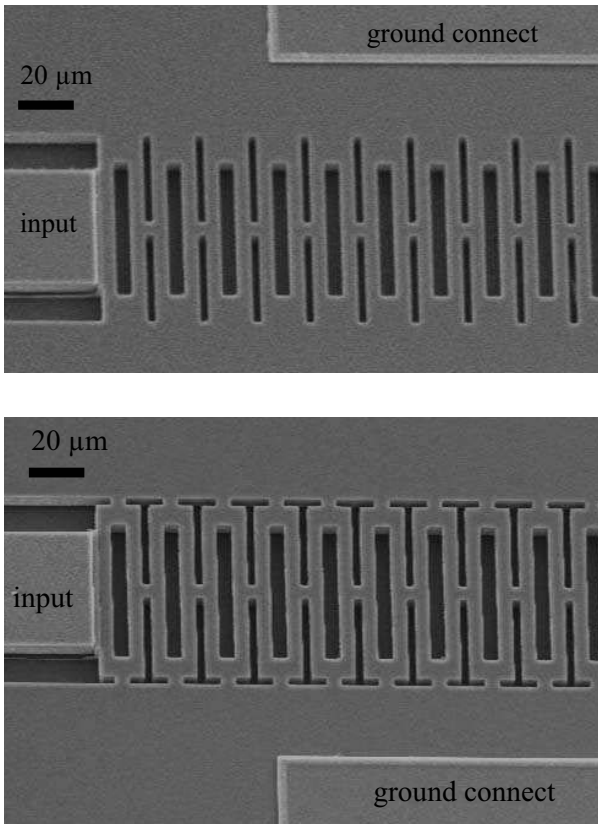

Figure 5. SEM picture of tuning-fork chains composed of fork 1 (up) and fork 2 (lower) of table 1.

45 μs and 10 μs for 1.4 mm long tansmission lines made of fork 1 and fork 2 of figure 4, respectively. As the fabrication process is detailed elsewhere [22], only the experimental set-up and results are given here.

Figure 6 shows a schematic of the measurement and simulation setup. The mechanical transmission lines, chain 1 and chain 2 of figure 5, and their input and output transducers are represented by the black-box components. Component values of figure 6 are collected in table 2.

In measurements, the input (in) and output (out) are connected to an HP 4195A network analyzer. The resonator chains, biasing circuits and the differential low-noise preamplifier (AD8129) are kept in a vacuum chamber with a pressure of 3 μbar. Only one of the transmission lines is measured at a time with nonzero bias voltage. In the other branch, with zero bias, signal propagates only through the parasitic feed-through capacitance C_{thr1} or C_{thr2}. Consequently, the differential readout suppresses the feed-through signals and amplifies only the signal propagating through the mechanical waveguide. As C_{thr1} and C_{thr2} are slightly different, trimmer capacitors, C_{tune1} and C_{tune2}, are utilized in the waveguide inputs such that a common-mode-rejection ratio (CMRR) of 61 dB is achieved. Here the feed-through capacitances of the two devices are almost equal and thus the cancellation is conveniently done using the unbiased

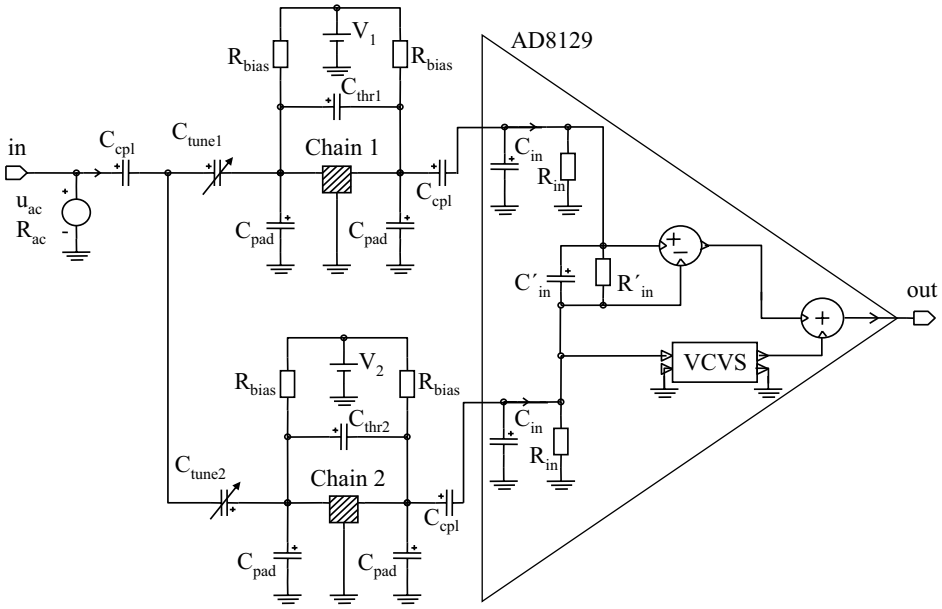

Figure 6. Measurement and simulation setup.

Table 2. Parameter values for the measurement and simulation setup of figure 6.

parameter	value	unit
C_{thr1}	≈ 30	fF
C_{thr2}	≈ 30	fF
C_{tune1}	$\in [0.5, 15]$	pF
C_{tune2}	$\in [0.5, 15]$	pF
C_{cpl}	100	nF
C_{pad}	360	fF
C_{in}	4	pF
C'_{in}	3	pF
R_{ac}	50	Ω
R_{bias}	3.6	MΩ
R_{in}	4	MΩ
R'_{in}	1	MΩ

component as a reference. More generally, one can use a tuneable capacitance of the same order as the feed-through capacitances for the reference. In addition to the high CMRR, the preamplifier has a differential gain of 17 dB. The transmission S_{21} is measured with respect to a short connecting the input and output of the network analyzer.

In simulations, the electrical circuit, transducers and the mechanical resonator chains are modelled in Aplac® [23] circuit simulator. The preamplifier is modelled as shown in figure 6. The voltage-controlled voltage source (VCVS) is used to tune the common-mode-rejection ratio to the measured level of 61 dB.

Figure 7 shows the measured and simulated responses for the two different spring-mass-chain transmission lines. The simulation results that reasonably well fit the measurements are obtained by varying the electrode length B, mechanical quality factor Q of the elementary resonators, the ratio of the spring coefficients K, the anchoring spring k' and the transducer gap d from the design values given in table 1. The fitting values for these parameters are given in table 3. The difference between the designed (table 1) and fitted (table 3) values for the spring coefficients can be explained by i) a finite stiffness of the support (assumed stationary in design as indicated in figure 4) at the anchoring of the tuning forks and ii) slight narrowing ($3-6$ %) of the structures in processing. The passband ripple and high loss are due to impedance mismatch at the input and output of the waveguide. Matched termination would require source and load impedances to equal the characteristic impedance Z_c given in table 1. The gentle slope of the measured responses in the lower passband edge can be due to the finite stiffness of the low-Q anchoring connects. For the higher passband frequencies, the consecutive resonators move mostly out of phase, which suppresses the anchor motions and the associated losses. The dip in figure 7 (b) is likely caused by unideal periodicity of the chain due to fabrication tolerances or by contamination.

Figure 8 shows the measured and simulated group delays for the resonator chains. As in the response of figure 7, the ripple is due to impedance mismatch. Simulation with matched source and load impedances removes the ripple and gives center-band group delays of 20 μs and 10 μs for chain 1 and chain 2, respectively, as indicated with a thick solid line in figure 8. This is in agreement with theoretical predictions when the fitted values for the spring coefficients in table 3 are used in (9).

5. Low-impedance design

As the above measurement results show, the analysis of section 2 can be used to design MEMS resonator-chain delay lines with record high time delays in a given physical size. However, to facilitate matched source and load termination for the MEMS delay line and to avoid using a differential readout (see figure 6), a much lower characteristic impedance, well below the pad (C_{pad}), feed-through (C_{thr}) and transducer (C_0) impedances, is needed than what was obtained above in table 3. As shown by (14) this can be achieved by enhancing the coupling, η, and by strenghtening the anchoring

Table 3. Parameter values for the tuning-fork resonators that give a better fit between simulations and measurements in figure 7 than the design values of table 1.

	fork 1	fork2	unit
k'	12.6	9.9	kN/m
K	8.5	3.3	
f_0	12	11	MHz
Δf	1.3	2.6	MHz
v_g^0	70	140	m/s
T_g^0	20	10	μs
Z_c	6	13	MΩ
B	42		μm
d	230		nm
Q	8000		

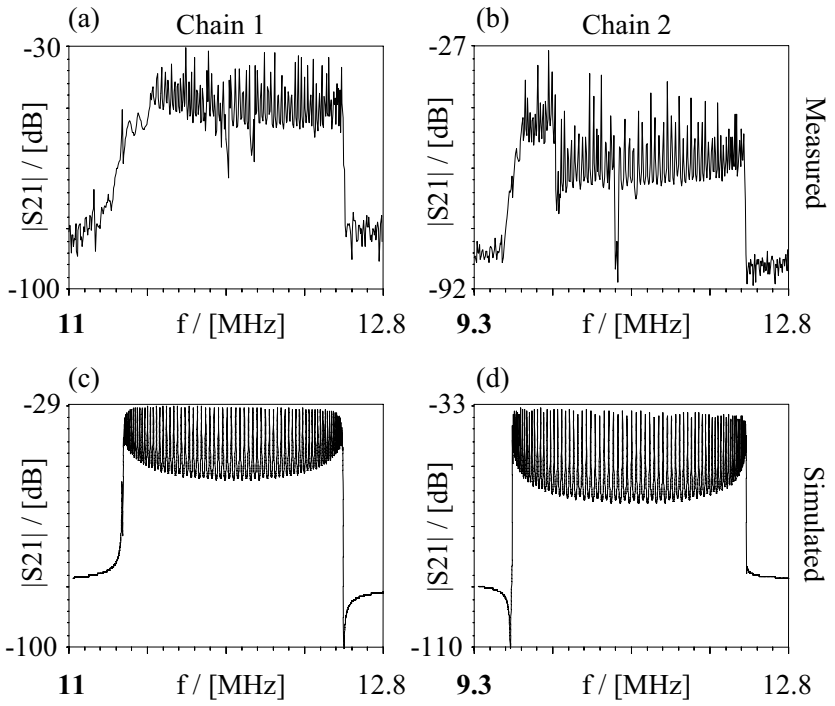

Figure 7. Measured ((a) and (b)) and simulated ((c) and (d)) $|S_{21}|$ for chain 1 ((a) and (c)) and chain 2 ((b) and (d)). The ripple is due to impedance mismatch at source and load.

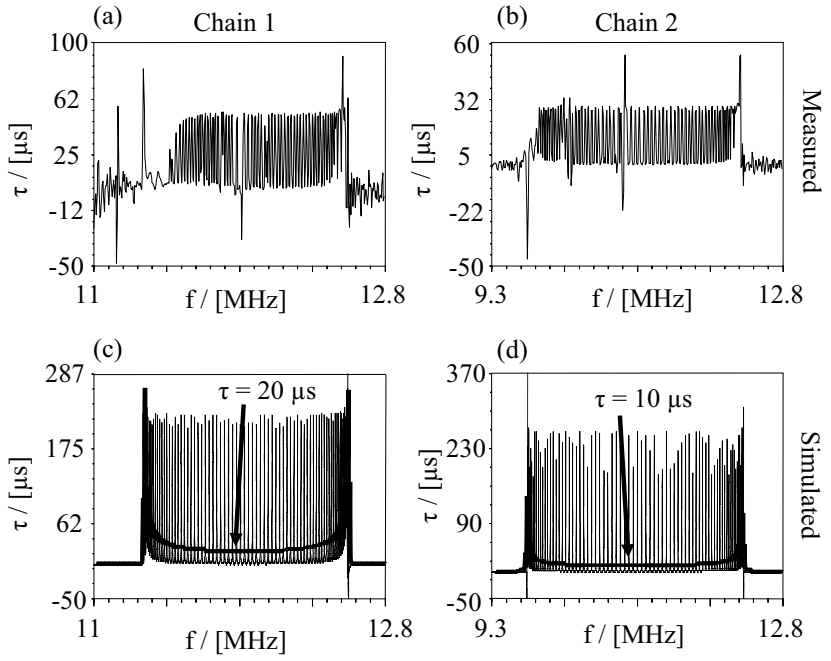

Figure 8. Measured and simulated group delay with ripple due to impedance mismatch as in figure 7. In simulation results ((c) and (d)) the thick solid curves show the group delay with impedance-matched source and load for the line.

spring, k', with respect to the coupling spring, k (larger K). Reducing the anchoring height, h_1, in figure 4 to 5 μm, doubling the beam separation ($w_f \rightarrow 20$ μm) and taking the narrowing of the structures in fabrication into account in design, a much higher spring-constant ratio of $K = 74$ is expected with $k' = 18$ kΩ and $M = 4.8$ ng. For good signal coupling, it is also important to design the first and last resonator in the chain to compensate for the electrical spring softening as well as for the stiffening of the first and last beams due to the capacitive coupling occuring over the transducer area as opposed to the point-force inter-resonator coupling along the chain. If, in addition, the transducer gap is reduced to $d = 100$ nm, a delay line with estimated characteristic impedance of $Z_c = 22$ kΩ (14), bandwidth of $\Delta f = 185$ kHz (7) and group velocity of $v_g^0 = 13$ m/s (9) can be obtained with a bias voltage of 30 V ($\eta = 11$ μFV/m).

Figure 9 shows the simulated response and group delay for a low-impedance chain of 80 resonators with reduced pad ($C_{pad} = 91$ fF $\Rightarrow Z_{pad} = 127$ kΩ) and feed-through capacitances ($C_{thr} = 8$ fF $\Rightarrow Z_{thr} = 1.3$ MΩ). The transducer capacitance is $C_0 = 37$ fF corresponding to $Z_0 = 308$ kΩ. Consequently, the characteristic impedance of the transmission line is much lower than Z_{pad}, Z_{thr} and Z_0 as required by good signal coupling. Figure 10 shows the corresponding simulation setup. To have a flat group delay at band center, resistive source and load termination to $R_L = 14$ kΩ was used that is somewhat lower than the estimated characteristic impedance of 22 kΩ. Higher pad and feed-through capacitances result in passband ripple and increased insertion loss if the characteristic impedance is not simultaneously further lowered.

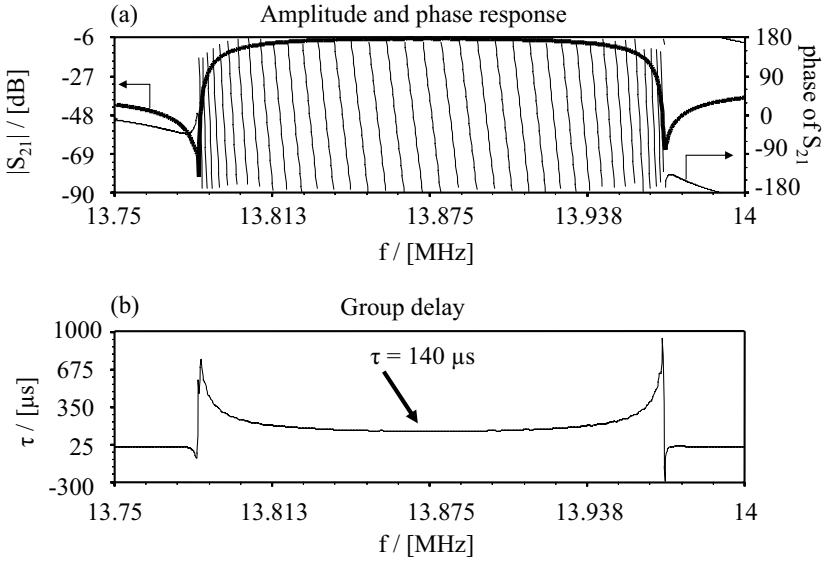

Figure 9. Simulated response (a) and group delay (b) for the low-impedance delay line with 14 kΩ source and load impedance. In (a) the thick line is for the amplitude and the thin line for the phase of S_{21}.

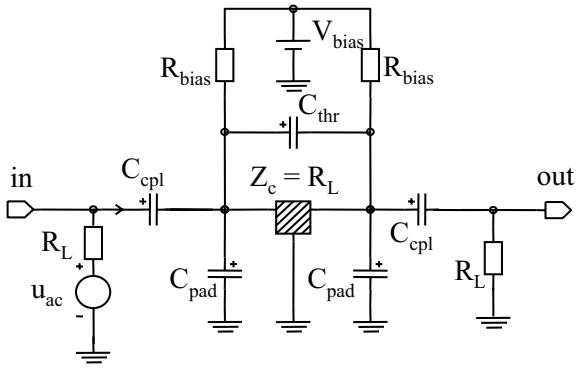

Figure 10. Simulation setup used to obtain the results of figure 9.

Figure 11 shows voltage amplitudes for a simulated transmission of a signal pulse through the delay line. The pulse duration is 115 μs to have the signal spectrum fit in the passband of the line. The signal frequency in the pulse is 13.875 MHz which is at the passband center. The rise time of the output voltage from 10 % to 90 % of the peak value in figure 11(b) is 15 μs.

6. Discussion and conclusions

A capacitively-coupled MEMS delay-line structure with record slow signal propagation was presented for HF frequencies enabling miniaturization of time-delay components. The properties of the delay line were theoretically analyzed and the theory was verified

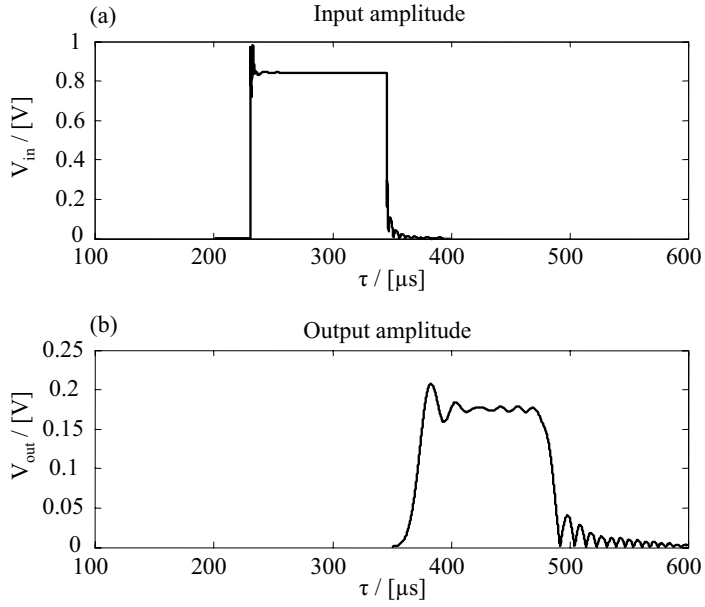

Figure 11. Simulated input (a) and output (b) voltage amplitudes for a pulse of width $\Delta T = 115$ μs transmitted through the delay line of figure 9 at the passband center.

in measurements with fabricated devices consisting of 80 series-connected MEMS resonators. The fabricated delay lines had too high characteristic impedances for practical applications but careful design can result in impedance levels of few kiloohms as shown in the paper. To reach higher frequencies, the resonator dimensions have to be scaled down which, however, weakens the capacitive coupling (increases the line impedance) unless the reduced transducer area is compensated by a smaller gap or a higher bias voltage. For clamped beams, the resonance frequency, f, depends on the width, w, and length, L, of the beam as $f \sim w/L^2$. Since the beam height, H, needs to be kept as high as possible for good coupling, fabrication tolerances easily limit the beam to be well thicker than a micrometer. Thus, for higher frequencies, a lower aspect ratio, L/w, of the beam is required which results in a lower quality factor, $Q \sim (L/w)^3$, due to clamping loss [24]. In addition to a group velocity that is much lower than for other acoustic delay lines (SAW or BAW), the MEMS line is characterized by a narrow-band response. This can be utilized in applications that would otherwise require a separate bandpass filter such as in wireless RF or ultrasound communication systems. For example, a low-power transponder terminal, communicating with on-off keying, is schematically shown in figure 12. Such transponders could be utilized, for example, in low-datarate sensor applications. Here, the reader sends an RF pulse to the sensor terminal in which the pulse is either retransmitted back to the reader (bit 1) or shunted to ground (bit 0).

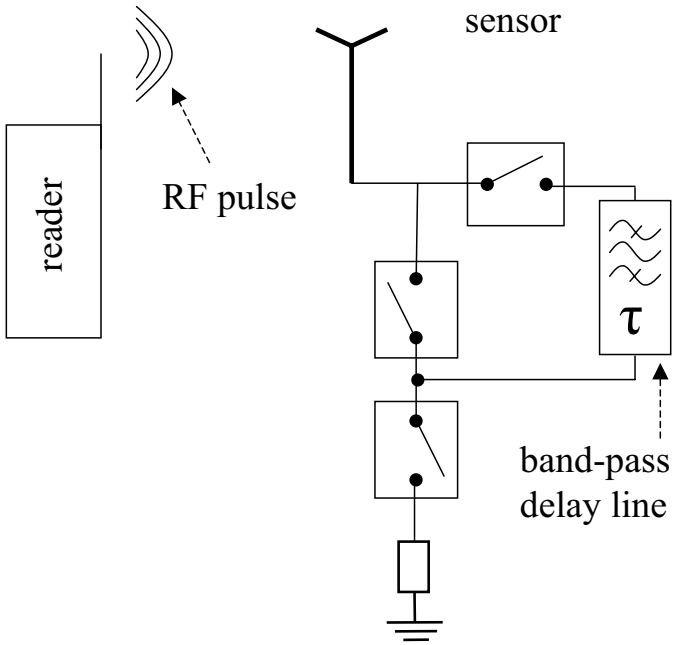

Figure 12. Schematic of a simple delay-line transponder for low-power low-datarate communication in sensor applications.

Acknowledgment

This work is supported by the Academy of Finland (grant 20542) and by Aplac® Solutions. The authors would like to thank Ville Kaajakari for discussions related to this paper.

References

[1] Weigel R, Morgan D P, Owens J M, Ballato A, Lakin K M, Hashimoto K and Ruppel C C W 2002 *IEEE Trans. Microwave Theory Tech.* **50** 738–749.
[2] Reindl L M, Pohl A, Scholl G and Weigel R 2001 *IEEE Sensors J.* **1** 69–78.
[3] Karilainen A, Finnberg T, Uelzen T, Dembowski K and Müller J 2004 *IEEE Trans. Ultrason., Ferroelect., Freq. Contr.* **51** 1464–1469.
[4] Narayanan R M, Zhou W, Wagner K H and Kim S 2004 *IEEE Geosci. Remote Sensing Lett.* **1** 166–170.
[5] Reindl L, Ruppel C C W, Berek S, Knauer U, Vossiek M, Heide P and Oréans L 2001 *IEEE Trans. Microwave Theory Tech.* **49** 787–794.
[6] Zari M C, Anderson C S and Caraway W D III 1995 *IEEE Trans. Microwave Theory Tech.* **43** 1889–1894.
[7] Salmon S K 1979 *IEEE Trans. Microwave Theory Tech.* **MTT-27** 1012–1018.
[8] Parker T E and Montress G K 1988 *IEEE Trans. Ultrason., Ferroelect., Freq. Contr.* **35** 342–364.
[9] Amorosi R I and Campbell C K 1985 *IEEE Trans. Sonics Ultrason.* **SU-32** 574–582.
[10] Ciplys D, Rimeika R, Sereika A, Gaska R, Shur M S, Yang J W and Khan M A 2001 *Electronics Letters* **37** 545–546.

[11] Kino G S, Ludvik S, Shaw H J, Shreve W R, White J M and Winslow D K 1973 *IEEE Trans. Microwave Theory Tech.* **MTT-21** 244–255.
[12] Berg N J, Lee J N, Casseday M W and Udelson B J 1979 *Applied Optics* **18** 2767–2774.
[13] Yin J H, Shen K X, Shui Y, Jiang Z L and He S P 1992 *Electronics Letters* **28** 172–174.
[14] Zhao S, Liu H and Tian Z 2004 In *Proc. IEEE Radio and Wireless Conference*, p 251–254.
[15] Kaajakari V, Mattila T, Oja A, Kiihamäki J and Seppä H 2004 *IEEE Electron Device Lett.* **25** 173–175.
[16] Nguyen C T C 1999 *IEEE Trans. Microwave Theory Tech.* **47** 1486–1503.
[17] Alastalo A T, Mattila T, Seppä H and Dekker J 2003 *Proc. 33rd European Microwave Conference* p 967–970.
[18] Lin L, Howe R T and Pisano A P 1998 *J. Microelectromech. Syst.* **7** 286–294.
[19] Ashcroft N W and Mermin N D 1976 *Solid State Physics* (Saunders College Publishing).
[20] Mattila T, Kiihamäki J, Lamminmäki T, Jaakkola O, Rantakari P, Oja A, Seppä H, Kattelus H and Tittonen I 1998 *Sensors and Actuators A* **101** 1–9.
[21] Ramo S, Whinnery J R and Duzer T V 1984 *Fields and Waves in Communication Electronics* (John Wiley & Sons) 2nd edition.
[22] Kiihamäki J, Kaajakari V, Luoto H, Kattelus H and Ylikoski M 2005 *Proc. The 13th International Conference on Solid State Sensors, Actuators and Microsystems, (Transducers'05)* p 1354–1357.
[23] Aplac RF Design Tool, APLAC Solutions Corp, www.aplac.com.
[24] Yasumura K Y, Stowe T D, Chow E M, Pfafman T, Kenny T W, Stipe B C and Rugar D 2000 *J. Microelectromech. Syst.* **9** 117–125.

Published by

Series title, number and
report code of publication

VTT Publications 616
VTT–PUBS–616

Author(s)
Alastalo, Ari

Title

Microelectromechanical Resonator-Based Components for Wireless Communications

Filters and Transmission Lines

Abstract

Starting in the early 1960's, when the integrated-circuit (IC) technology was developed, micromachining and microelectromechanical systems (MEMS) have grown into a broad research field with several commercial successes. Typical applications of MEMS are in physical, chemical and biochemical sensors, as well as in optical systems such as the digital micromirror device of Texas Instruments. From the 1990's, the advances in the processing technologies and the tremendous growth of the wireless-communication market have drawn much interest into radio-frequency MEMS devices (RF MEMS) such as filters, oscillators, switches and tunable capacitors. These are now beginning to penetrate the market.

This thesis considers electrostatically-actuated RF-MEMS filters and delay lines. For filters, the work concentrates on nonlinear distortion and filter design. The intermodulation properties of capacitively-coupled MEMS filters are analytically solved in closed form and the theory is verified in numerical simulations as well as in measurements with MEMS resonators. The analysis is more generally valid than the previously published results. The theory is utilized to formulate a design procedure for MEMS filters that, for the first time, takes systems speci-fications for tolerable intermodulation distortion and insertion-loss into account. For delay lines, capacitive actuation of bulk-acoustic waves in a solid rod is analyzed. In particular, challenges in impedance matching due to the weakness of the electrostatic coupling are quantified. Finally, a new kind of resonator-chain delay line for high-frequency (HF) signals is introduced. This delay line is characterized by extremely slow signal group velocity (~ 10–100 m/s), narrow-band response, and much lower characteristic impedance than found for the solid-rod waveguide enabling efficient signal coupling. Properties of the resonator-chain waveguide are theoretically analyzed and the results are verified in measurements of fabricated devices.

Keywords

MEMS, radio-frequency MEMS, microelectromechanical filters, microelectromechanical resonators, components, transducers, wireless communication, transmission lines, acoustic wave propagation, intermodulation

ISBN

951–38–6865–6 (soft back ed.)
951–38–6866–4 (URL: http://www.vtt.fi/publications/index.jsp)

Series title and ISSN	Project number
VTT Publications 1235–0621 (soft back ed.) 1455–0849 (URL: http://www.vtt.fi/publications/index.jsp)	

Date	Language	Pages	Price
October 2006	English, finnish abstr.	57 p. + app. 56 p.	C

Name of project	Commissioned by
MIRA	

Contact	Sold by
VTT Technical Research Centre of Finland P.O. Box 1000, FI-02044 VTT, Finland Phone internat. +358 20 722 111 Fax +358 20 722 7012	VTT Technical Research Centre of Finland P.O.Box 1000, FI-02044 VTT, Finland Phone internat. +358 20 722 4404 Fax +358 20 722 4374

Julkaisija

Julkaisun sarja, numero ja raporttikoodi

VTT Publications 616
VTT–PUBS–616

Tekijä(t)
Alastalo, Ari

Nimeke

Mikromekaanisiin resonaattoreihin perustuvat komponentit langattoman tiedonsiirron sovelluksissa

Suodattimet ja siirtolinjat

Tiivistelmä

Mikroelektromekaanisten järjestelmien (MEMS) kehitys alkoi 1960-luvun alussa yhdessä integroitujen piirien (IC) teknologian kanssa. Tähän päivään mennessä mikromekaniikka on kehittynyt laajaksi tutkimusalaksi ja johtanut useisiin kaupallisiin menestyksiin. MEMS-teknologiaa sovelletaan mm. fysikaalisissa, kemiallisissa ja biokemiallisissa antureissa sekä optisissa järjestelmissä, kuten Texas Instrumentsin mikropeileissä, joita käytetään videoprojektroreissa. Kiinnostus radiotaajuisiin MEMS-komponentteihin (RF MEMS) on lisääntynyt voimakkaasti 1990-luvun alusta alkaen valmistusteknologian ja langattoman tiedonsiirron markkinoiden kehityksen myötä. Radiotekniikassa MEMS-teknologiaa pyritään soveltamaan mm. suodattimissa, oskillaattoreissa, kytkimissä ja säädettävissä kondensaattoreissa. Ensimmäiset tällaiset komponentit ovat jo kaupallistuneet.

Tässä väitöskirjassa käsitellään kapasitiivisesti kytkettyjä RF-MEMS-suodattimia ja viivelinjoja. Suodattimien osalta työ keskittyy epälineaarisuuksien ja häviöiden huomioimiseen suodinsuunnittelussa. MEMS-suodinten intermodulaatio-ominaisuudet ratkaistaan työssä analyyttisesti aikaisempaa yleisemmin ja saadut tulokset varmennetaan tietokonesimulaatioissa ja mittauksissa. Tulosten pohjalta laaditaan MEMS-suodinsuunnittelulle säännöt, joissa otetaan ensimmäistä kertaa huomioon asetetut vaatimukset sekä intermodulaatiolle että häviöille. Viivelinjojen osalta työssä käsitellään mikromekaaniseen tankoon perustuvaa tilavuusaaltoviivelinjaa ja tuodaan esiin vaikeudet, jotka liittyvät riittävän hyvän kytkennän saavuttamiseen tällaisessa rakenteessa. Tehokkaampi kytkentä on HF-taajuuksilla mahdollinen jousimassaketjuun perustuvaan viivelinjaan, jollainen esitellään ja analysoidaan tässä väitöstyössä. Hyvän kytkennän lisäksi tämän viivelinjan ominaisuuksiin kuuluu kapeakaistaisuus ja erittäin hidas signaalin kulkunopeus. Mikromekaanisen jousimassaketjuviivelinjan toiminta varmennetaan mittauksin.

Avainsanat

MEMS, radio-frequency MEMS, microelectromechanical filters, microelectromechanical resonators, components, transducers, wireless communication, transmission lines, acoustic wave propagation, intermodulation

ISBN
951–38–6865–6 (nid.)
951–38–6866–4 (URL: http://www.vtt.fi/publications/index.jsp)

Avainnimeke ja ISSN	Projektinumero
VTT Publications 1235–0621 (nid.) 1455–0849 (URL: http://www.vtt.fi/publications/index.jsp)	

Julkaisuaika	Kieli	Sivuja	Hinta
Lokakuu 2006	Englanti, suom. tiiv.	57 s. + liitt. 56 s.	C

Projektin nimi	Toimeksiantaja(t)
MIRA	

Yhteystiedot	Myynti
VTT, PL 1000, 02044 VTT Puh. vaihde 020 722 111 Faksi 020 722 7012	VTT PL 1000, 02044 VTT Puh. 020 722 4404 Faksi 020 722 4374

VTT PUBLICATIONS 616 Microelectromechanical Resonator-Based Components for Wireless Communications Ari Alastalo

Starting in the early 1960's, when the integrated-circuit (IC) technology was developed, micromachining and microelectromechanical systems (MEMS) have grown into a broad research field with several commercial successes. Typical applications of MEMS are in physical, chemical and biochemical sensors, as well as in optical systems such as the digital micromirror device of Texas Instruments. From the 1990's, the advances in the processing technologies and the tremendous growth of the wireless-communication market have drawn much interest into radio-frequency MEMS devices (RF MEMS) such as filters, oscillators, switches and tunable capacitors. This thesis considers electrostatically-actuated RF-MEMS filters and delay lines. The intermodulation properties of capacitively-coupled MEMS filters are analytically solved in closed form and the theory is verified in numerical simulations as well as in measurements with MEMS resonators. The theory is utilized to formulate a design procedure for MEMS filters that takes systems specifications for tolerable intermodulation distortion and insertion-loss into account. For delay lines, capacitive actuation of bulk-acoustic waves in a solid rod is analyzed. In particular, challenges in impedance matching due to the weakness of the electrostatic coupling are quantified. Finally, a new kind of resonator-chain delay line is introduced. This delay line is characterized by record-low acoustic signal velocity, narrow-band response, and much lower characteristic impedance than found for the solid-rod waveguide enabling efficient signal coupling.

Tätä julkaisua myy

VTT
PL 1000
02044 VTT
Puh. 020 722 4404
Faksi 020 722 4374

Denna publikation säljs av

VTT
PB 1000
02044 VTT
Tel. 020 722 4404
Fax 020 722 4374

This publication is available from

VTT
P.O. Box 1000
FI-02044 VTT, Finland
Phone internat. +358 20 722 4404
Fax +358 20 722 4374

ISBN 951-38-6865-6 (soft back ed.)
ISSN 1235-0621 (soft back ed.)

ISBN 951-38-6866-4 (URL: http://www.vtt.fi/inf/pdf/)
ISSN 1455-0849 (URL: http://www.vtt.fi/inf/pdf/)